



저작자표시-비영리-변경금지 2.0 대한민국

이용자는 아래의 조건을 따르는 경우에 한하여 자유롭게

- 이 저작물을 복제, 배포, 전송, 전시, 공연 및 방송할 수 있습니다.

다음과 같은 조건을 따라야 합니다:



저작자표시. 귀하는 원저작자를 표시하여야 합니다.



비영리. 귀하는 이 저작물을 영리 목적으로 이용할 수 없습니다.



변경금지. 귀하는 이 저작물을 개작, 변형 또는 가공할 수 없습니다.

- 귀하는, 이 저작물의 재이용이나 배포의 경우, 이 저작물에 적용된 이용허락조건을 명확하게 나타내어야 합니다.
- 저작권자로부터 별도의 허가를 받으면 이러한 조건들은 적용되지 않습니다.

저작권법에 따른 이용자의 권리는 위의 내용에 의하여 영향을 받지 않습니다.

이것은 [이용허락규약\(Legal Code\)](#)을 이해하기 쉽게 요약한 것입니다.

[Disclaimer](#)

공학박사 학위논문

A Study on Estimation of Hydraulic Roughness
Height and Calibration Techniques for
Numerical Modeling through Bathymetry Data
Analysis

지형 데이터 분석을 통한 조도계수 산정 및
수치모델 보정 기법 연구

2024 년 8 월

서울대학교 대학원
건설환경공학부 건설환경공학전공

이 민 재

A Study on Estimation of Hydraulic Roughness Height
and Calibration Techniques for Numerical Modeling
through Bathymetry Data Analysis

지형 데이터 분석을 통한 조도계수 산정 및
수치모델 보정 기법 연구

지도교수 박용성

이 논문을 공학박사 학위논문으로 제출함

2024년 8월

서울대학교 대학원

건설환경공학부 건설환경공학전공

이민재

이민재의 공학박사 학위논문을 인준함

2024년 8월

위원장 _____ (인)

부위원장 _____ (인)

위원 _____ (인)

위원 _____ (인)

위원 _____ (인)

Abstract

A Study on Estimation of Hydraulic Roughness Height and Calibration Techniques for Numerical Modeling through Bathymetry Data Analysis

Lee, Minjae

Department of Civil and Environmental Engineering

The Graduate School

Seoul National University

The methods to estimate the roughness height and their application in numerical model are studied, focusing on the rough elements larger than several centimeters, measurable via image analysis and ultrasonic devices. The study consists of three parts, and to achieve the research objective of each part, experiments, field investigation, and numerical analysis were conducted.

In the first part, experiments were conducted to develop a roughness predictor for oyster reefs in coastal regions, which have not been previously studied for roughness height estimation methods. By examining the correlation between the geometric variables of oyster reefs and the roughness height through unidirectional and oscillatory flow experiments, the roughness predictor is proposed. The proposed roughness predictor is validated by comparing the estimated logarithmic velocity profile using the calculated roughness coefficients with experimentally measured velocities and is applicable under both unidirectional and

oscillatory flow conditions. The results of this study enable the estimation of the appropriate roughness height for the oyster reefs, which is crucial for understanding their hydraulic characteristics, and their roles in coastal protection.

In the second part, a study focuses on estimating the roughness height of bedforms, one of the primary rough elements in sandy rivers. Bedforms develop heterogeneously in river segments, causing spatial variations in roughness height and friction factor. To effectively examine the spatial heterogeneity, a method is proposed for estimating roughness height and friction factor from the transverse bathymetry data, allowing for the estimation of bed shear stress throughout the river. To assess the validity of bedform analysis and estimated form roughness height based on the transverse data, the characteristics of bedform and form roughness height analyzed using the transverse data are compared with those analyzed using the streamwise bathymetry survey data. Furthermore, the importance of considering the form roughness height in estimating bed shear stress is confirmed through a comparison with bed shear stress calculations that considered only grain roughness height.

In the third part, a study investigates the method of estimating and applying the friction coefficient, a key parameter in the calibration and validation of numerical models, through the analysis of bathymetry data. In the study, the surface analysis method used in the first and second studies is employed to estimate the roughness height and friction coefficient. During the process of estimating and applying the friction coefficient to the numerical model, three sensitivity factors are identified: (1) random extraction from the probability density function (2) filtering length (3) different form predictors. Therefore, the impacts of these three factors on the results of the numerical model are analyzed to evaluate the applicability of the friction coefficient estimated through bathymetry data analysis to the numerical model. The analysis results verify the robustness of the numerical results regardless of the three

sensitivity factors and confirm that the sensitivity of the numerical model results is not significant. The results confirm that incorporating the distribution of friction coefficients effectively enhances numerical model calibration and robustness.

Through these three parts, the study develops robust methods for estimating roughness height and applying these estimates in numerical models, improving their accuracy and predictive capabilities.

Keywords: Roughness height, Friction coefficient, Bathymetry analysis, Bed Shear Stress, Numerical modeling

Student Number: 2019-30187

3.4	Discussion	44
3.5	Concluding remarks	62
Chapter 4 ESTIMATION OF FRICTION FACTOR AND BED SHEAR STRESS		
	CONSIDERING BEDFORM EFFECT	64
4.1	Introduction	64
4.2	Field survey	66
4.3	Methodology	74
4.4	Results	84
4.5	Discussion	91
4.6	Concluding remarks	99
Chapter 5 CALIBRATION OF NUMERICAL MODEL USING FRICTION		
	FACTOR DISTRIBUTION	102
5.1	Introduction	102
5.2	Field experiment	103
5.3	Estimation of bedform friction factor	109
5.4	Numerical modeling	120
5.5	Results and discussions	126
5.6	Concluding remarks	140
Chapter 6 Conclusion		141
Bibliography		145
국문초록		165

List of Tables

Table 2.1	Wall regions and layers (Pope, 2000)	8
Table 2.2	Typical values of the friction coefficient (Julien, 2018)	14
Table 3.1	Experimental cases under the unidirectional flow over rough bottom conditions	32
Table 3.2	Experimental cases under the oscillatory flow over rough bottom conditions	32
Table 3.3	Roughness height ($k_{s,oc}$) calculated from Eq. 3.14 over the experimental rough surfaces for the unidirectional flow experiments (unit: mm)	45
Table 3.4	The roughness height ($k_{s,ow}$) of rough elements calculated from Eq. 3.16 over the experimental rough surfaces for the oscillatory flow experiments (unit: mm)	49
Table 3.5	Statistics of the height of rough element and roughness height depending on the five oyster reef surface classifications (Std: standard deviation; 50 th : 50 percentile; 90 th : 90 percentile)	61
Table 4.1	Average discharge, average water level, and representative percentile of discharge for four segments (ND-S1, ND-S2, ND-S3, and ND-S4)	68

Table 4.2	Characteristics of sediment particles for the four segments (ND-S1, ND-S2, ND-S3, and ND-S4) in the Nakdong River	69
Table 4.3	Hydraulic conditions at the field survey dates for measuring flow velocity (Q : discharge; \bar{U} : cross-sectional average velocity; \bar{h} : mean water depth; Fr : Froude number ($Fr = \bar{U}/\sqrt{g\bar{h}}$); g : gravitational acceleration ($9.81 m/s^2$))	73
Table 4.4	Average size of bedform and form roughness height	76
Table 4.5	Mean form roughness height (value in parentheses represents the standard deviation) and mean Chezy coefficient and Manning's n (ranges of Chezy coefficient and Manning's n values in parentheses)	87
Table 4.6	Parameters of the probability density function estimated for each segment	90
Table 5.1	Daily mean discharge at the study site. Q_{NH} is the outflow from the Hapcheon-Changnyeong weir; Q_H is the discharge of the Hwang River	106
Table 5.2	Form roughness predictors	110
Table 5.3	Mean, standard deviation (Std), and skewness (Skew) of the estimated Chezy coefficients depending on the smoothness and form predictors	116
Table 5.4	Mean, standard deviation (Std), and skewness (Skew) of the estimated Chezy coefficients depending on Manning's n values	116
Table 5.5	Probability density function error	118
Table 5.6	Simulation Cases for the Study Site. Q_{NH} is the Outflow from the Hapcheon-Changnyeong weir; Q_H is the Discharge of the Hwang River. SP Denotes Span Size	125
Table 5.7	Velocity error for different roughness sets	133

Table 6.1	Research summary	144
-----------	----------------------------	-----

List of Figures

Figure 1.1	Research objectives and flowchart for the studies in Chapter 3-5 . . .	5
Figure 2.1	Wall regions and layers defined in terms of y^+ and y/δ (Pope, 2000)	8
Figure 2.2	Turbulent flows over rough surfaces (Kadivar et al., 2021)	9
Figure 2.3	Definition of bedform geometric parameters (Gutierrez et al., 2013)	13
Figure 2.4	Schematic diagram of the flow over the bedform (FSZ: flow separation zone) (Best, 2005)	13
Figure 3.1	(a) Contour image of original surface data (b) Contour image of roughness level (z_{RL}) (c) Example of roughness level and definition of geometric variables of the roughness level (Black solid line: original surface profile; Red solid line: reference level; blue solid line: roughness level; red dashed line: zero-level; Δ_o : height of the rough element; Λ_o : length of the rough element)	20
Figure 3.2	(a) ECDF of rough element height over the oyster reef surfaces (b) ECDF of rough element length over the oyster reef surfaces (ECDF: empirical cumulative distribution function)	22
Figure 3.3	Sketch of the open channel flume and the experimental setup of the unidirectional flow experiment	24

Figure 3.4	Sketch of the oscillatory water tunnel and the experiment setup of the oscillatory flow experiment	24
Figure 3.5	Contour images of the experimental rough bottom models and the PIV measurement sections over the rough bottom models (a) RBC1 (b) RBC2 (c) RBW1 (d) RBW2	29
Figure 3.6	Contour images of the experimental rough bottom models and the PIV measurement sections for investigating the scale effect of roughness predictor (a) RBC3 (b) RBW3	30
Figure 3.7	Flow regime for the oscillatory flow experiments in $Re - A/k_s$ space (Orange marker: the experimental conditions in this study)	33
Figure 3.8	The PIV-measured velocity profiles and corresponding fitted logarithmic velocity profiles over selected oyster models (R1, R8, R10, R13, and R16) in RBC1 and RBC2 (a) Experiments with a water depth of 0.1 m (b) Experiments with a water depth of 0.15 m (Color markers: the PIV-measured velocity; Color solid lines: the fitted logarithmic velocity profile)	37
Figure 3.9	The relationship between the dimensional variables of the oyster model and the roughness height in the unidirectional flow (a) Roughness height as a function of the height of the rough element (Δ_o) (b) Roughness height as a function of height and length of the rough element (Δ_o^2/Λ_o) (Red solid line: regression line between the roughness height and the geometric variables; Blue dashed line: lower and upper bound of the 95% confidence interval)	39

Figure 3.10	Example of the logarithmic velocity profile with the corresponding measured velocity at selected phases over oyster models (a) RW7 (Experimental case: U22R1) (b) RW15 (Experimental case: U22R2) (Blue dot: the PIV-measured velocity; Black solid line: the fitted logarithmic velocity profile)	41
Figure 3.11	The relationship between the geometric variables of the oyster model and roughness height in the oscillatory flow (a) Roughness height against Δ_o (b) Roughness height against Δ_o^2/Λ_o (Red solid line: the regression line between the roughness height and the geometric variables; Blue dashed line: lower and upper bound of 95% confidence interval)	43
Figure 3.12	Comparison between the PIV-measured velocity profile and the logarithmic velocity profile over the oyster models (R7, R9, R12, and R14) in RBC1 and RBC2 to validate the roughness predictor (Eq. 3.14) (a) Unidirectional flow experiments with a water depth of 0.1 m (b) Unidirectional flow experiments with a water depth of 0.15 m (Color marker: the PIV-measured velocity; Color solid line: the fitted logarithmic velocity profile)	46

Figure 3.13	Comparison between the PIV-measured velocity profile and the logarithmic velocity profile over the oyster models (RV2, RV5, RV6, and RV7) in RBC3 to assess the scale effect of the roughness predictor (Eq. 3.14) (a) Unidirectional flow experiments with a water depth of 0.1 m (b) Unidirectional flow experiments with a water depth of 0.15 m (Color marker: the PIV-measured velocity; Color solid line: the fitted logarithmic velocity profile)	47
Figure 3.14	Comparison between the PIV-measured velocity profile and the fitted logarithmic velocity profile at selected phase over the oyster models under the oscillatory flow condition (RW2, RW8, RV15, RVW7, and RVW9) (Marker: the PIV-measured velocity; Solid line: the fitted logarithmic velocity profile)	49
Figure 3.15	ECDF for the height and length of rough elements on the oyster reef surfaces	51
Figure 3.16	Comparison between the PIV-measured velocity and the fitted logarithmic velocity over the oyster models (R9, R16, RV2, and RV7) to validate the unified roughness predictor (Eq. 3.18) under unidirectional flow condition (a) Experiments with the water depth of 0.1 m (b) Experiments with the water depth of 0.15 m (Color marker: the PIV-measured velocity; Color solid line: the fitted logarithmic velocity profile)	53

Figure 3.17	Comparison between the PIV-measured velocity and the fitted logarithmic velocity over the oyster models (RW2, RW8, RW15, RVW7, and RVW9) to validate the unified roughness predictor (Eq. 3.18) under the oscillatory flow condition (Marker: measured velocity; Solid line: fitted logarithmic velocity profile)	54
Figure 3.18	Wave friction factor (f_w) as a function of relative roughness height (A/k_s) with the previous study results and empirical relations (The wave friction factor of previous results are referenced including those from Van Der A et al. (2011), Yuan and Madsen (2014), and O'Donoghue et al. (2021))	56
Figure 3.19	Boundary layer thickness as a function of relative roughness height (A/k_s) with the previous study results and empirical relations (The boundary layer thickness' of previous results are referenced including those from Van Der A et al. (2011), Yuan and Madsen (2014), and O'Donoghue et al. (2021))	58
Figure 3.20	Distribution of the roughness height over oyster reef surfaces depending on the five structural classifications	61
Figure 4.1	The map of study site (a) Overview of field survey area (b)-(e) Thalweg bed profile survey lines for the four segments (ND-S1, ND-S2, ND-S3, and ND-S4) and velocity measured area (ND-GJ, ND-DS, ND-HC, and ND-CH) with indicated orange box	67
Figure 4.2	The bed elevation along the center of channel, measured through four field surveys (a) ND-S1 (b) ND-S2 (c) ND-S3 (d) ND-S4	71

Figure 4.3 Decomposition of bedform level and definition of bedform information, height and length (a) Sample of measured bed profile (black solid line) and its smoothed bed profile (red solid line) (b) Bedform level and definition of bedform height and length 75

Figure 4.4 (a) Correlation plot of bedform height and length, where the red solid line is for $\Lambda_f/d_{50} = 4.1 \times 10^3 (\Delta_f/d_{50})^{1/3}$; the blue dashed line is for $\Lambda_f/d_{50} = 8.2 \times 10^3 (\Delta_f/d_{50})^{1/3}$; the purple dashed line is for $\Lambda_f/d_{50} = 1.6 \times 10^3 (\Delta_f/d_{50})^{1/3}$; (b) Distribution of bedform height (c) Distribution of bedform length 79

Figure 4.5 Identification of roughness elements in bed profile in the transverse direction (a) Sample of measured bed profile and its smoothed bed profile (b) Identification of rough elements from the decomposed bed level and definition of bedform height 81

Figure 4.6 Comparison of bedform height and form roughness height estimated from streamwise and transverse bed profile data for velocity measured region (a) ND-DS (B) ND-HC (c) ND-CH (Blue circle: estimated values from streamwise bed profile data; Green diamond: estimated values from transverse bed profile data with Eq. 4.2); blue dashed line: estimated values from transverse bed profile data with $\Lambda_f/d_{50} = 8.2 \times 10^3 (\Delta_f/d_{50})^{1/3}$; purple dashed line: estimated values from transverse bed profile data with $\Lambda_f/d_{50} = 1.6 \times 10^3 (\Delta_f/d_{50})^{1/3}$) 86

Figure 4.7	(a) Distribution of form roughness height (b) Distribution of Chezy coefficient (Color dot: empirical cumulative distribution function for observed value; Red solid line : fitted probability density function)	89
Figure 4.8	Vertical velocity profile at selected points and logarithmic velocity profile at selected points (a) ND-CH1 (b) ND-CH2 (Gray dot: the measured velocity; Blue solid line: the logarithmic velocity profile)	92
Figure 4.9	Correlation plot of bed shear stress computed by the log-law and depth-average velocity	93
Figure 4.10	Bed shear stress in ND-GJ, ND-DS, ND-HC, and ND-CH (a) Comparison of grain bed shear stress and form bed shear stress computed using log-law (b) Comparison of grain bed shear stress and total bed shear stress computed using log-law (Red solid line represents $\tau_{b,log} = 1.717\tau_{b,g,log}$) (d) Comparison of grain bed shear stress and form bed shear stress computed using depth-average velocity (d) Comparison of grain bed shear stress and total bed shear stress computed using depth-average velocity (Red solid line represents $\tau_{b,U} = 3.794\tau_{b,g,U}$)	95
Figure 4.11	Comparison of the grain bed shear stress, form bed shear stress, and total bed shear stress calculated using depth-average velocity. (a) Distribution of the grain bed shear stress (left), the form bed shear stress (middle), and the total bed shear stress (right) for ND-CH1. (a) Distribution of the grain bed shear stress (left), the form bed shear stress (middle), and the total bed shear stress (right) for ND-CH2.	98

Figure 5.1	Study site of the study in Chapter 5. Downstream of the Hapcheon-Changnyeong weir in the Nakdong River. The region with blue color is the computational domain and white solid lines are survey lines.	104
Figure 5.2	Changes in the bed elevation in each cross-section (a) NHS2 (b) NHS3 (c) NHS4 (d) NHS5. A Solid line along the brown area is the bed elevation measured on the first field survey, and other colors show the bed elevation on subsequent field surveys, respectively.	107
Figure 5.3	Variation of the daily average discharge of outflow from the Hapcheon-Changnyeong weir from 2013 to 2020 (Black circle: the daily averaged discharge; Blue line: the discharge corresponding to 95th percentile of outflow from the Hapcheon-Changnyeong weir; Red line: the discharge corresponding to 99th percentile of outflow from the Hapcheon-Changnyeong weir)	108
Figure 5.4	Estimation of the bedform height using the zero-crossing method (a) Example of the field-measured bed profile (black solid line) and smoothed bed profile (blue dot line) in NHS5 and the bedform height defined from the residual bed level (b) Comparison between the field-measured bed profile and smoothed bed profiles using the 5 different span size (SS=0.05, 0.1, 0.15, 0.2, and 0.25) (Black solid line: the measured bed profile; Blue solid line: SS=0.05; Blue dot line: SS=0.1; Purple solid line: SS=0.15; Purple dot line: SS=0.2; Green solid line: SS=0.25)	112

Figure 5.5 Distribution and box plot of the Chezy coefficients according to the span size and form roughness predictors. The Chezy coefficients are calculated using three different form predictors (a) VR1993 (b) Soulsby 1997 and (c) BAR2010. 115

Figure 5.6 Comparison between the computed Chezy coefficients and the fitted probability density function according to form predictors (a) VR1993 (b) Soulsby1997 (c) BAR2010 119

Figure 5.7 Example of distribution of Chezy coefficient (a) Q2V15 (b) Q2M20 (c) Q2M25 (d) Q2M30 (e) Q2M35 124

Figure 5.8 Comparison between the field-measured velocity and simulated velocities on the section NHS3 (left in subfigure) and NHS4 (right in subfigure) (Black dot: the field-measured velocity; Blue solid line: the simulated depth-averaged velocity) (a) Streamwise velocity (U_s) and transverse velocity (U_n) in case of Q1V10 (b) Streamwise and transverse velocity in case of Q2V10 (c) Streamwise and transverse velocity in case of Q3V10. Positive value of the transverse velocity represents the eastward transverse direction (toward to left bank) and negative value of the transverse velocity represents the westward transverse direction (toward to right bank). 128

Figure 5.9 Comparison between the field-measured velocity and simulated velocities on section NHS3 (a) Q1V10 (b) Q2V10 (c) Q3V10 (Left in subfigure: the field-measured streamwise velocity; Right in subfigure: the simulated streamwise velocity; u_s : streamwise velocity) . . 129

Figure 5.10	RMSE for the measured water depth and simulated water depth at NHS2-NHS5 (Orange bar graph: Q1V10; Blue bar graph: Q2V10; Purple bar graph: Q3V10)	130
Figure 5.11	Comparison of the depth-averaged velocity error between the models with different roughness sets (a) Q1V10 (b) Q2V10 (c) Q3V10 (Red solid line: roughness case 1; Purple solid line: roughness case 2; Yellow solid line: roughness case 3)	132
Figure 5.12	Depth-averaged velocity error depending on the smoothness and form Predictors, VR1993 and BAR2010 for: (a) Q1V05-Q1V20 (b) Q1B05-Q1B20 (c) Q2V05-Q2V20 (d) Q2B05-Q2B20 (e) Q3V05-Q3V20 (f) Q3B05-Q3B20 (Red solid line: span size =0.05; Purple solid line: span size = 0.10; Yellow solid line: span size = 0.15; Green solid line: span size = 0.20)	136
Figure 5.13	Cumulative distribution of depth averaged-velocity error for each validation cases; (a) Q1V15 and Q1M20-Q1M35 (b) Q2V15 and Q2M20-Q2M35 (c) Q3V15 and Q3M20-Q3M35 (Red: V15; Purple: M20; Yellow: M25; Green: M30; Blue: M35)	138
Figure 5.14	Comparison of the depth-average velocity results at NHS2-NHS5 for the numerical results with different Manning's n under Q2 flow condition: (a) NHS2, (b) NHS3, (c) NHS4, (d) NHS5 (Purple: Q2M20; Yellow: Q2M25; Green: Q2M30; Blue: Q2M35)	139

Nomenclature

A	Orbital amplitude
C	Chezy coefficient
C_d	Drag coefficient
C_f	Dimensionless Chezy coefficient
D_H	Horizontal eddy diffusivity
Δ_f	Height of bedform
Δ_o	Height of rough element on oyster reefs
Fr	Froude number
f	Darcy-Weisbach friction factor
f_f	Form related friction coefficient
f_g	Grain related friction coefficient
f_w	Wave friction factor
h	Water depth
k_s	Roughness height
$k_{s,f}$	Form roughness height
$k_{s,g}$	Grain roughness height
$k_{s,o}$	Roughness height of oyster reef
k_s^+	Dimensionless roughness height
κ	von Kármán constant
Λ_f	Length of bedform
Λ_o	Length of rough element on oyster reefs
μ	Dynamic viscosity
n	Manning coefficient

ν	Kinematic viscosity
ν_H	Horizontal eddy viscosity
ν_{SGS}	sub-grid scale horizontal eddy viscosity
ν_V	Vertical eddy viscosity
ω	Radian frequency
p	Pressure
Φ	Universal non-dimensional function
Q	Flow discharge
R	Hydraulic radius
Re	Reynolds number
Re_τ	Friction Reynolds number
ρ	Water density
S	Friction slope
T_w	Wave period
τ_b	Bed shear stress
$\tau_{b,w}$	Bed shear stress in wave motion
u, v, w	Velocity component
$\bar{u}, \bar{v}, \bar{w}$	Time-averaged velocity
$\hat{u}, \hat{v}, \hat{w}$	Phase-averaged velocity
u', v', w'	Turbulence component
u_∞	Freestream velocity in oscillatory flow
$\langle \bar{u} \rangle$	Time and spatially averaged velocity
$\langle \hat{u} \rangle$	Phase and spatially averaged velocity
u_*	Shear velocity

u^+	Dimensionless velocity scale
z_0	Hydraulic roughness height
z^+	Dimensionless wall distance

Chapter 1. INTRODUCTION

1.1 Introduction

Roughness is a fundamental concept in earth sciences, influencing various processes. In fluid mechanics, roughness significantly affects flow structure, impacting bed shear stress, turbulence, and transport of sediment and substance. Therefore, it is essential to characterize surface roughness, often referred to as roughness.

However, the term, roughness, is used in different contexts, leading to terminological confusion. Roughness can be defined in physically, as a flow property, or as a calibration parameter (Smith, 2014). Physically, roughness refers to surface variability or irregularity. As a flow property, it is the height where flow velocity is zero. As a calibration parameter, roughness is used as a parameter to represent subgrid-scale processes without physical meaning. As an attempt to integrate the three aforementioned perspectives of roughness, roughness height is defined based on the physical characteristics of rough elements.

Roughness height can be formulated using the geometric variables of rough elements. For example, the grain roughness height can be determined by grain diameter (Yen, 2002), and form roughness height can be formulated using the height and length of bedforms (Van Rijn, 1993; Soulsby, 1997; Bartholdy et al., 2010; Lefebvre and Winter, 2016). Thus, collecting data on bed characteristics is essential for estimating the roughness height. Various methods, such as sieve analysis and image analysis for sediment distribution (Ren et al., 2020; Yoo et al., 2024), topographic data analysis for bedform features (Smart et al., 2002; Van Der Mark et al., 2008; Cazenave et al., 2013; Gutierrez et al., 2013; De Lange et al., 2021), and 3D surface data analysis for irregular rough surface (Choe et al., 2012; Hitzegrad et al.,

2022) are used for analyzing rough bottom characteristics.

Roughness height is a crucial parameter for estimating bed shear stress and predicting velocity. Using the log-law, roughness height fundamentally controls the vertical velocity structure of rough turbulent flow (Schlichting and Gersten, 2016; Kadivar et al., 2021). Additionally, friction coefficients, such as the Manning's n and Chezy coefficient (C) are commonly used in the flow resistance formulae (Yen, 2002; Chanson, 2004). Friction coefficient describes the resistance due to the interaction between the fluid and the surface, and this value differs depending on the rough surface condition. Accurately determining roughness height and friction coefficient is essential for properly representing hydrodynamics and sediment transport (Powell, 2014).

In computational fluid dynamics, roughness height is a crucial parameter for model calibration and interpretation of flow velocity and sediment transport processes including erosion, deposition, and bedform development (Dao and Tkalich, 2007; Kasvi et al., 2015; Rousseau et al., 2016; Xia et al., 2022). Additionally, roughness height is essential for representing boundary layer flow and calculate the bed shear stress, which serves as a bottom boundary condition for solving momentum equations. Representing roughness elements at the actual scale in numerical simulations is nearly impossible due to computational constraints. Instead, roughness height and/or friction coefficient are employed to characterize the bottom conditions. Thus, it is important to determine appropriate roughness height and/or friction coefficient for numerical simulations, taking into account bed conditions.

Despite the significance of roughness height, the complexity and variability in roughness characteristics raise the challenge in accurately determining of roughness height and friction factor. Advances in field measurement equipment and technology provide valuable data to investigate the relationship between surface characteristics and roughness heights.

In addition, the field survey findings allow enhancing the fidelity and predictive capabilities of numerical simulations. This study focuses on analyzing the field survey data to estimate roughness height and friction factor, thereby improving the applicability and robustness of numerical models by considering rough bottom conditions.

1.2 Objectives and scope of the study

The objective of this dissertation is to estimate roughness height and validate its applicability to numerical modeling using field survey data. To achieve this objective, the studies are organized as follows. In Chapter 1, the general research background and motivation are introduced. In Chapter 2, the theoretical background of roughness height is addressed. Chapter 3 presents an experimental study on estimating roughness height using geometric variables of rough elements over uneven surfaces. Experiments were conducted with unidirectional and oscillatory flow in an open channel flume and an oscillatory water tunnel with rough bottom models. Based on the measured velocities obtained from those experiments, roughness height for the rough bottom models is estimated, and a roughness predictor is derived and validated. This chapter demonstrates that the roughness height can be calculated using the geometry variable of the rough elements. Chapter 4 suggests a method for estimating friction factor and bed shear stress in sandy rivers. In sandy river bed environments, bedforms affect the roughness height and bed shear stress, and their spatial variation impacts the bed shear stress. The chapter proposes a method for estimating the friction factor related to bedforms, highlighting the significance of bedforms in estimating the spatial distribution of bed shear stress in rivers. Chapter 5 covers the study on estimating and applying the friction factors based on field-measured data for numerical calibration. In sandy river beds with irregular features, the spatial distribution of the friction coefficient varies. This chapter

analyzes river bed characteristics and estimates the friction coefficient distribution from field survey data. These estimations are used to determine friction factors for numerical model calibration, and their applicability to numerical models is investigated. Chapter 6 provides the overall conclusions of the studies in the dissertation.

Chapter 3 demonstrates through experiments that the roughness height can be estimated solely based on the geometric information of rough elements. Chapter 4 and Chapter 5 focus on field applications, assuming roughness height can be estimated using field-measured bed information. Chapter 4 estimates both the roughness height and friction coefficient based on field survey data collected at a field scale and applies these estimates to river analysis. The roughness height and friction coefficient are crucial parameters for analyzing both experimental and field measurement data and for constructing numerical models. Thus, Chapter 5 integrates the experimental findings of Chapter 3 and the field applications of Chapter 4 into numerical modeling practices. Fig. 1.1 summarizes research objectives and research flow of this dissertation.

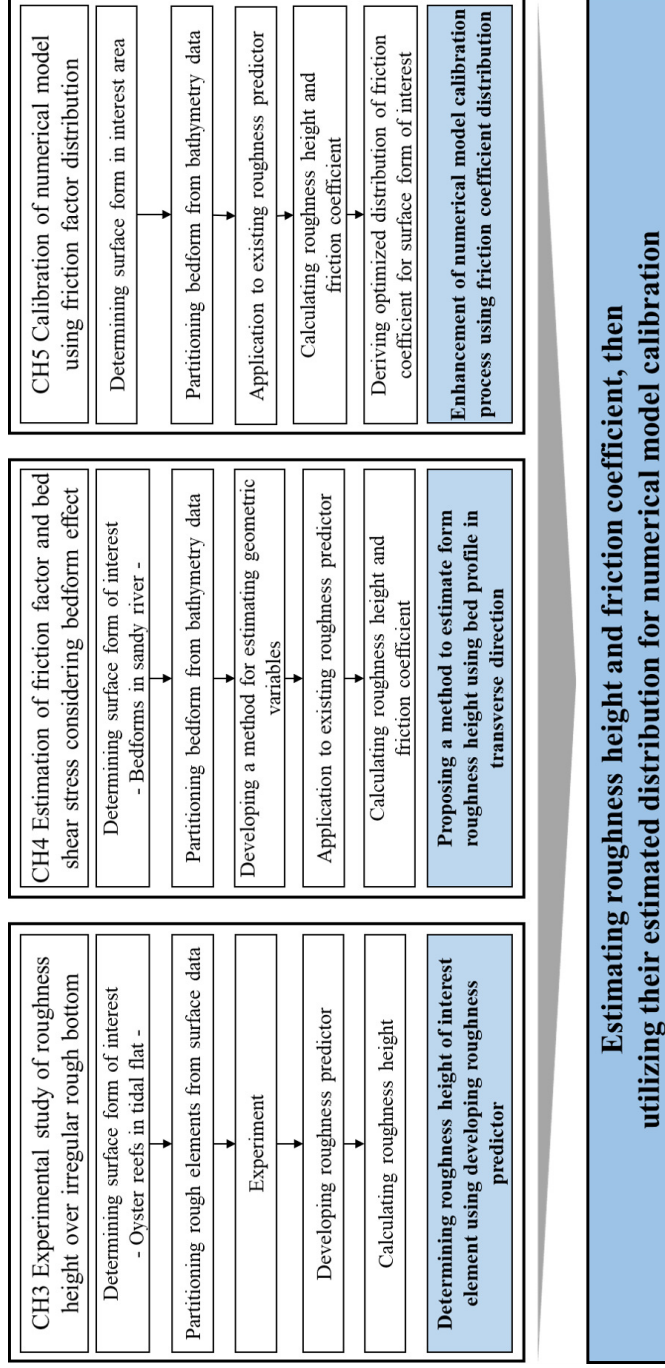


Figure 1.1: Research objectives and flowchart for the studies in Chapter 3-5

Chapter 2. THEORETICAL BACKGROUND

2.1 Mean velocity profile

From the dimensional analysis, the mean velocity profile and velocity gradient can be written as follows:

$$\langle u \rangle = u_* F\left(\frac{y}{\delta}, Re_\tau\right), \quad (2.1)$$

$$\frac{d\langle u \rangle}{dy} = \frac{u_*}{y} \Phi\left(\frac{y}{\delta_\nu}, \frac{y}{\delta}\right), \quad (2.2)$$

where u_* is shear velocity ($u_* = \sqrt{\tau_b/\rho}$); δ is characteristic length scale; Re_τ is friction Reynolds number ($Re_\tau = u_*\delta/\nu = \delta/\delta_\nu$); δ_ν is viscous length scale ($\delta_\nu = \nu\sqrt{\frac{\rho}{\tau_b}} = \nu/u_*$).

At high Reynolds number and close to the wall ($y/\delta \ll 1$; inner layer), the mean velocity profile is determined by the viscous scale and it can be written as follows:

$$u^+ = f_w(y^+), \quad (2.3)$$

$$f_w(y^+) = \int_0^{y^+} \frac{1}{y'} \Phi(y') dy', \quad (2.4)$$

where u^+ is defined as $\langle u \rangle / u_*$; y^+ is dimensionless wall unit ($y^+ = y/\delta_\nu = u_*y/\nu$); Φ is universal non-dimensional function.

Outer part of the inner layer corresponds to large y^+ . It can be supposed that viscosity has little effect when y^+ is large, so that Φ adopts a constant value denoted by von Kármán constant (κ).

$$\Phi(y^+) = \frac{1}{\kappa}, \quad \text{for } \frac{y}{\delta} \ll 1 \text{ and } y^+ \gg 1. \quad (2.5)$$

In this region, the mean velocity gradient and the velocity profile can be written as follows:

$$\frac{du^+}{dy^+} = \frac{1}{\kappa y^+}, \quad (2.6)$$

$$u^+ = \frac{1}{\kappa} \ln y^+ + C_1, \quad (2.7)$$

where C_1 is constant and it has different value depending on the bottom conditions. κ is set to 0.41 within a 5% variation. Eq. 2.7 is valid for $y^+ > 30$ (Schlichting and Gersten, 2016). The various regions and layers for near-wall flows are summarized in Table 2.1 and Fig. 2.1.

In reality, the bottom is normally rough rather than smooth. Thus, the roughness height is introduced and the log-law (Eq. 2.7) can be rewritten as

$$u^+(y^+) = \frac{1}{\kappa} \ln \frac{y}{k_s} + C^+(k_s^+), \quad (2.8)$$

$$k_s^+ = \frac{k_s}{\delta_v} = \frac{k_s u_*}{\nu}, \quad (2.9)$$

where k_s^+ is roughness characteristic number; k_s is roughness height. If k_s becomes large enough to take up all of the wall layer, the viscosity is no further importance, called fully rough regime. Three different rough regimes can be defined based on the different values of k_s^+ , hydraulically smooth regime ($0 \leq k_s^+ \leq 5$), transitionally rough regime ($5 < k_s^+ < 70$), and fully rough regime ($70 \leq k_s^+$) (Fig. 2.2). The rough elements are entirely embedded in the viscous sublayer, and skin friction and drag coefficient are not modified compared to the smooth bottom condition under hydraulically smooth regime. Transitionally rough regime is characterized by a complex influence of rough surface, where both the Reynolds number and relative roughness impact the skin friction and drag coefficient. In case of fully rough regime, the rough elements protrude into the fully turbulent region, causing a downward shift

in the logarithmic velocity profile. The viscous sublayer is entirely disrupted by turbulence caused by rough elements. The friction drag significantly increases due to pressure forces and becomes independent of the viscous effect.

Table 2.1: Wall regions and layers (Pope, 2000)

Region	Location	Defining property
Inner layer	$y/\delta < 0.1$	U determined by u_* and y^+
Viscous wall region	$y^+ < 50$	The viscous contribution to the shear stress is significant
Viscous sublayer	$y^+ < 5$	The Reynolds stress is negligible compared with the viscous stress
Outer layer	$y^+ > 50$	Direct effects of viscosity on U are negligible
Overlap layer	$y^+ > 50, y/\delta < 0.1$	Region of overlap between inner and outer layers (at large Reynolds numbers)
Log-law region	$y^+ > 30, y/\delta < 0.3$	the log-law holds
Buffer layer	$5 < y^+ < 30$	The region between the viscous sublayer and the log-law region

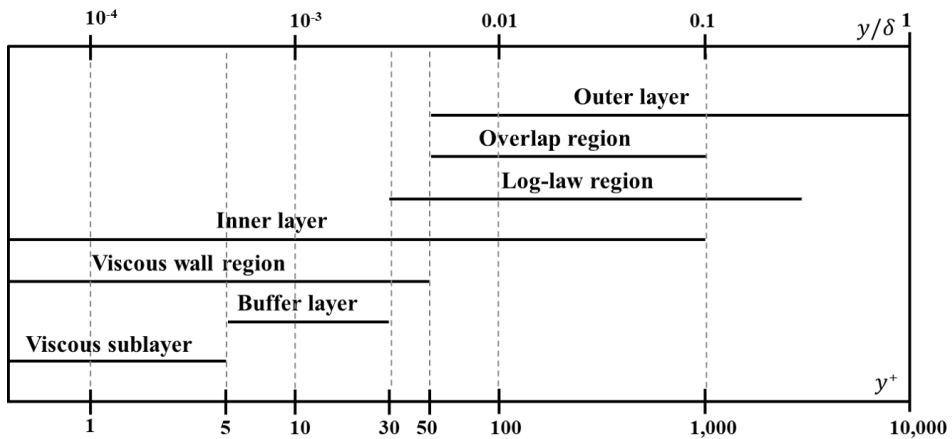


Figure 2.1: Wall regions and layers defined in terms of y^+ and y/δ (Pope, 2000)

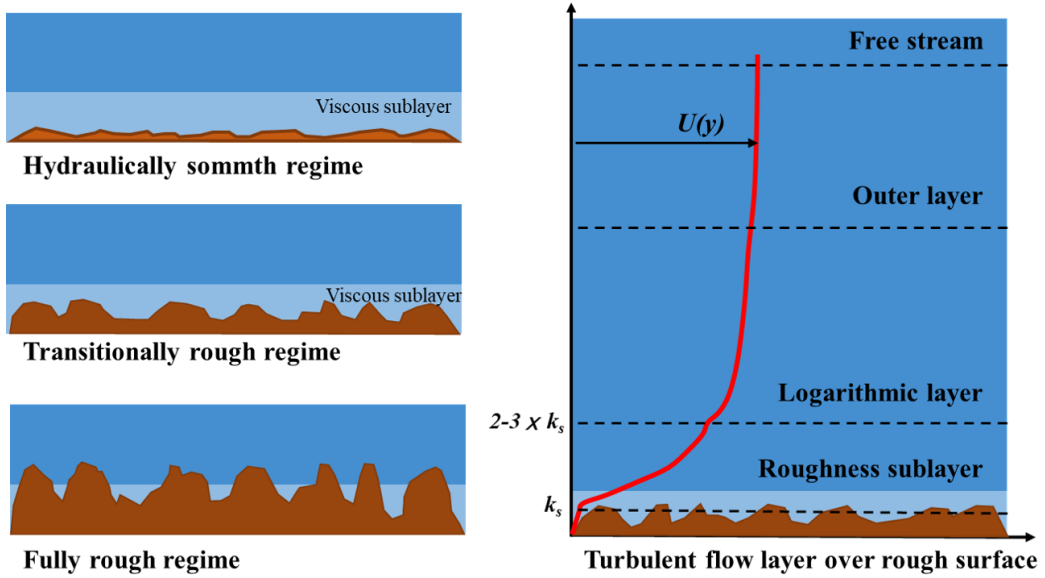


Figure 2.2: Turbulent flows over rough surfaces (Kadivar et al., 2021)

2.2 Flow resistance in open channel flow

The frequently used formulas for open channel flow velocity with friction coefficient are as follows:

$$U = \sqrt{\frac{8g}{f}} \sqrt{RS} \quad (2.10)$$

$$U = C \sqrt{RS} \quad (2.11)$$

$$U = \frac{1}{n} R^{2/3} S^{1/2} \quad (2.12)$$

where n is Manning coefficient; f is Darcy-Weisbach friction factor; C is Chezy coefficient; R is hydraulic radius; S is friction slope. From Eqs. 2.12-2.11, relationship between friction coefficients can be found.

$$\sqrt{\frac{f}{8}} = \frac{\sqrt{gn}}{R^{1/6}} = \frac{\sqrt{g}}{C} = \frac{\sqrt{gRS}}{V} \quad (2.13)$$

Bed shear stress can be also expressed using friction coefficient.

$$\tau_b = \frac{f}{8} \rho U^2 = \frac{\rho g U^2}{C^2} = \frac{\rho g n^2 U^2}{R^{1/3}} \quad (2.14)$$

Formula for Chezy coefficient can be obtained by integration of the logarithmic law.

$$u = \frac{1}{h} \int_{z_0}^h \frac{u_*}{\kappa} \ln(z/z_0) \quad (2.15)$$

$$C = \frac{2\sqrt{g}}{\kappa} \log\left(\frac{12h}{k_s}\right), \quad (2.16)$$

where z_0 is hydraulic roughness height ($z_0 = k_s/30$). Chezy coefficient (Eq. 2.16) can be calculated using k_s , however, k_s is estimated considering rough surface conditions. Commonly used roughness heights are grain roughness height ($k_{s,g}$) and form roughness height ($k_{s,f}$). Grain roughness height, $k_{s,g}$ can be estimated by grain diameter as follows (Yen, 2002):

$$k_{s,g} = \alpha d_*, \quad (2.17)$$

where α is constant variable; d_* is representative grain diameter. Form roughness height, $k_{s,f}$ is formulated by geometric variables of bedform and suggested form roughness predictors are as follows:

$$k_{s,f} = 1.1\Delta_f \left(1 - \exp \left(- 25\Delta_f / \Lambda_f \right) \right) \text{ (Van Rijn, 1993),} \quad (2.18)$$

$$k_{s,f} = \frac{30\Delta_f^2}{\Lambda_f} \text{ (Soulsby, 1997),} \quad (2.19)$$

$$k_{s,f} = 0.57\Delta_f \text{ (Bartholdy et al., 2010),} \quad (2.20)$$

$$k_{s,f} = 1975\gamma \frac{\Delta_f}{h} \left(\frac{\Delta_f}{\Lambda_f} \right)^2 \text{ (Lefebvre and Winter, 2016),} \quad (2.21)$$

where Δ_f is height of bedform; Λ_f is length of bedform; γ is reduction factor to consider lee side angle of bedform, $\gamma = \frac{1}{1+\exp(-0.56\theta+13.3)}$ (Lefebvre and Winter, 2016).

The geometric variables of bedforms can be defined in several ways (Fig. 2.3) (Gutierrez et al., 2013). When bedforms are present on the bottom, form-influenced flow field is generated, which is affected by the bedforms (Lefebvre et al., 2014). Flow separation occurs due to a strong pressure gradient over the lee side with reattachment occurring in the trough. An internal boundary layer develops after reattachment, leading to the formation

of logarithmic velocity profile. A shear layer forms, bounding the flow separation zone, and turbulence is generated along this shear layer. Maximum velocity occurs over the crest of bedform. This flow structure affects the bed shear stress. Fig. 2.4 illustrates the form-influenced flow field and principal regions of flow over the bedform (Best, 2005).

Other friction coefficient widely used is Manning coefficient, n . Manning's n value can be considered a constant value regardless of the water depth, on the other hand, it should change depending on the bed condition. Recommended Manning's n value is well organized depending on the bed condition empirically. Table 2.2 provides typical values of friction coefficients depending on bottom conditions (Julien, 2018).

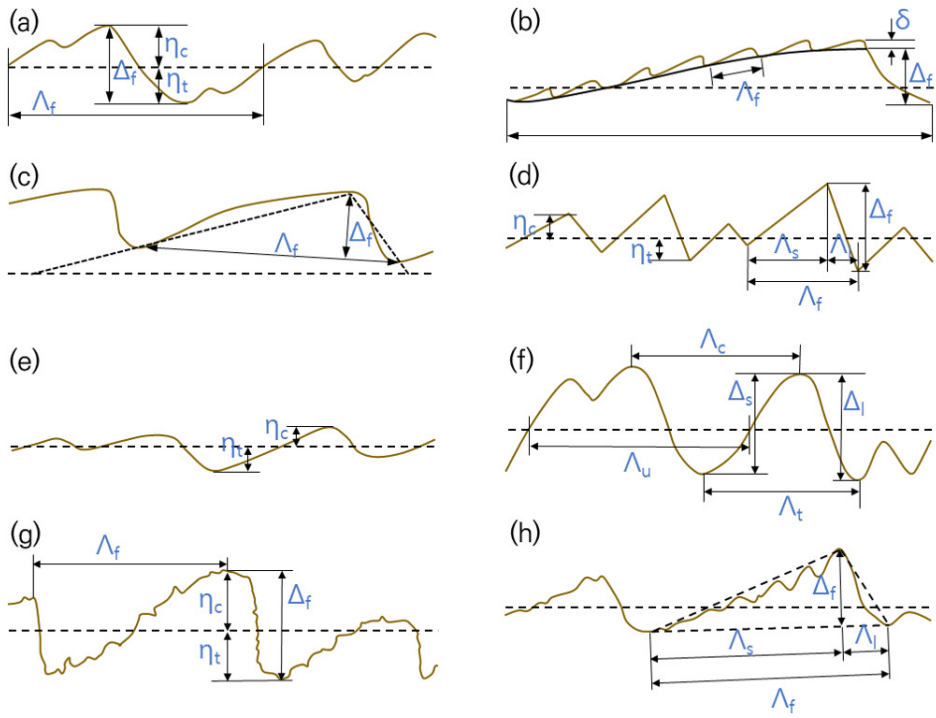


Figure 2.3: Definition of bedform geometric parameters (Gutierrez et al., 2013)

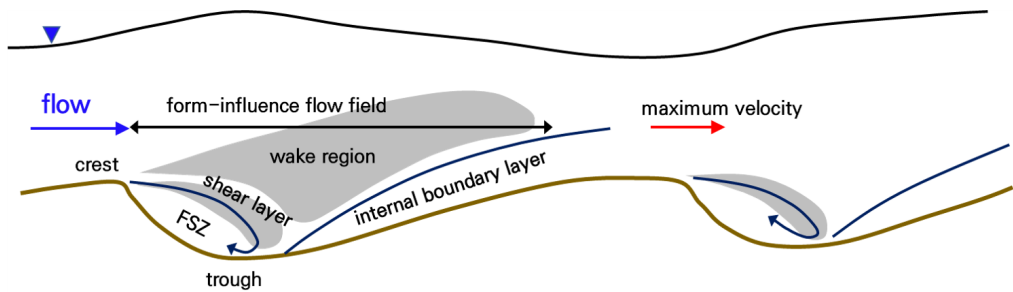


Figure 2.4: Schematic diagram of the flow over the bedform (FSZ: flow separation zone) (Best, 2005)

Table 2.2: Typical values of the friction coefficient (Julien, 2018)

Boundary type	Manning's n ($s/m^{1/3}$)	Chezy Coefficient ($C, m^{1/2}/s$)	Darcy-Weisbach, f
Smooth	0.01	118	0.0056
Plane sand bed	0.010-0.013	100-130	0.0046-0.0078
Sand antidunes	0.013-0.018	72-100	0.0078-0.015
Ripples	0.018-0.030	43-72	0.015-0.042
Sand dunes	0.020-0.040	32-65	0.018-0.076
Gravel bed	0.015-0.030	43-86	0.011-0.042
Cobble bed	0.020-0.035	37-65	0.018-0.057
Boulder bed	0.025-0.04	32-52	0.029-0.076
Vegetation	0.03-0.07	18-43	0.042-0.24

2.3 Wave boundary layer flow

The boundary layer flow by uniform and oscillatory flow can be obtained from the momentum equation.

$$\rho \left(\frac{\partial u}{\partial t} + u \frac{\partial u}{\partial x} + w \frac{\partial u}{\partial z} \right) = - \frac{\partial p}{\partial x} + \frac{\partial \tau_b}{\partial z} \quad (2.22)$$

$$\rho \frac{\partial}{\partial t} (U_\infty - u) = - \frac{\partial \tau_b}{\partial z} \quad (2.23)$$

where u_∞ is free stream velocity outside the boundary layer. In case of laminar flow, the boundary layer flow and bed shear stress are expressed as follows:

$$u = U_\infty \sin \omega t - U_\infty \exp \left(- \frac{z}{\delta} \right) \sin \left(\omega t - \frac{z}{\delta} \right) \quad (2.24)$$

$$\frac{\tau_b}{\rho} = \nu \frac{\partial u}{\partial z} = \frac{\nu U_\infty}{\delta} (\sin \omega t + \cos \omega t) \quad (2.25)$$

where boundary layer thickness, δ is $\sqrt{2\nu/\omega}$; ω is radian frequency of oscillatory flow; ν is kinematic viscosity. From the equation, it can be found that there is a phase shift of 45° between the flow outside the boundary layer and bed shear stress.

Eq. 2.23 can be applied to turbulent flow as well as laminar flow and the bed shear stress can be obtained by integration of the equation which is the momentum integral method.

$$\tau_b = \int_{z_0}^{\delta+z_0} \frac{\partial \tau}{\partial z} dz = \rho \int_{z_0}^{\delta+z_0} \frac{\partial}{\partial t} (U_\infty - u) dz \quad (2.26)$$

where z_0 is the bottom level. Bed shear stress under wave motion is generally expressed with

the wave friction factor, f_w .

$$\tau_b = \frac{1}{2}\rho f_w U_\infty^2. \quad (2.27)$$

f_w is a function of wave amplitude (A) and roughness height (k_s), indicating that the estimation of k_s is necessary for determining the bed shear stress under wave motion.

Chapter 3. EXPERIMENTAL STUDY OF ROUGHNESS HEIGHT OVER IRREGULAR ROUGH BOTTOM

3.1 Introduction

In tidal flats, oysters form reef-like structures with complex three-dimensional surfaces known as oyster reefs. The oyster reefs develop above sediment, creating a rough surface distinct from bare sand surfaces. The formation of rough surfaces by oyster reefs significantly influences boundary layer flow and velocity over reef structures is often described by the log-law (Eq. 3.1) (Monismith, 2007; Whitman and Reidenbach, 2012; Reidenbach et al., 2013; Kitsikoudis et al., 2020; Lindhart et al., 2021).

$$\frac{u(z)}{u_*} = \frac{1}{\kappa} \ln \left(\frac{z + d'}{z_0} \right), \quad (3.1)$$

where $u(z)$ is horizontal velocity at height z ; u_* is shear velocity; κ is von Kármán constant; z_0 is hydraulic roughness height; d' is displacement thickness. z_0 is related to roughness height (k_s , $z_0 = k_s/30$). The roughness height is a crucial parameter in the log-law under rough flow regime Schlichting and Gersten (2016). Therefore, it is necessary to appropriately determine the roughness height for evaluating velocity over oyster reefs.

Oyster reefs are considered one of the major factors in nature-based solutions (Borsje et al., 2011; Scyphers et al., 2011; Morris et al., 2019; Moraes et al., 2022; La Peyre et al., 2022). From a coastal defense perspective, the oyster reefs attenuate waves and currents and stabilize shorelines (Styles, 2015; De Paiva et al., 2018; Chowdhury et al., 2019; Morris et al., 2019; Kitsikoudis et al., 2020; Morris et al., 2021). The key factor for these effects is the development of the rough surface due to oyster reefs (Wright et al., 1990; Hitzegrad et al.,

2024). Furthermore, the impacts of oyster reefs on wave attenuation and shoreline changes have been studied using numerical models (Smith et al., 2009; Housego and Rosman, 2016; Salatin et al., 2022; Hong et al., 2023; Stanley et al., 2024). In these simulations, the friction coefficient and roughness height used to account for the effects of the rough surface of oyster reefs were based on values applied to gravel or coral reefs (Van Leeuwen et al., 2010; Housego and Rosman, 2016; Hong et al., 2023) due to insufficient research on the roughness height of oyster reefs. Therefore, understanding the roughness height of oyster reefs is essential to comprehend their impact on coastal flows and the environment.

The study described in Chapter 3 aims to propose an estimation model for determining the roughness height of oyster reefs using their geometric variables, such as the height of the rough elements over oyster reef surfaces. A discrete approach is employed to estimate the roughness height rather than a continuous approach (Stewart et al., 2019). The discrete approach calculates the roughness height for individual rough elements without considering the surrounding topographical characteristics. On the other hand, the continuous approach is a method that estimates roughness height by using the statistical characteristics of surface elevation when individual rough elements are difficult to identify on a randomly rough surface (Flack and Schultz, 2010). Through surface analysis, the characteristic length of rough elements on oyster reef surfaces is estimated, thereby enhancing the relevance of the roughness predictors. To develop the roughness predictor for oyster reefs, experiments were conducted in an open channel flume (OCF) (Shin et al., 2020) for unidirectional flow and an oscillatory water tunnel (OWT) (Hwang and Park, 2023) for oscillatory flow. Artificial rough bottom models, mimicking actual oyster reef surfaces based on field measurements, were used to reproduce oyster reef conditions. The developed roughness predictor is validated by comparing the log-law velocity profile based on the calculated roughness height with the

experimentally measured velocity profile.

3.2 Methodology

3.2.1 Characteristics of oyster reef surfaces

Since this study focuses on estimating the local roughness height of oyster reefs, it is necessary to identify the geometric variables of the rough elements over the complex surfaces. The rough surface over oyster reefs is analyzed employing a method used in the bedform analysis (Van Der Mark et al., 2008; Gutierrez et al., 2013; Zomer et al., 2021). To identify individual rough elements of oyster reefs, the zero-upcrossing method is applied to the filtered surface level (or roughness level, hereinafter denoted as z_{RL}). The height variation of the rough elements (roughness level, z_{RL}) is obtained by subtracting the mean surface level from the original data, and the mean surface level is determined through empirical mode decomposition (EMD) (Huang et al., 1998). Among the decomposed intrinsic modes, the lowest frequency mode is considered the mean surface level. This method is applied to the oyster reef surface data obtained from Hitzegrad et al. (2022), which were reconstructed using the structure-from-motion (SfM) technique (Ullman, 1979). Sample contour images of the oyster reef surface and the corresponding roughness level (z_{RL}) are shown in Fig. 3.1(a),(b), respectively. The zero-upcrossing method is then applied to the roughness level to identify individual rough elements. A single rough element is defined as the interval between two neighboring zero-crossing points where the signals change from negative to positive. Subsequently, the dimensions of individual rough elements, i.e., their height (Δ_o) and length (Λ_o), are determined. These are defined as the vertical distance between the crest and the trough, and the horizontal distance between two consecutive zero-upcrossing points, respectively (see Fig. 3.1(c)).

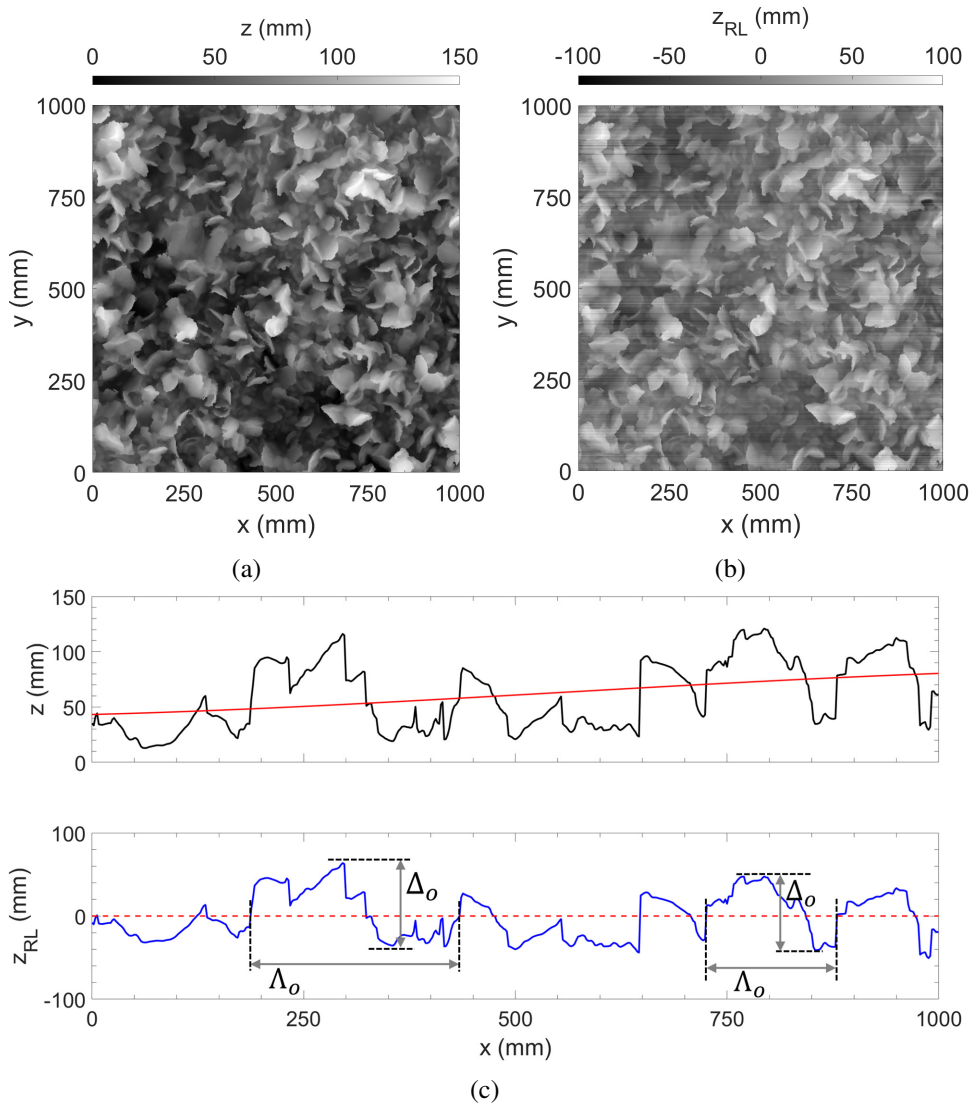
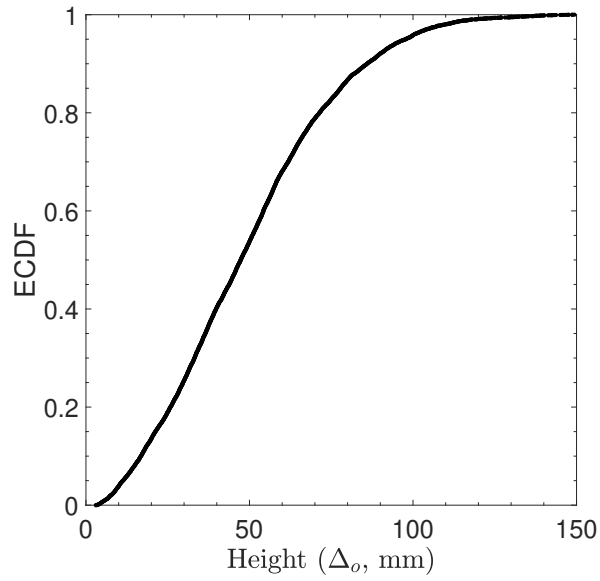
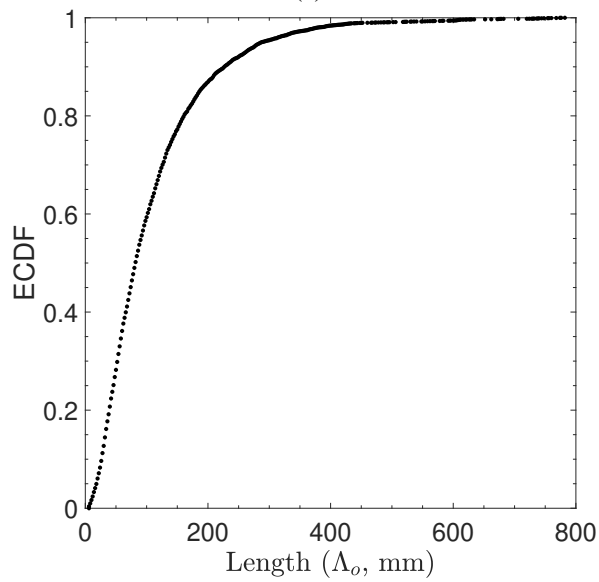


Figure 3.1: (a) Contour image of original surface data (b) Contour image of roughness level (z_{RL}) (c) Example of roughness level and definition of geometric variables of the roughness level (Black solid line: original surface profile; Red solid line: reference level; blue solid line: roughness level; red dashed line: zero-level; Δ_o : height of the rough element; Λ_o : length of the rough element)

The outlined method is applied to four datasets of oyster reef surfaces and the size distribution of rough elements is then obtained. Fig. 3.2 shows the empirical cumulative distribution function (ECDF) of the height and length of the rough elements. The average height of the rough elements is 49.6 mm, ranging from 3.0 to 149.4 mm, and the average length is 110.3 mm, ranging from 6 to 782 mm. These sizes of rough elements over the oyster reef surfaces are comparable to the scale of gravel (2-64 mm) and cobbles (64-256 mm), according to the sediment classification in Valentine (2019).



(a)



(b)

Figure 3.2: (a) ECDF of rough element height over the oyster reef surfaces (b) ECDF of rough element length over the oyster reef surfaces (ECDF: empirical cumulative distribution function)

3.2.2 Experimental setup

Experimental facility

The experiments were conducted to estimate the roughness height of oyster reefs under two different flow conditions: unidirectional flow using the OCF and oscillatory flow using the OWT. The motivation for conducting two types of experiments is that the tidal flats, where oyster reefs primarily develop, are influenced by both unidirectional flow caused by tides and oscillatory flow caused by waves. The OCF, depicted in Fig. 3.3, has dimensions of 10 m in length, 0.3 m in width, and 0.6 m in height. Water is supplied from a reservoir tank to the inlet of the flume via a pump, and the water depth is controlled by a tailgate at the downstream end of the OCF. Ten experimental rough bottom models were sequentially attached to the flume bottom starting 6 m away from the inlet to generate the turbulent flow over the rough bottom (Fig. 3.3). Further details of the experimental rough bottom models are provided in the part of rough bottom model for the experiment. Flow velocity was measured using the particle image velocimetry (PIV) with the field of view (FOV) set in the seventh row of the attached rough bottom model sequence.

Another series of experiments aims to investigate the roughness height under oscillatory flow using the OWT (Fig. 3.4). The test section of the OWT is square, with the dimensions of 0.27 m in both width and height and the horizontal length of the OWT is 4.59 m. A servo motor, mounted on a frame and moving horizontally with a 1 m excursion, generates the oscillatory flow in the test section of OWT. The reciprocating motion of the servo motor is controlled with an accuracy of $\pm 15.0 \mu\text{m}$ using SpiiPlus (ACS Motion Control). By controlling the servo motor, the velocity amplitude can be adjusted, allowing for experiments across various Reynolds numbers. Ten experimental rough bottom models were attached to

the bottom of the OWT to induce turbulent flow over the rough bottom. The FOV for the PIV was positioned in the fifth row of the attached rough bottom model sequence. Under identical flow conditions, the velocity data were collected over 15-20 wave cycles in the repeated experiments in order to obtain a phase-averaged velocity field.

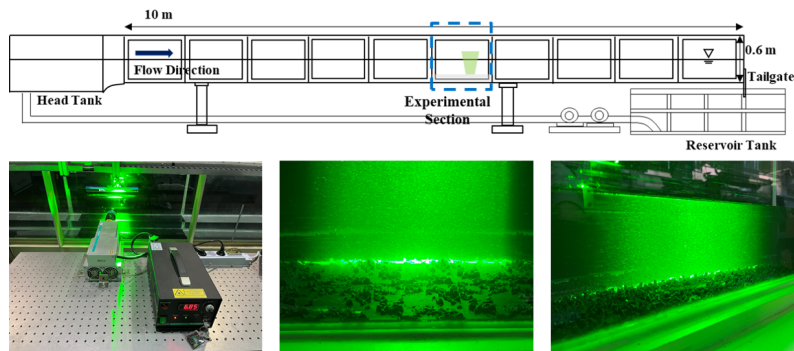


Figure 3.3: Sketch of the open channel flume and the experimental setup of the unidirectional flow experiment

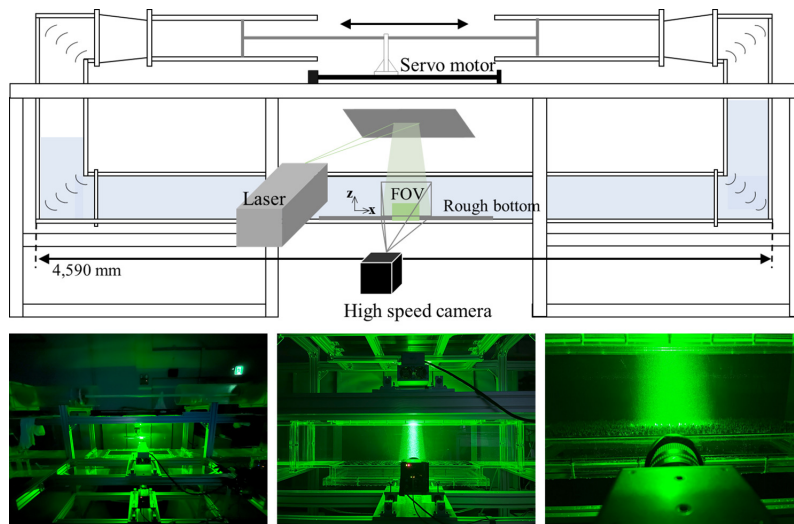


Figure 3.4: Sketch of the oscillatory water tunnel and the experiment setup of the oscillatory flow experiment

The velocity field was measured using the PIV system (Fig. 3.3 and 3.4), which comprised a continuous wave diode-pumped solid-state (CW DPSS) laser (RayPower 5W, Dantec) and a high-speed camera (FASTCAM mini UX50, Photron). Images were acquired at 1,000 frames per second with a pixel resolution of 1,280 x 1,024 and recorded using the image acquisition program (PFV4). Silver-coated hollow glass spheres with a mean particle diameter of 10 μm (S-HGS-10, Dantec) were used as the seeding particles for the PIV analysis. The PIV measurements were conducted at two or three different $x - z$ planes (u and w velocity components) in each model to capture the variability in the rough element sizes within the experimental models. The velocity fields from the captured images were obtained using PIVlab, a MATLAB toolbox (Thielicke and Sonntag, 2021). The final velocity vector was obtained using fast fourier transform (FFT) window deformation algorithm, with three iterations and 50% overlap. In the unidirectional and oscillatory flow experiments, the final interrogation window sizes were 24 x 24 and 16 x 16, respectively. This resulted in vector spacing of 1 mm for the unidirectional flow velocity fields and 0.7 mm for the oscillatory flow velocity fields.

The instantaneous velocity fields were obtained through the PIV analysis, however, the flow over rough surfaces can be spatially heterogeneous (Nikora et al., 2001). To address this, the doubly-averaged method is employed for both unidirectional and oscillatory flow conditions (Nikora et al., 2007; Coleman et al., 2008; Yuan and Madsen, 2014; Yang et al., 2015). In the unidirectional flow experiments, time and spatial averaging are performed, with time averaging based on the duration of PIV measurements. In the oscillatory flow experiments, phase and spatial averaging are conducted, with phase averaging over N wave cycles. The spatial averaging is carried out along the length of the oyster model. Consequently, the

instantaneous velocity can be decomposed as follows:

$$u_i(t) = \langle \bar{u}_i \rangle + \tilde{\tilde{u}}_i + u'_i, \quad (3.2)$$

$$u_i(t) = \langle \hat{u}_i \rangle + \tilde{\tilde{u}}_i + u'_i, \quad (3.3)$$

where t is time; u_i is instantaneous velocity at t ; \bar{u} is time-averaged velocity for the unidirectional flow; $\tilde{\tilde{u}}_i$ is spatial fluctuation of \bar{u}_i ; \hat{u}_i is phase-averaged velocity for the oscillatory flow; $\langle \rangle$ denotes spatial averaging; $\tilde{\tilde{u}}_i$ and $\tilde{\tilde{u}}_i$ is spatial fluctuation of $\langle \bar{u}_i \rangle$ and $\langle \hat{u}_i \rangle$, respectively; u'_i is turbulent fluctuation. The time-averaged velocity (Eq. 3.4) and phase-averaged velocity (Eq. 3.5) are calculated as follows:

$$\bar{u}(x, z) = \frac{1}{T} \sum u(x, z, t), \quad (3.4)$$

$$\hat{u}(x, z, \omega t) = \frac{1}{N} \sum u(x, z, \omega(t + (n-1)T_w)), \quad (3.5)$$

where x and z are horizontal and vertical coordinates; T is the duration of the PIV measurement; ω is defined as $2\pi/T_w$. the spatially averaged velocity across the rough element length with M points was then calculated as follows:

$$\langle \bar{u}(z) \rangle = \frac{1}{M} \sum \bar{u}(x, z), \quad (3.6)$$

$$\langle \hat{u}(z, \omega t) \rangle = \frac{1}{M} \sum \hat{u}(x, z, \omega T_w). \quad (3.7)$$

Rough bottom model for the experiment

Rough bottom models for the experiments were fabricated using a 3D printer (Sindoh DP200), based on the rough surface data of oyster reefs obtained from the Wadden Sea on the German side (Hitzegrad et al., 2022). To facilitate 3D printing, small fluctuations were smoothed using locally estimated scatterplot smoothing (LOESS) (Cleveland, 1979), and the dimensions were then scaled down by a factor of 0.09 in both the horizontal and vertical directions. Fig. 3.5 shows the contour images of the experimental rough bottom models and the surface profiles at the PIV measurement section. Additionally, in the PIV measurement sections, the rough elements used to estimate the roughness height are marked in green and each rough element is assigned a label accordingly. Hereafter, the rough element over the experimental rough bottom model is referred to as the oyster model. The oyster models in the unidirectional flow and oscillatory flow experiment are labeled with serial numbers prefixed with R (e.g., R1, R2, R3) and RW (e.g., RW1, RW2, RW3), respectively. Due to the surface irregularity, some smaller rough elements are hidden behind the larger ones, resulting in the omission of velocity data near the top of small rough elements. This is because the high-speed camera was installed parallel to the experimental flumes (OCF and OWT) for the PIV measurements. Consequently, only the oyster models where the flow near the top is measurable are included in the estimation of roughness height. By analyzing the relationship between the size information of the oyster models (Δ_o and Λ_o) and the calculated roughness height, the roughness predictor for oyster reefs is developed.

To assess the scale effect of the derived roughness predictors, two differently scaled rough bottom models (RBC3 and RBW3 illustrated in Fig. 3.6) were also used in the experiments. RBC3 and RBW3 are distorted models reduced by a scale factor of 0.09 horizontally and 0.18 vertically. The oyster models considered in the analysis are highlighted

in green and marked with numbers in Fig. 3.6. The oyster models of RBC3 and RBW3 are labeled with the serial numbers prefixed with RV (e.g., RV1, RV2) and RVW (e.g., RVW1, RVW2), respectively.

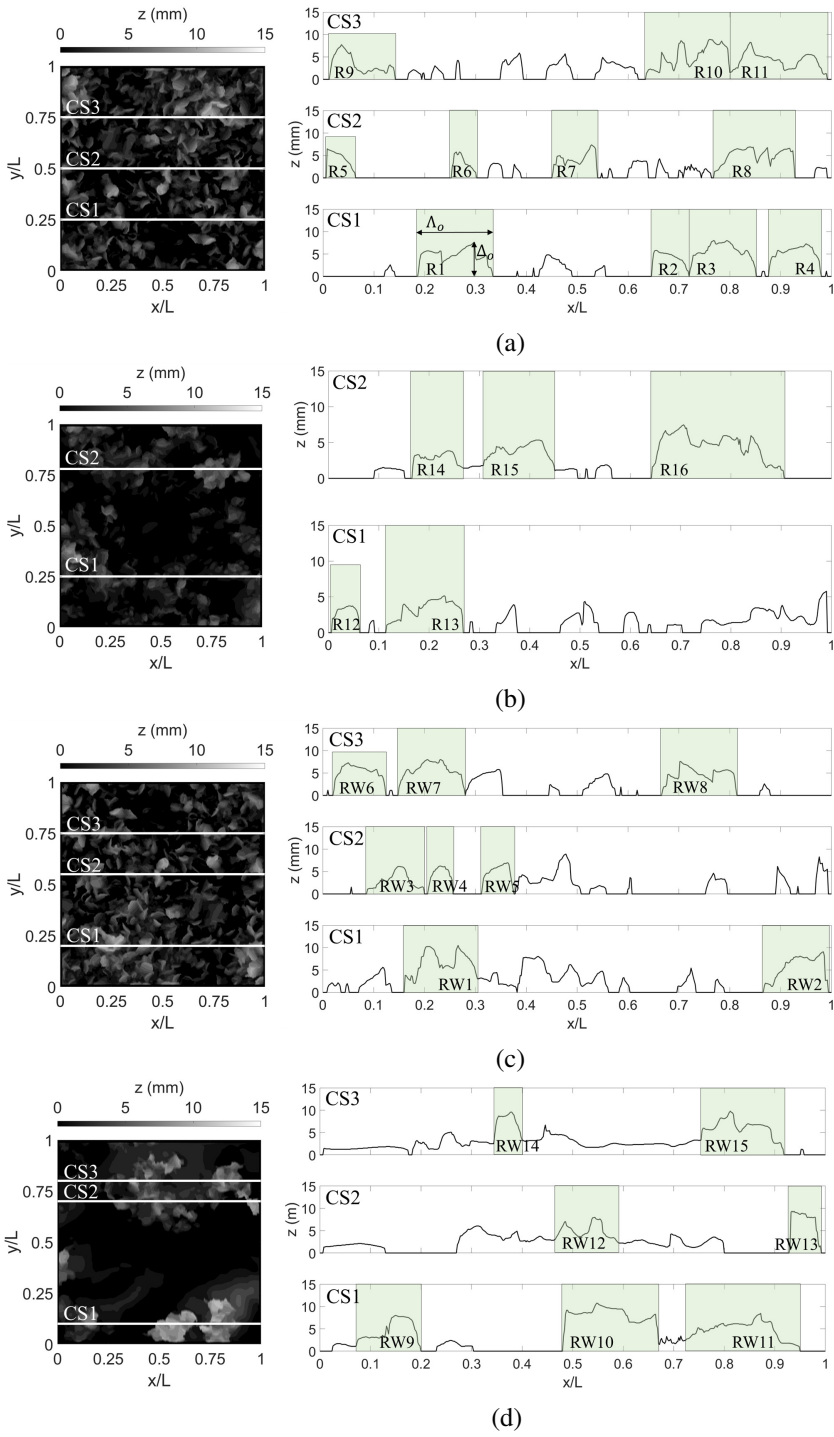


Figure 3.5: Contour images of the experimental rough bottom models and the PIV measurement sections over the rough bottom models (a) RBC1 (b) RBC2 (c) RBW1 (d) RBW2

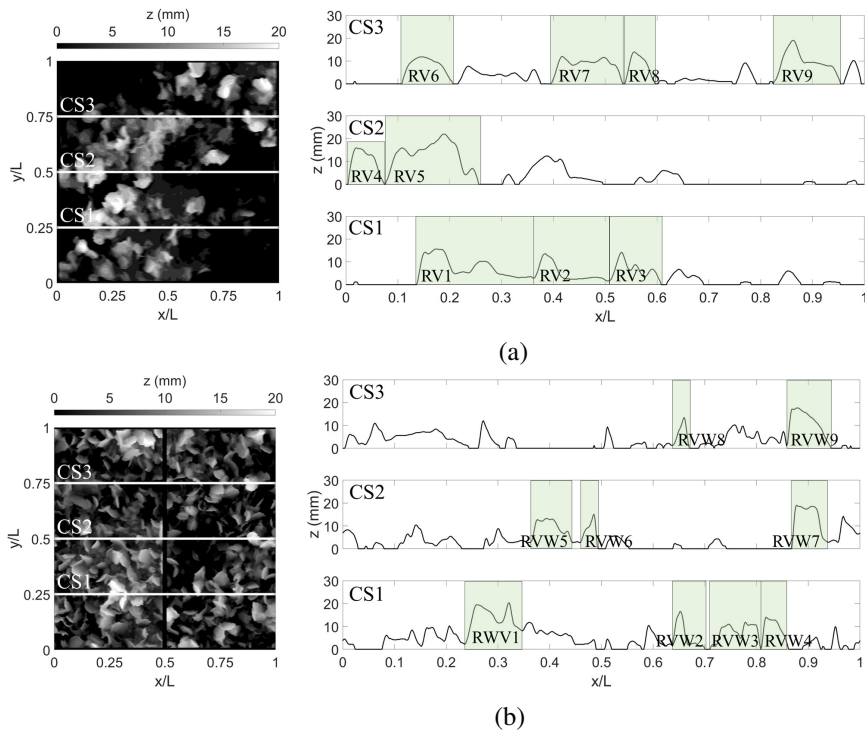


Figure 3.6: Contour images of the experimental rough bottom models and the PIV measurement sections for investigating the scale effect of roughness predictor (a) RBC3 (b) RBW3

Experimental cases

The unidirectional flow experiments were conducted under a total of 24 experimental conditions, which were a combination of 8 different flow conditions and 3 different rough bottom conditions (Table 3.1). The water depth was set to two conditions, 0.1 m and 0.15 m. For each water depth condition, flow discharges were adjusted resulting in an average flow velocity ranging from 0.13 to 0.33 m/s. The three different rough bottom models (RBC1, RBC2, and RBC3) incorporate the oyster models of varying sizes. The roughness heights are estimated for the oyster models with the heights ranging from 3.8 to 22 mm and lengths from 25 to 113 mm.

The oscillatory flow experiment consists of 9 different cases, as detailed in Table 3.2, including different velocity amplitudes ranging from 0.15 to 0.27 m/s and three different rough bottom conditions under sine wave conditions with a constant wave period ($T_w = 3$). In these experiments, the roughness heights are estimated for the oyster models with heights ranging from 5.8 to 20.3 mm and lengths from 25 to 115 mm. The flow regime for the OWT experiments is examined in terms of Reynolds number and the relative roughness height (A/k_s) (Fig. 3.7). Here, A ($A = U_\infty T_w / 2\pi$) is the orbital amplitude, which can be determined from the freestream velocity. The Reynolds numbers for the OWT experiments range from 9,000 to 35,000. Under these experimental conditions, the flow is situated in the transitional and very rough turbulent zone with low relative roughness height conditions, $A/k_s < 10$.

Table 3.1: Experimental cases under the unidirectional flow over rough bottom conditions

Case	Water depth (h), m)	Average velocity (U), m/s)	Reynolds number ($Re = Uh/u$)	Rough bottom model	Oyster model height (mm) length (mm)	
U20h10R1	0.10	0.20	20,000	RBC1	5.8-8.9	25-96
U24h10R1	0.10	0.24	24,000	RBC1	5.8-8.9	25-96
U27h10R1	0.10	0.27	27,000	RBC1	5.8-8.9	25-96
U33h10R1	0.10	0.33	33,000	RBC1	5.8-8.9	25-96
U13h15R1	0.15	0.13	19,500	RBC1	5.8-8.9	25-96
U15h15R1	0.15	0.15	22,500	RBC1	5.8-8.9	25-96
U17h15R1	0.15	0.17	25,500	RBC1	5.8-8.9	25-96
U21h15R1	0.15	0.21	31,500	RBC1	5.8-8.9	25-96
U20h10R2	0.10	0.20	20,000	RBC2	3.8-7.5	28-132
U24h10R2	0.10	0.24	24,000	RBC2	3.8-7.5	28-132
U27h10R2	0.10	0.27	27,000	RBC2	3.8-7.5	28-132
U33h10R2	0.10	0.33	33,000	RBC2	3.8-7.5	28-132
U13h15R2	0.15	0.13	19,500	RBC2	3.8-7.5	28-132
U15h15R2	0.15	0.15	22,500	RBC2	3.8-7.5	28-132
U17h15R2	0.15	0.17	25,500	RBC2	3.8-7.5	28-132
U21h15R2	0.15	0.21	31,500	RBC2	3.8-7.5	28-132
U20h10R3	0.10	0.20	20,000	RBC3	11.8-22.0	29-113
U24h10R3	0.10	0.24	24,000	RBC3	11.8-22.0	29-113
U27h10R3	0.10	0.27	27,000	RBC3	11.8-22.0	29-113
U33h10R3	0.10	0.33	33,000	RBC3	11.8-22.0	29-113
U13h15R3	0.15	0.13	19,500	RBC3	11.8-22.0	29-113
U15h15R3	0.15	0.15	22,500	RBC3	11.8-22.0	29-113
U17h15R3	0.15	0.17	25,500	RBC3	11.8-22.0	29-113
U21h15R3	0.15	0.21	31,500	RBC3	11.8-22.0	29-113

Table 3.2: Experimental cases under the oscillatory flow over rough bottom conditions

Case	Wave type	Wave period (T_w), s)	Free stream velocity (U_∞), m/s)	Reynolds number ($Re = U_\infty^2 T / 2\nu$)	Rough bottom model	Oyster model height (mm) length (mm)	
U15R1	Sine	3	0.15	10,743	RBW1	5.8-10.5	25-90
U19R1	Sine	3	0.19	17,236	RBW1	5.8-10.5	25-90
U22R1	Sine	3	0.22	23,109	RBW1	5.8-10.5	25-90
U27R1	Sine	3	0.27	34,807	RBW1	5.8-10.5	25-90
U19R2	Sine	3	0.19	17,236	RBW2	8.0-10.8	31-115
U22R2	Sine	3	0.22	23,109	RBW2	8.0-10.8	31-115
U27R2	Sine	3	0.27	34,807	RBW2	8.0-10.8	31-115
U14R3	Sine	3	0.14	9,358	RBW3	11.9-20.3	18-56
U21R3	Sine	3	0.21	21,056	RBW3	11.9-20.3	18-56

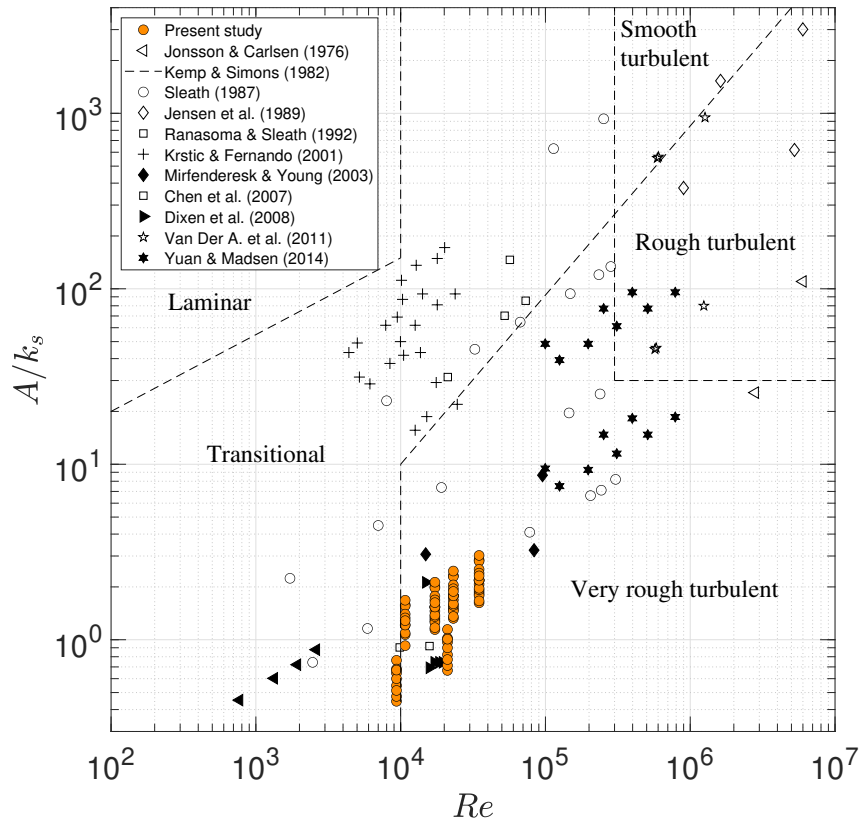


Figure 3.7: Flow regime for the oscillatory flow experiments in $Re - A/k_s$ space (Orange marker: the experimental conditions in this study)

3.2.3 Roughness height and friction factor

The roughness height can be parameterized by the characteristic length of the rough element. For example, the grain roughness height ($k_{s,g}$) can be estimated using the representative grain diameter (d_*) as $k_{s,g} = \alpha d_*$ (Yen, 2002). In oscillatory flow conditions, the grain roughness height was estimated based on experimental measurements and then used in the calculation of bed shear stress, with various formulations such as $k_{s,g} = 2.5d_{50}$ (O'Donoghue and Wright, 2004); $k_{s,g} = 2.38d_{50}$ and $k_{s,g} = 2.44d_{50}$ (Van Der A et al., 2011); $k_{s,g} = 15d_{50}$ (Abreu et al., 2013); $k_{s,g} = 1.3d_{50}$ (O'Donoghue et al., 2021). On the other hand, the form roughness height ($k_{s,f}$) can be calculated using the bedform height (Δ_f) and length (Λ_f) (Van Rijn, 1993; Soulsby, 1997; Bartholdy et al., 2010), with additional consideration given to the lee side angle of bedform by Lefebvre and Winter (2016).

The local roughness height can be estimated using the log-law (Eq. 3.1), and the bed shear stress can be calculated from the shear velocity (Eq. 3.8),

$$\tau_b = \rho u_*^2, \quad (3.8)$$

where ρ is the water density. Both u_* and z_0 are treated as fitting parameters, and their values can be estimated by fitting Eq. 3.1, thereby leading to the estimation of the roughness height of each rough element. In the unidirectional flow, the roughness heights for oyster models are determined through the doubly-averaged velocity profile (time and spatial averaging). In the oscillatory flow, the log-law fitting is performed using the instantaneous doubly-averaged velocity profile (phase and spatial averaging), leading to variations in roughness heights over the wave cycle. The mean of the temporally varied roughness height is defined as the

representative roughness height for the considered oyster model see, e.g., Van Der A et al. (2011).

In oscillatory flow, the wave bed shear stress ($\tau_{b,w}$) is often expressed in a velocity quadratic form (Eq. 3.9), in which the wave friction factor (f_w) (Eq. 3.10) can be calculated from the wave bed shear stress.

$$\tau_{b,w} = \frac{1}{2} \rho f_w U_\infty^2, \quad (3.9)$$

$$f_w = \frac{2 \max(\tau_{b,w}(t))}{\rho U_\infty^2}. \quad (3.10)$$

where U_∞ is freestream velocity. The wave friction factor can be formulated as the function of A/k_s (Swart, 1974; Dixen et al., 2008; Humbyrd, 2012). Swart (1974) proposed a semi-empirical formula for the wave friction factor (Eq. 3.11). Dixen et al. (2008) obtained an empirical formula based on the experimental data in the range of A/k_s between 0.2 and 10 (Eq. 3.12). Humbyrd (2012) explicitly derived a formula depending on the range of A/k_s and the equation corresponding to the range of A/k_s in the present experiment is presented in Eq. 3.13.

$$f_w = \exp [5.213 (A/k_s)^{-0.194} - 5.977], \quad (3.11)$$

$$f_w = 0.32(A/k_s)^{-0.8}, \quad (0.2 < A/k_s < 10), \quad (3.12)$$

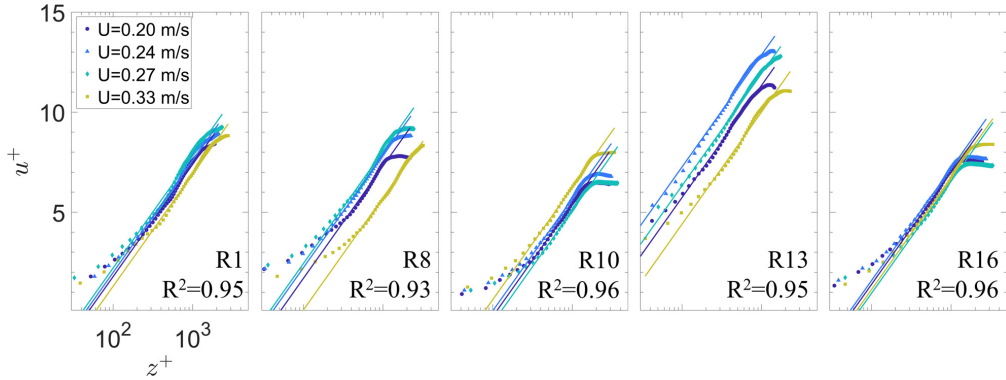
$$f_w = \exp [-1.69 (A/k_s)^{0.344} - 0.473] + 0.0388 \quad (0.342 < A/k_s \leq 10). \quad (3.13)$$

The relationship between f_w and A/k_s for the experiment conditions conducted in this study is further discussed in Chapter 3.4.2.

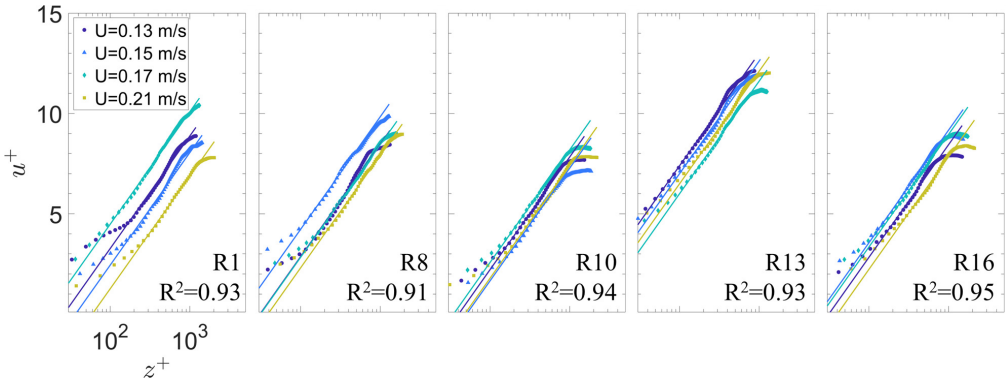
3.3 Results

3.3.1 Roughness height under unidirectional flow

The roughness heights of the oyster models marked in Fig. 3.5(a),(b) are estimated through the log-law fitting under the unidirectional flow. For the log-law fitting, the doubly-averaged velocity profile within the boundary layer is utilized. The boundary layer thickness is determined by δ_{99} , defined as a level where $u = 0.99u_\infty$. Due to the influence of oyster models, the velocity near the bottom may not conform to the log-law (Powell, 2014). Therefore, the velocity data near the top of the oyster models are excluded from the log-law fitting process. To evaluate the accuracy of the estimated roughness height, the fitted logarithmic velocity profiles are compared to the PIV-measured velocity profile. The velocity distributions over selected oyster models are plotted against the non-dimensional parameters, z^+ ($z^+ = u_*z/\nu$) and u^+ ($u^+ = u/u_*$) (Fig. 3.8). The fitted logarithmic velocity profiles show good agreement with the measured velocity, except for the regions where the log-law is not followed, achieving a mean of coefficient of determination (R^2) values of 0.94 with a standard deviation of 0.03. These results indicate that suitable estimations for the shear velocity and roughness height are made during the log-law fitting process, enabling the representation of measured velocity distribution over the oyster models.



(a)



(b)

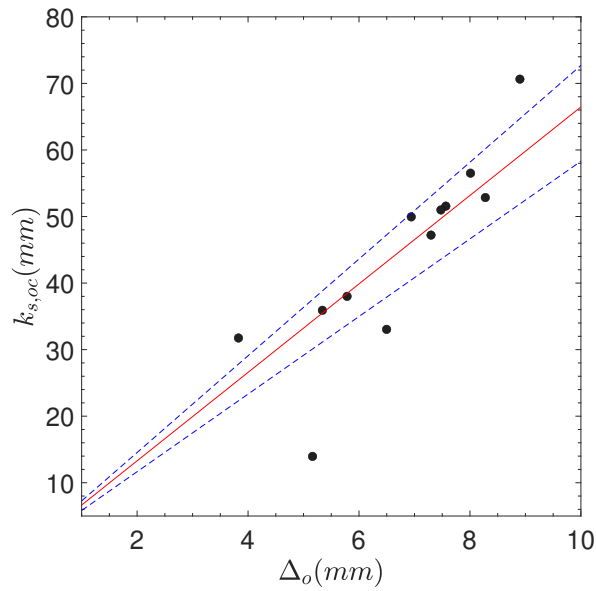
Figure 3.8: The PIV-measured velocity profiles and corresponding fitted logarithmic velocity profiles over selected oyster models (R1, R8, R10, R13, and R16) in RBC1 and RBC2 (a) Experiments with a water depth of 0.1 m (b) Experiments with a water depth of 0.15 m (Color markers: the PIV-measured velocity; Color solid lines: the fitted logarithmic velocity profile)

The correlation between the estimated roughness height and geometric variables of the oyster models is examined. From this analysis, a formula for calculating roughness height is derived with the characteristic length chosen as Δ_o and Δ_o^2/Λ_o , considering the variables in the grain roughness predictor and form roughness predictor (Van Rijn, 1993; Yen, 2002; López and Barragán, 2008; Bartholdy et al., 2010; Lefebvre and Winter, 2016). The estimated roughness heights for the twelve oyster models (R1-R6, R8, R10, R11, R13, R15, and R16) are plotted against both Δ_o (Fig. 3.9(a)) and Δ_o^2/Λ_o (Fig. 3.9(b)), with their regression lines depicted as the red solid lines, and the derived formulas are as follows:

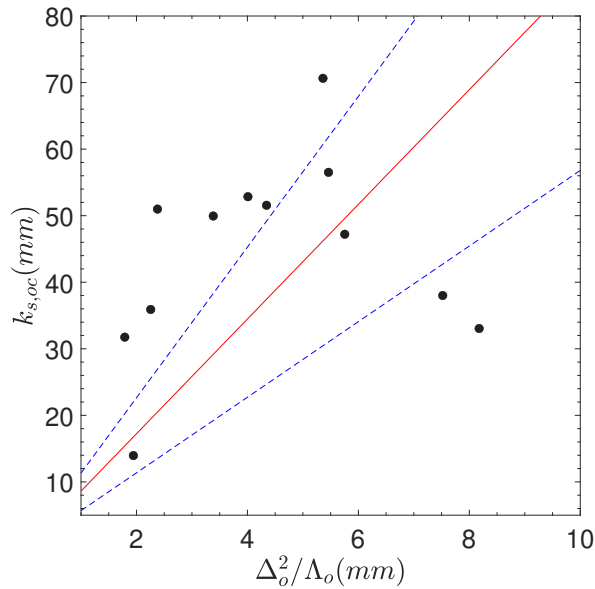
$$k_{s,oc} = 6.6\Delta_o, \quad (3.14)$$

$$k_{s,oc} = 8.5\Delta_o^2/\Lambda_o, \quad (3.15)$$

where $k_{s,oc}$ is the roughness height of the oyster model under unidirectional flow condition. Δ_o has a higher correlation with the roughness height, with R^2 of 0.69 (Eq. 3.14), compared to Δ_o^2/Λ_o (Eq. 3.15).



(a)

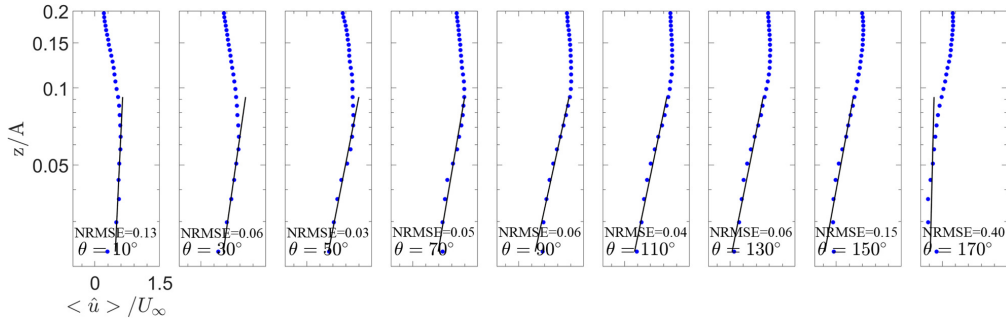


(b)

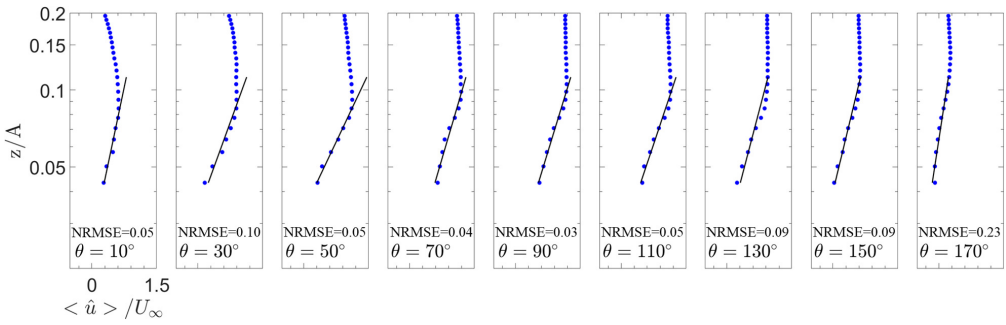
Figure 3.9: The relationship between the dimensional variables of the oyster model and the roughness height in the unidirectional flow (a) Roughness height as a function of the height of the rough element (Δ_o) (b) Roughness height as a function of height and length of the rough element (Δ_o^2/Λ_o) (Red solid line: regression line between the roughness height and the geometric variables; Blue dashed line: lower and upper bound of the 95% confidence interval)

3.3.2 Roughness height under oscillatory flow

In the same manner, the roughness heights are estimated through the log-law fitting, and a roughness predictor is examined under the oscillatory flow. In the oscillatory flow, the log-law may not be applicable in some phases, for example, when the opposite directional flows occur between the boundary layer flow and freestream flow due to an adverse pressure gradient. The velocity within the boundary layer can be larger than freestream velocity, limiting the applicability of the log-law to specific regions near the bottom (Van Der A et al., 2011; Yuan and Madsen, 2014). Therefore, considering these factors, the fitting of the logarithmic velocity profile is performed using the velocity points below the overshooting velocity level where maximum velocity occurs. For example, as shown in Fig. 3.10, the log-law is appropriately applied in oscillatory flow within the phase range of 10° to 150° , therefore, the representative roughness height is determined by averaging the roughness heights estimated within this phase range. The accuracy of the fitted logarithmic velocity is assessed using the normalized root mean square error (NRMSE) for the fifteen oyster models in RBW1 and RBW2. NRMSE is calculated by dividing root mean square error (RMSE) by the mean of the experimental values. The mean NRMSE is 0.08, with a standard deviation of 0.02, indicating that the fitted logarithmic velocities accurately represent the PIV-measured velocities under the oscillatory flow as well. In other words, the two parameters, u_* and z_0 , are accurately determined, thus the estimated roughness heights are utilized to develop the roughness predictor for the oyster reefs.



(a)



(b)

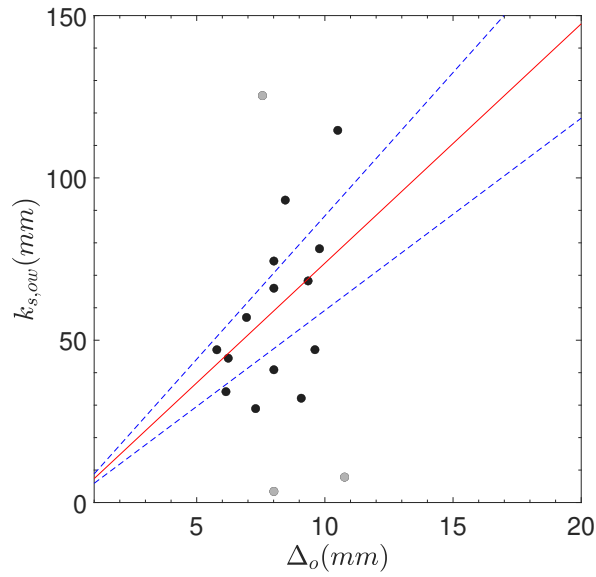
Figure 3.10: Example of the logarithmic velocity profile with the corresponding measured velocity at selected phases over oyster models (a) RW7 (Experimental case: U22R1) (b) RW15 (Experimental case: U22R2) (Blue dot: the PIV-measured velocity; Black solid line: the fitted logarithmic velocity profile)

Fig. 3.11 shows the relationship between the roughness height and geometric variables of the oyster model (Δ_o and Δ_o^2/Λ_o) in the OWT experiment. Three points marked in gray in Fig. 3.11 indicate instances where the roughness height is either overestimated or underestimated. The inclusion or exclusion of these points in deriving the roughness predictor (Eq. 3.16 and Eq. 3.17) has a negligible impact on the coefficients, with a difference of less than 10%. To accurately represent the dependence of roughness height on the geometric variables, the formulas derived from the data excluding these points are presented as follows:

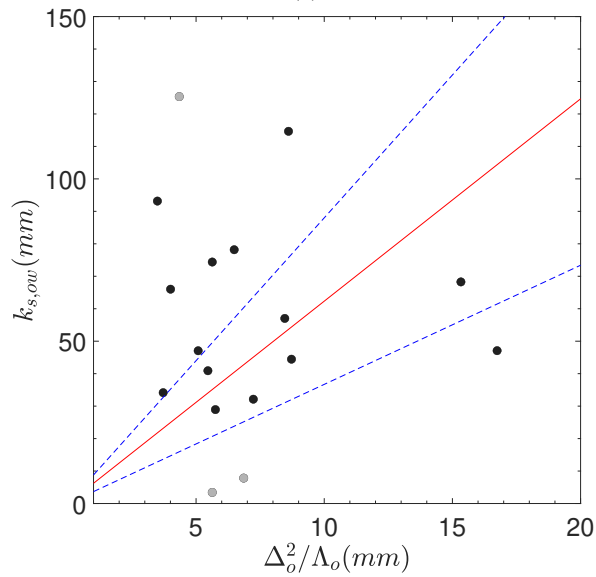
$$k_{s,ow} = 7.4\Delta_o, \quad (3.16)$$

$$k_{s,ow} = 6.2\Delta_o^2/\Lambda_o, \quad (3.17)$$

where $k_{s,ow}$ is the roughness height under oscillatory flow condition. The roughness height has a higher correlation with Δ_o ($R^2=0.31$) compared to Δ_o^2/Λ_o . It can be concluded that the roughness height under oscillatory flow is better represented by Δ_o .



(a)



(b)

Figure 3.11: The relationship between the geometric variables of the oyster model and roughness height in the oscillatory flow (a) Roughness height against Δ_o (b) Roughness height against Δ_o^2/Λ_o (Red solid line: the regression line between the roughness height and the geometric variables; Blue dashed line: lower and upper bound of 95% confidence interval)

3.4 Discussion

3.4.1 Validity and scale effect of roughness predictor in unidirectional flow

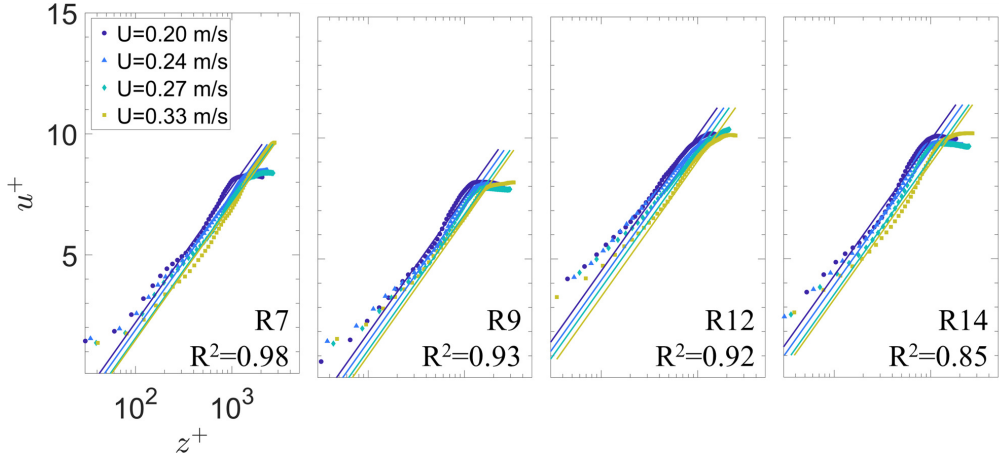
To validate Eq. 3.14, log-law fitting is performed using calculated roughness heights, which are presented in Table 3.3. In the process of the log-law fitting, u_* is only set as the free parameter, while z_0 is assigned based on calculated roughness height ($k_{s,oc}$). The comparison between the fitted logarithmic velocity profiles and PIV-measured velocity for the four oyster models (R7, R9, R12, and R14) are shown in Fig. 3.12. These four oyster models are not included in deriving Eq. 3.14. The fitted logarithmic velocity profiles show good agreement with the PIV-measured velocities, except for velocities outside the boundary layer and near the bottom, which are excluded from the log-law fitting. The mean R^2 for all fitting results is 0.95 with a standard deviation of 0.05, indicating that the roughness predictor (Eq. 3.14) reliably estimates the roughness height of the oyster model.

To examine the scale effect of Eq. 3.14, the log-law fitting is performed over the oyster models in RBC3 (RV1-RV9). The roughness heights used for the log-law fitting are provided in Table 3.3. The scale of oyster models in RBC3 differs from those in RBC1 and RBC2, being 2.5 to 3.2 times larger. The fitting results are shown in Fig. 3.13. Despite employing a different scale from those used in deriving Eq. 3.14, the fitted logarithmic velocity profile accurately represents the measured velocity profile, with R^2 values ranging from 0.81 to 0.99 (Mean of R^2 : 0.95). On the other hand, the logarithmic profile of RV5 failed to represent the measured velocity. This discrepancy may be attributed to the relatively large height of RV5, which has a height-to-depth ratio of 0.22 in case of $h=0.1$ m and 0.15 in case of $h=0.15$ m. This is because the log-law may not be applicable if the ratio of the height of the rough element to water depth is large (Powell, 2014). The overall results suggest that the roughness

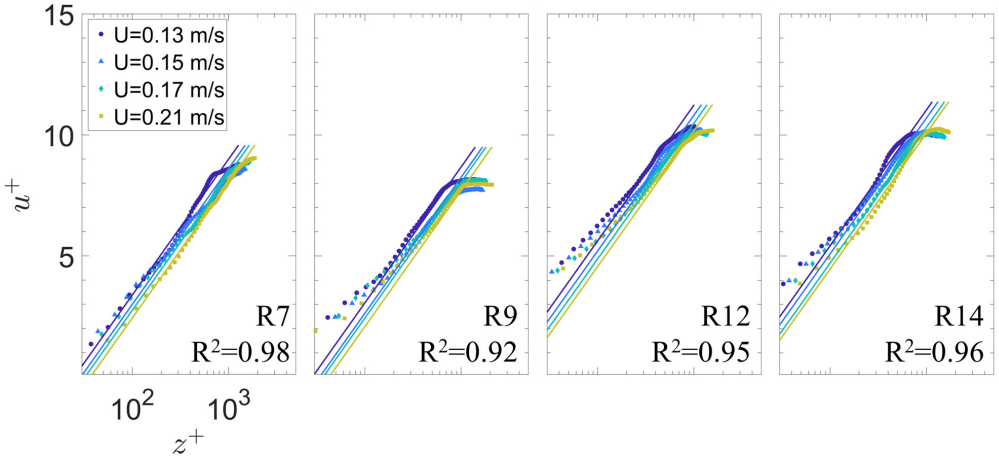
predictor (Eq. 3.14) proposed in this study is reliable in estimating local roughness height on the oyster reef surface. It is expected that this roughness predictor, derived under the unidirectional flow conditions, is primarily applicable in environments where tidal currents predominate.

Table 3.3: Roughness height ($k_{s,oc}$) calculated from Eq. 3.14 over the experimental rough surfaces for the unidirectional flow experiments (unit: mm)

RBC1	R1	R2	R3	R4	R5	R6	R7	R8	R9	R10	R11
$k_{s,oc}$	75	55	80	72	63	55	73	68	77	90	83
RBC2	R12	R13	R14	R15	R16						
$k_{s,oc}$	32	48	33	50	74						
RBC3	RV1	RV2	RV3	RV4	RV5	RV6	RV7	RV8	RV9		
$k_{s,oc}$	103	90	94	106	145	78	79	92	125		

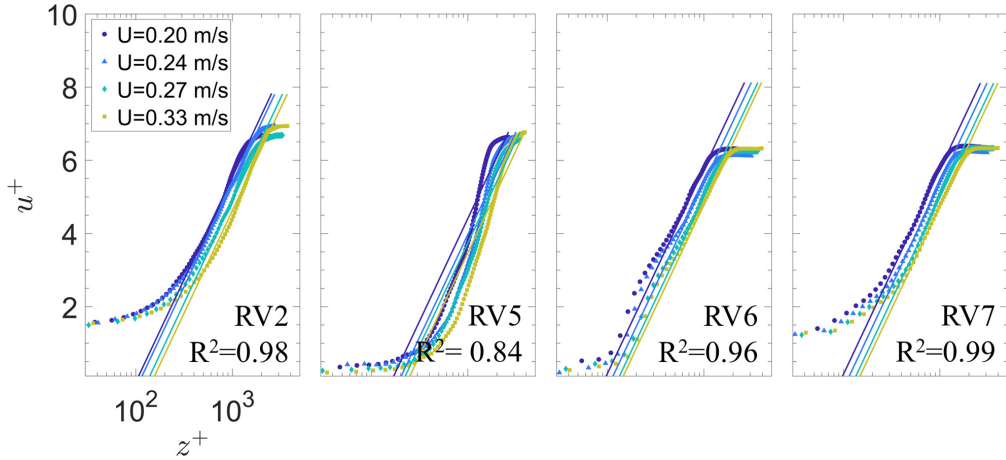


(a)

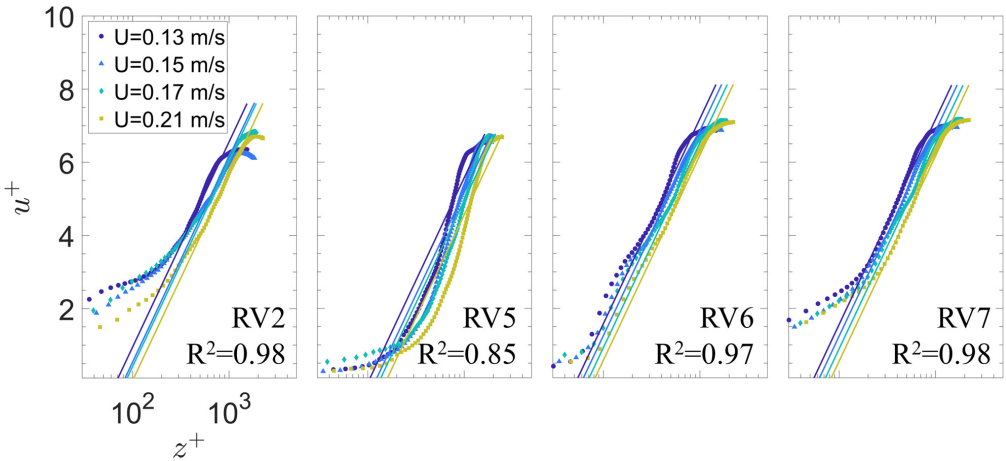


(b)

Figure 3.12: Comparison between the PIV-measured velocity profile and the logarithmic velocity profile over the oyster models (R7, R9, R12, and R14) in RBC1 and RBC2 to validate the roughness predictor (Eq. 3.14) (a) Unidirectional flow experiments with a water depth of 0.1 m (b) Unidirectional flow experiments with a water depth of 0.15 m (Color marker: the PIV-measured velocity; Color solid line: the fitted logarithmic velocity profile)



(a)



(b)

Figure 3.13: Comparison between the PIV-measured velocity profile and the logarithmic velocity profile over the oyster models (RV2, RV5, RV6, and RV7) in RBC3 to assess the scale effect of the roughness predictor (Eq. 3.14) (a) Unidirectional flow experiments with a water depth of 0.1 m (b) Unidirectional flow experiments with a water depth of 0.15 m (Color marker: the PIV-measured velocity; Color solid line: the fitted logarithmic velocity profile)

3.4.2 Validity and scale effect of roughness predictor in oscillatory flow

Similar to the validation in the unidirectional flow condition, the roughness heights calculated from Eq. 3.16 are substituted into z_0 for fitting the log-law. The fitted logarithmic velocity profiles are then compared to the PIV-measured velocities. The log-law fitting is performed on the velocities over the oyster models used to derive Eq. 3.16 and on the velocities over the oyster models in RBW3 in order to examine the scale effect. Table 3.4 presents the roughness heights of the oyster models for RBW1, RBW2 and RBW3. The oyster models in RBW3 are up to 3.5 times larger than those in RBW1 and RBW2 which were used to derive Eq. 3.16. Fig. 3.14 shows the comparison between the PIV-measured velocity and the fitted logarithmic velocity at the selected phase. The log-law fitting results, with the constant roughness height, well represent the oscillatory flow over the oyster models. The mean NRMSE is 0.16, with a standard deviation of 0.09. Additionally, the fitted logarithmic velocities over the oyster models in RBW3 also accurately represent the oscillatory flow. In other words, although the roughness predictor (Eq. 3.16) is derived at a scale 0.09 times smaller than the actual oyster reef surfaces, it can be applied to different scales as well.

Table 3.4: The roughness height ($k_{s,ow}$) of rough elements calculated from Eq. 3.16 over the experimental rough surfaces for the oscillatory flow experiments (unit: mm)

RBW1	RW1	RW2	RW3	RW4	RW5	RW6	RW7	RW8	
$k_{s,ow}$	78	67	45	46	51	54	59	56	
RBW2	RW9	RW10	RW11	RW12	RW13	RW14	RW15		
$k_{s,ow}$	59	80	63	59	69	71	72		
RBW3	RVW1	RVW2	RVW3	RVW4	RVW5	RVW6	RVW7	RVW8	RVW9
$k_{s,ow}$	151	123	88	104	99	112	141	100	131

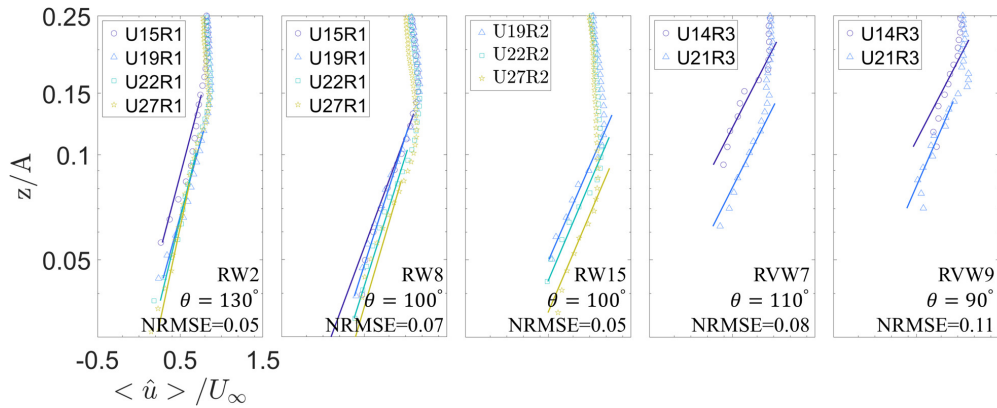


Figure 3.14: Comparison between the PIV-measured velocity profile and the fitted logarithmic velocity profile at selected phase over the oyster models under the oscillatory flow condition (RW2, RW8, RV15, RVW7, and RVW9) (Marker: the PIV-measured velocity; Solid line: the fitted logarithmic velocity profile)

3.4.3 Unified roughness predictor

In certain oyster species, it has been reported that their shape parameters are highly correlated (Bellaaj-Zouari et al., 2012). An analysis of 21 datasets of oyster reef surfaces (Hitzegrad et al., 2022) shows that the ratio of rough element height to length mostly falls below 5 (Fig. 3.15). Additionally, compared to the aspect ratio of the bedforms ranging from 0.01 to 0.1 (Venditti, 2013), the aspect ratio of roughness element on oyster reefs (Δ_o/Λ_o) is mostly above 0.1, indicating a higher aspect ratio than those of the bedforms. Furthermore, individual rough elements on the oyster reef surfaces are densely developed, which can deteriorate the relationship between Δ_o/Λ_o and the length of the separation zone. Therefore, the aspect ratio, used to parameterize the form drag influence over the bedforms (Lefebvre et al., 2014), may not be appropriate for estimating $k_{s,o}$. The experimental results in this study also show that focusing solely on Δ_o provides a more accurate measure of the roughness height. Based on these results, the roughness predictor is examined as a function of Δ_o , which is robustly applicable to both the unidirectional and oscillatory flows.

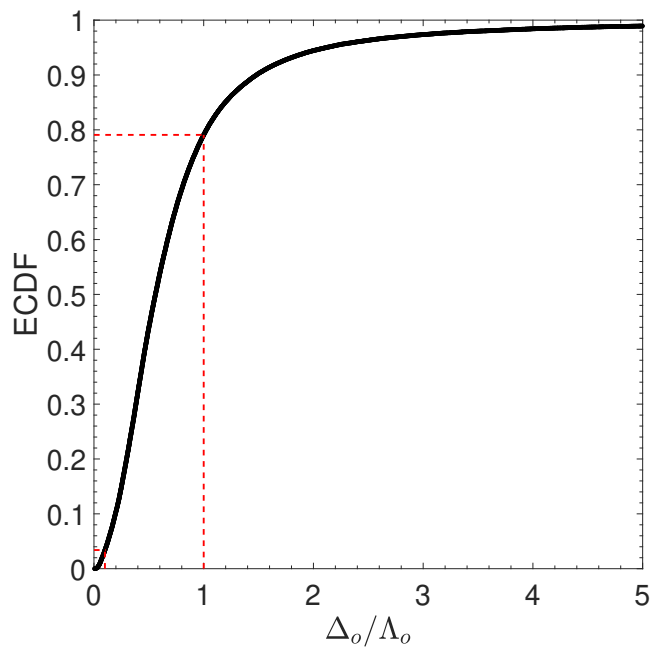
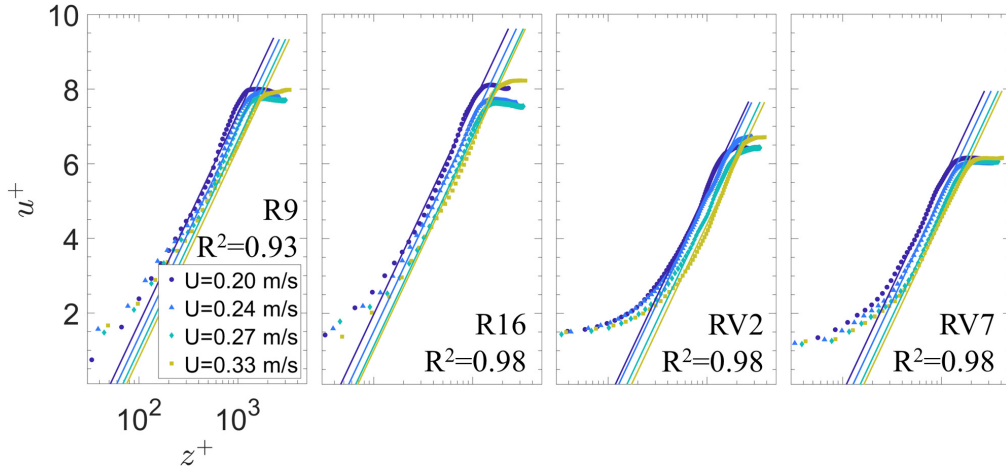


Figure 3.15: ECDF for the height and length of rough elements on the oyster reef surfaces

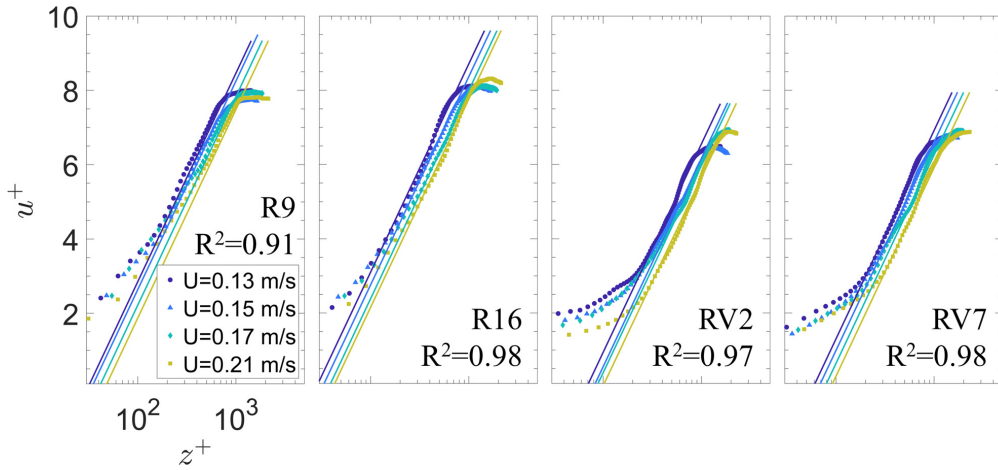
In the unidirectional flow, the estimated roughness height is 6.6 times the roughness height, with a 95% confidence interval ranging from 5.8 to 7.3. In the oscillatory flow, the roughness height is calculated as 7.4 times the roughness height, with a 95% confidence interval ranging from 5.9 to 8.8. Considering that the confidence intervals for the coefficient of the roughness predictor overlap in the unidirectional flow and oscillatory flow, it is feasible to use the same roughness predictor to calculate the roughness height under both flow conditions and the unified roughness predictor is suggested as follows:

$$k_{s,o} = 7\Delta_o. \quad (3.18)$$

To validate the unified roughness predictor, the log-law fitting is performed using the roughness height calculated from Eq. 3.18 for all considered oyster models in both the unidirectional flow and oscillatory flow experiments. The fitting results show good agreement with the PIV-measured velocities. Fig. 3.16 and Fig. 3.17 depict the fitted logarithmic velocity and the PIV-measured velocity. For the unidirectional flow, the fitting results have an R^2 range of 0.77 to 0.99, with a mean value of 0.96. In the oscillatory flow, the mean NRMSE for the log-law fitting is 0.18 with a standard deviation of 0.14. Based on these results, it is concluded that the fitted logarithmic velocity accurately represents the PIV-measured velocity, and Eq. 3.18 rationally determines the roughness height to represent velocity distribution over the oyster models.



(a)



(b)

Figure 3.16: Comparison between the PIV-measured velocity and the fitted logarithmic velocity over the oyster models (R9, R16, RV2, and RV7) to validate the unified roughness predictor (Eq. 3.18) under unidirectional flow condition (a) Experiments with the water depth of 0.1 m (b) Experiments with the water depth of 0.15 m (Color marker: the PIV-measured velocity; Color solid line: the fitted logarithmic velocity profile)

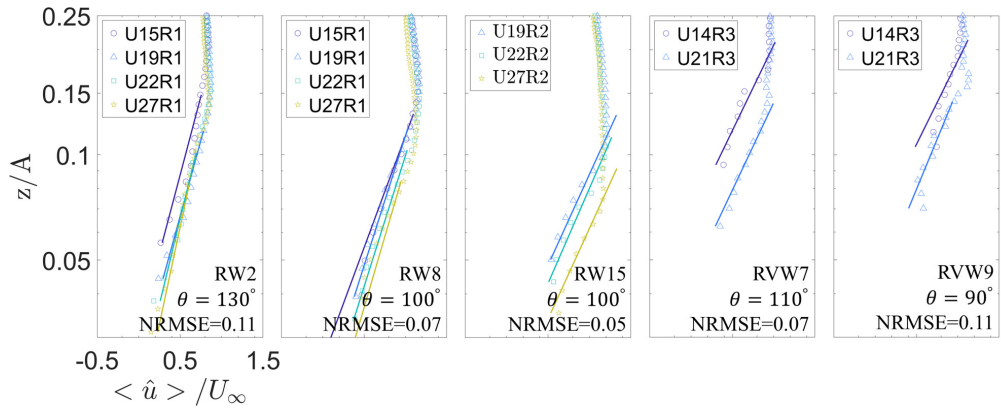


Figure 3.17: Comparison between the PIV-measured velocity and the fitted logarithmic velocity over the oyster models (RW2, RW8, RW15, RVW7, and RVW9) to validate the unified roughness predictor (Eq. 3.18) under the oscillatory flow condition (Marker: measured velocity; Solid line: fitted logarithmic velocity profile)

In the oscillatory flow, the roughness height is associated with the wave friction factor and boundary layer thickness (Van Der A et al., 2011). Therefore, the relationships between the roughness height calculated from Eq. 3.18 and these two features are examined in order to evaluate the appropriateness of the calculated roughness height under the oscillatory flow conditions. This evaluation also includes comparisons with the results from previous studies to affirm the appropriateness of estimated roughness height.

The wave friction factor is inversely related to the relative roughness height, $f_w \sim (A/k_s)^{-1}$ (Swart, 1974), which has been confirmed by various experiments and numerical studies (Dixen et al., 2008; Van Der A et al., 2011; Yuan and Madsen, 2014; O'Donoghue et al., 2021; Dunbar et al., 2023). The relative roughness heights range from 1 to 10 for RBW1 and RBW2, and from 0.1 to 1 for RBW3. These results lie between those observed in Dixen et al. (2008) and other oscillatory flow experiments (Sleath, 1987; Van Der A et al., 2011; Yuan and Madsen, 2014; O'Donoghue et al., 2021). The corresponding wave friction factors against the relative roughness heights are presented in Fig. 3.18, including the results of previous studies. The wave friction factors in the present experiments are distributed in the range from 0.05 to 1.0. The overall distribution shows that the wave friction factor tends to increase as A/k_s decreases. Furthermore, the scatters of wave friction factors align well with Dixen et al. (2008), with an RMSE of 0.127, compared to the formulas of Swart (1974) and Humbyrd (2012) with RMSEs of 0.225 and 0.176, respectively.

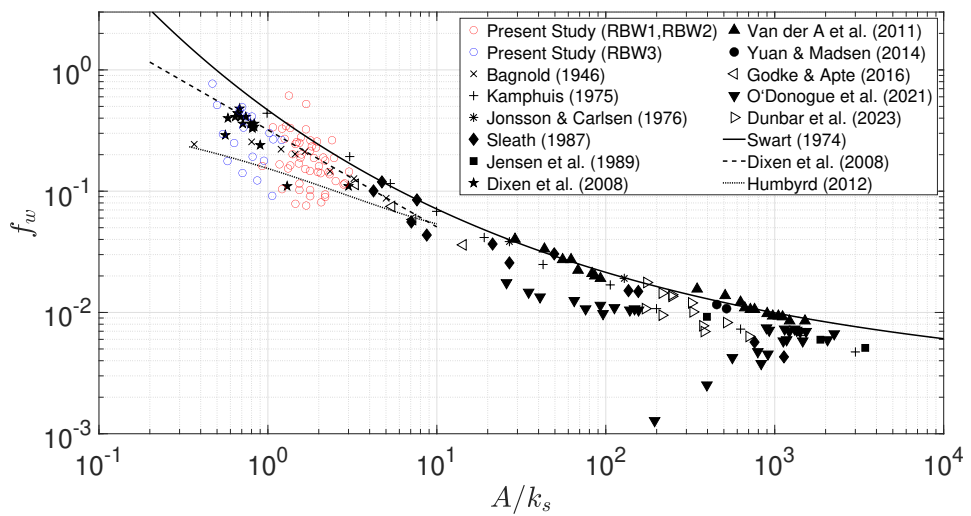


Figure 3.18: Wave friction factor (f_w) as a function of relative roughness height (A/k_s) with the previous study results and empirical relations (The wave friction factor of previous results are referenced including those from Van Der A et al. (2011), Yuan and Madsen (2014), and O'Donoghue et al. (2021))

Roughness height can influence the boundary layer thickness and the empirical relations proposed by Dixen et al. (2008) (Eq. 3.19) and Van Der A et al. (2011) (Eq. 3.20).

$$\frac{\delta_w}{k_s} = 0.08 [(A/k_s)^{0.82} + 1], \quad (3.19)$$

$$\frac{\delta_w}{k_s} = 0.75 (A/k_s)^{0.82}, \quad (3.20)$$

where δ_w is the boundary layer thickness. In oscillatory flow, the boundary layer thickness can be defined as the distance from the bottom to the point of maximum velocity (overshooting point) (Dixen et al., 2008; Van Der A et al., 2011; Yuan and Madsen, 2014; O'Donoghue et al., 2021). This definition is employed to investigate the relationship between the boundary layer thickness and roughness height. The boundary layer thickness is used at the phase of maximal bed shear stress. The resulting boundary layer thickness is marked in Fig. 3.19, along with findings from previous studies. Most previous experiments were conducted with A/k_s exceeding 30, while Dixen et al. (2008) conducted experiments where A/k_s was less than 1. In the present experiments, the range of δ_w/k_s according to A/k_s ranges from 0.03 to 0.3. As A/k_s decreases, δ_w/k_s generally decreases, consistent with the relationship observed in previous studies. Although the relative roughness heights for RBW3 are similar to those in Dixen et al. (2008), the corresponding δ_w/k_s is smaller than the results in Dixen et al. (2008). The experimental results are consistent with the characteristics of oscillatory flow across different rough structures and scales, suggesting that the roughness height calculated from Eq. 3.18 accurately represents the oscillatory flow characteristics.

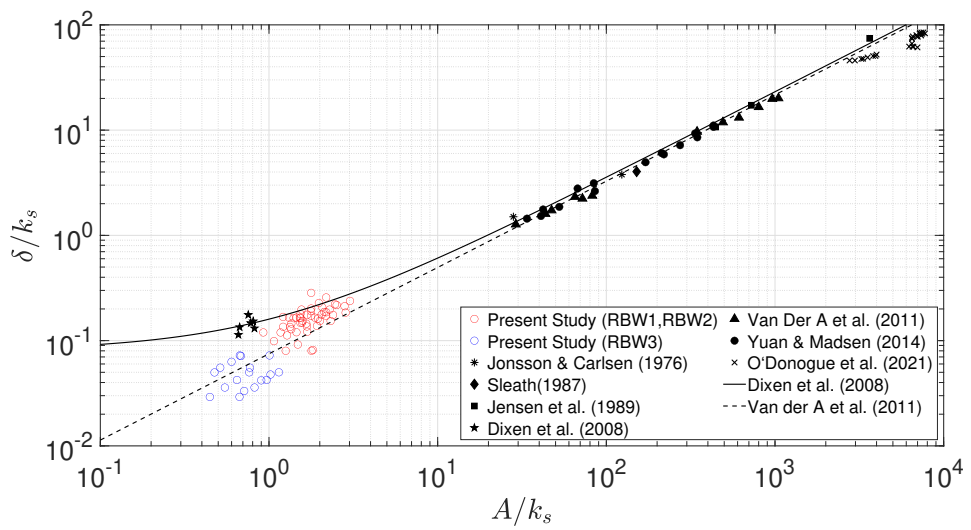


Figure 3.19: Boundary layer thickness as a function of relative roughness height (A/k_s) with the previous study results and empirical relations (The boundary layer thickness' of previous results are referenced including those from Van Der A et al. (2011), Yuan and Madsen (2014), and O'Donoghue et al. (2021))

The scale of rough elements over oyster reef surfaces is similar to that of gravel and cobble (ref. Chapter 3.2.1), and the proportionality coefficient in Eq. 3.18 is similar to those of gravel and cobble. The values of the proportionality coefficient in the roughness predictor for gravel have been reported to range from 3.1 to 8.2 (López and Barragán, 2008). The roughness predictors for gravel were obtained under bed conditions with a sediment sorting index (d_{84}/d_{50}) mostly ranging between 1.6 and 2.8 (Millar, 1999; López and Barragán, 2008). By applying the sorting index (d_{84}/d_{50}) to the oyster reef surfaces, it is determined that the range is 1.5 to 1.9, indicating that the roughness condition is similar to that of gravel beds. The similar characteristics of oyster reef surfaces and gravel bed conditions suggest that the roughness height equation derived in this study is likely comparable to that for gravel. In addition, Eq. 3.18 aligns with the observations in Styles (2015). Styles (2015) measured the velocity laterally away from the oyster banks and observed that the roughness height at the oyster banks was $5(\pm 2)$ times the average height of living oysters.

3.4.4 Application to actual topography

Hitzegrad et al. (2022) classified the oyster reef surfaces into five categories: central reef, transitional zone, cluster, patch, and garland, based on statistical analysis of 21 oyster reef surface data sets. Using these data sets, the roughness heights are estimated using the unified roughness predictor (Eq. 3.18). The calculated roughness heights mostly range on the order of 10^{-1} m (Table 3.5). The mean roughness height varies between 270 and 350 mm, depending on the structural classifications. Although direct comparison is not feasible due to the absence of roughness height estimation for these oyster reef surfaces, the calculated values are similar to the roughness height over oyster reefs presented in previous studies, such as $k_{s,o} = 90 - 630$ mm (Whitman and Reidenbach, 2012) and $k_{s,o} = 141$ and 324

mm (Styles, 2015). Therefore, it can be inferred that the unified roughness predictor reliably estimates the roughness height of oyster reefs. Additionally, the distribution of roughness heights can be obtained for different surfaces through the analysis of oyster reef surfaces (Fig. 3.20). These distributions can be utilized to determine the representative value of roughness height for the heterogeneous surface of oyster reefs, serving as a parameter for hydraulic analysis.

Table 3.5: Statistics of the height of rough element and roughness height depending on the five oyster reef surface classifications (Std: standard deviation; 50th: 50 percentile; 90th: 90 percentile)

	Mean (Std) height of rough element (Δ_o , mm)	Roughness height ($k_{s,o}$, mm; Eq. 20)		
		Mean (Std)	50 th	90 th
Central reef	46 (22)	325 (151)	319	534
Transitional zone	47 (22)	328 (155)	317	540
Cluster	39 (25)	272 (172)	231	523
Patch	50 (25)	351 (175)	339	598
Garland	42 (25)	297 (174)	265	555

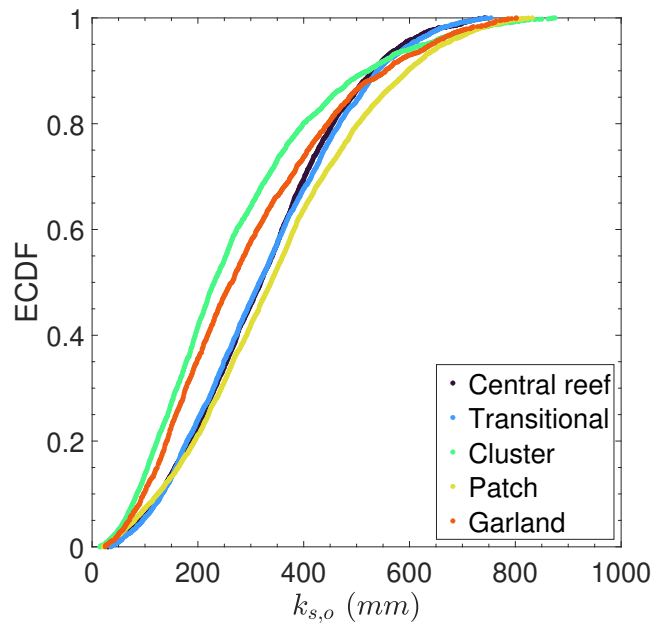


Figure 3.20: Distribution of the roughness height over oyster reef surfaces depending on the five structural classifications

3.5 Concluding remarks

In the study described in Chapter 3, a roughness predictor applicable to both the unidirectional and oscillatory flows is proposed along with a method for measuring the size of rough elements on oyster reef surfaces in order to estimate the roughness height for oyster reefs. This study focuses on calculating the roughness height for individual rough elements on the oyster reef surfaces.

Firstly, experiments were conducted using rough bottom models that mimicked oyster reef surfaces to investigate the relationship between geometric variables and roughness height. The results confirm that the roughness height can be formulated by the height of rough elements on the oyster reefs under both unidirectional and oscillatory flow conditions. Additionally, a unified roughness predictor is suggested for estimating roughness height in both unidirectional and oscillatory flow conditions. This roughness predictor is validated by comparing the fitted logarithmic velocity profiles, using the calculated roughness heights, with the PIV-measured velocities. The applicability of the roughness predictor to different scales is also verified using models of varying scales.

The height of rough elements on oyster reefs, an essential variable for estimating roughness height, can be measured through surface analysis employing the EMD and zero-upcrossing techniques. The oyster reefs, comprising clusters of individual oysters, exhibit a wide range of roughness height values. The distribution characteristics of the roughness height vary depending on the surface classification of the oyster reefs. Thus, it is feasible to determine a representative roughness height suitable for the surface characteristics of oyster reefs from the distribution.

The roughness height is a crucial parameter for understanding the effects of oyster reefs on wave attenuation, current reduction, and sediment transport. Due to these benefits, oyster

reefs are gaining attention as the nature-based solution (NbS), leading to numerous field studies and numerical studies focused on NbS design. From this perspective, the results of this study are expected to be useful for constructing numerical models and analyzing the field-measured data. This is because accurately estimating roughness height is essential for precisely understanding the hydraulic impact of oyster reefs.

Chapter 4. ESTIMATION OF FRICTION FACTOR AND BED SHEAR STRESS CONSIDERING BEDFORM EFFECT

4.1 Introduction

Roughness in the rivers arises from a variety of features such as sediment, bedforms, vegetation, and man-made structures. The roughness interacts with the fluid flow and the interaction induces turbulence and affects the flow velocity, bed shear stress, sediment transport, and morphology. The effects of roughness elements on hydrodynamics were conducted for several decades (Best, 2005). Flow structures over the bedform were investigated through experiments and field campaigns (Best and Kostaschuk, 2002; Venditti and Bauer, 2005; Holmes Jr and Garcia, 2008; Sukhodolov et al., 2006; Lefebvre et al., 2013; MacVicar and Obach, 2015). Key influences of bedforms on flow structure include flow acceleration, flow separation, and secondary flow cells (Best, 2005). Total bed shear stress is expressed as the sum of grain bed shear stress and form bed shear stress and the contribution of form bed shear stress could be larger than the grain bed shear stress (Chanson, 2004).

For river surveys, acoustic Doppler current profiler (ADCP) is widely used, which offers an opportunity to collect spatially extensive data collection. It can be utilized for time-series measurements through installation on the river bed or structures, as well as for spatial measurements when equipped on a moving boat (Muste et al., 2004; Vermeulen et al., 2013). Additionally, ADCP has become versatile, allowing for riverbed topography surveys through water depth measurements (Williams et al., 2015; Kasvi et al., 2017), estimation

^oThis chapter is reproduced from the part of following publication: Lee, Park, Lee, Song, & Park (2024). Earth Surface Processes and Landforms. DOI: <http://doi.org/10.1002/esp.5954>.

of suspended sediment concentration and bedload (Gaeuman and Jacobson, 2006; Baranya and Józsa, 2013; Guerrero et al., 2014; Conevski et al., 2023), and calculation of bed shear stress based on measured velocity (Fugate and Chant, 2005; Sime et al., 2007; Stone and Hotchkiss, 2007; Engel and Rhoads, 2016). Therefore, it is possible to analyze the shape of the bedform, estimate the roughness height, and calculate the bed shear stress by incorporating form roughness height using ADCP.

However, since the primary development of bedform occurs in the flow direction in rivers, the shape and dimensions of bedform are defined from the bed profile in the streamwise direction (Gutierrez et al., 2013). On the other hand, ADCP surveys for analyzing hydraulic characteristics of rivers are generally conducted in the transverse direction (Dinehart and Burau, 2005; Vermeulen et al., 2014; Engel and Rhoads, 2016; Herrero et al., 2018; Palman and Trento, 2023). Hence, there are limitations in bedform analysis and roughness height estimation using ADCP measurements. However, obtaining river cross-sectional information can be valuable for understanding spatial variations in various hydrodynamic phenomena, including changes in flow velocity based on channel planform and variation of water depth. Therefore, it is necessary to calculate roughness heights and friction factors, through the integration of these data.

In Chapter 4, a method to estimate friction factor and bed shear stress considering form roughness height using ADCP-measured data in the transverse direction is proposed. Additionally, the friction coefficient distribution considering form roughness is determined for selecting the representative friction coefficient. However, when using transverse data, the limitation is that the length of bedforms cannot be estimated. Therefore, an analysis of streamwise data is conducted to derive the relationship between the height and length of bedforms, which is then utilized in calculating the form roughness height. The proposed

method is applied to the Nakdong River in South Korea to assess its suitability.

4.2 Field survey

4.2.1 Study site

Field surveys were conducted to collect bathymetry data and flow velocity in the Nakdong River (ND-River), one of the major rivers in South Korea. ND-River is located in the southeastern part of South Korea with a length being 510.36 km and eight multifunctional weirs are placed along the reach. The locations of these eight weirs are indicated in Fig. 4.1. This study specifically focuses on bathymetry data and velocity measurements in the segments between Chilgok weir (N 36°0'56'', E 128°23'53'') and Changnyeong-Haman weir (N 35°22'48'', E 128°33'7''), covering five of the eight weirs (Fig. 4.1(a)). The channel width in the surveyed segments ranges from 220 to 1,220 m (ND-S1: 285-1,160 m; ND-S2: 300-1,220 m; ND-S3: 220-465 m; ND-S4: 280-835 m), with an average channel width of 448 m (MOE, 2022a).

The discharges and water levels in the mainstream are regulated by the operation of these weirs. Outside the flooding season (June to September), the water levels are controlled according to the designated water level. Detailed information about the average water levels, average discharges, and extreme discharges for each segment is provided in Table 4.1. The discharges and water level information in Table 4.1 are based on data collected over 11 years from 2013 to 2023. This period was chosen because the weirs in ND-River were installed and began operation in 2012, therefore, data from after 2013 were used. The data of discharge and water level for ND-River can be obtained from website (www.water.or.kr). During the flood season, while variations exist among segments, the discharge increases, reaching a maximum of 5,000-10,000 m^3/s . Simultaneously, with the rise in discharge, the water levels

increase by more than several meters compared to the average water level.

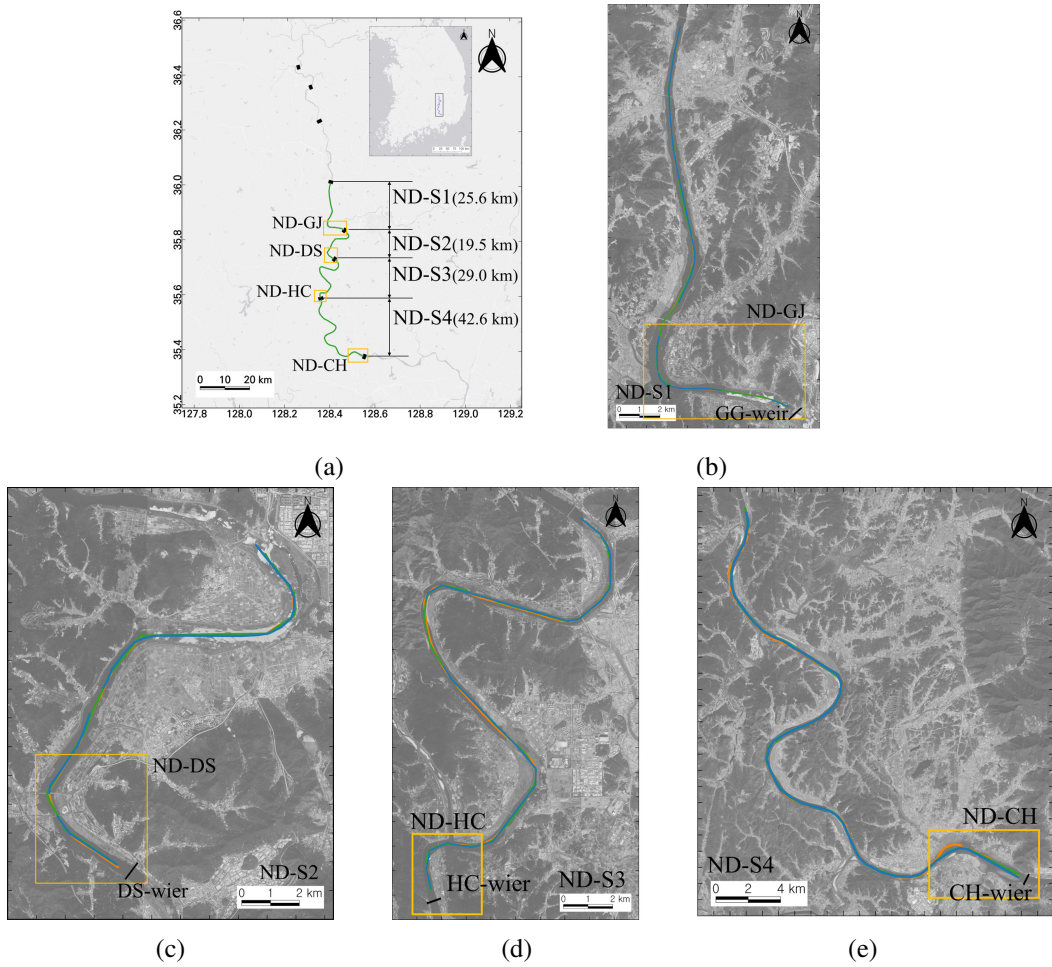


Figure 4.1: The map of study site (a) Overview of field survey area (b)-(e) Thalweg bed profile survey lines for the four segments (ND-S1, ND-S2, ND-S3, and ND-S4) and velocity measured area (ND-GJ, ND-DS, ND-HC, and ND-CH) with indicated orange box

Table 4.1: Average discharge, average water level, and representative percentile of discharge for four segments (ND-S1, ND-S2, ND-S3, and ND-S4)

	ND-S1	ND-S2	ND-S3	ND-S4
Q_{avg} (m^3/s)	151.6	178.4	200.4	299.0
Q_{50th} (m^3/s)	70.5	89.0	98.5	154.5
Q_{90th} (m^3/s)	285.0	313.1	372.4	569.7
Q_{95th} (m^3/s)	483.4	511.4	628.4	901.6
Q_{99th} (m^3/s)	1829.3	1928.8	2291.5	2814.8
Average water level (EL.m)	18.8	13.8	9.5	4.6

The representative sediment size (d_{50}) in the study sites was obtained through field surveys conducted in 2019 (for ND-S1) and 2022 (for ND-S2, ND-S3, and ND-S4). The ranges of the median diameter in the target segments are summarized in Table 4.2. The median particle size in the four segments ranges between 0.029 mm and 4.221 mm. While there are instances where silt particles seem to dominate in ND-S4, overall, it is evident that the average particle size is greater than 0.065 mm. According to the particle classification criteria (Julien, 2010), particles with a size of 0.065 mm or larger are classified as sand particles. In ND-S1, the sand content exceeds 80%, and in the other segments (ND-S2, ND-S3, and ND-S4), it exceeds 90%, indicating a significant proportion of sand in the bed material. The overall uniformity coefficient (C_{μ}) is below 4, suggesting poorly graded sands according to the Unified Soil Classification System (USCS; ASTM Standard D2487-11 (2011)). Therefore, it can be considered that the reach of ND-River is predominantly composed of sand.

Table 4.2: Characteristics of sediment particles for the four segments (ND-S1, ND-S2, ND-S3, and ND-S4) in the Nakdong River

	ND-S1	ND-S2	ND-S3	ND-S4
d_{50} (mm)	0.56 (0.15-4.2)	0.30 (0.06-1.5)	0.52 (0.29-0.75)	0.27 (0.03-0.52)
C_{μ}	4.0	2.0	2.0	2.0
Percentage of Sand (%)	82	94	93	97

4.2.2 Bathymetry measurement

Bed profiles along the center of the river channel for the four segments were collected using a single-beam echo sounder (Hydrotrac HT97001). Bed elevation surveys for each segment were conducted four times in June and October of 2022 and 2023. The subdivided segments are as follows: (1) Chilgok weir-Gangjeong-Goryeong weir (ND-S1) (2) Gangjeong-Goryeong weir – Dalseong weir (ND-S2) (3) Dalseong weir – Hapcheon-Changnyeong weir (ND-S3) (4) Hapcheon-Changnyeong weir – Changnyeong-Haman weir (ND-S4) (Fig. 4.1), with the measured bed profiles shown in Fig. 4.2. The total length of the surveyed reach is 116 km from the Chilgok weir to the Changnyeong-Haman weir. The average bed slopes in four segments range from 0.002 to 0.004, exhibiting a gentle bed slope. However, some sections such as those between 10 and 25 km of ND-S3 and between 20 and 40 km of ND-S4, exhibit bed elevation differences of over 10 m within the segments. These areas have steep bed slopes of up to 0.038.

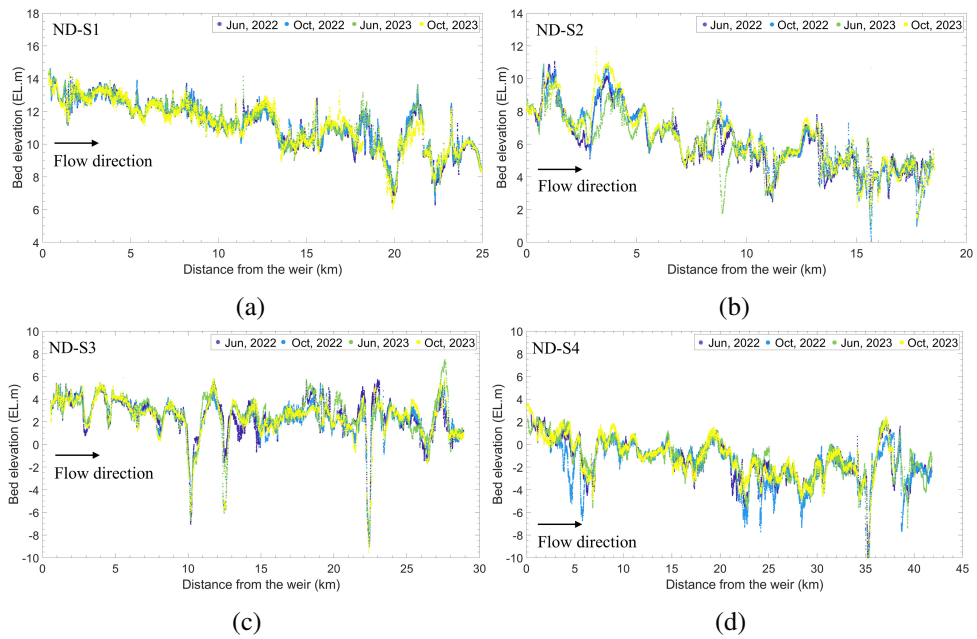


Figure 4.2: The bed elevation along the center of channel, measured through four field surveys (a) ND-S1 (b) ND-S2 (c) ND-S3 (d) ND-S4

4.2.3 Flow velocity measurement

Flow velocity measurements were conducted upstream of the four weirs: (1) Gangjeong-Goryeong weir (ND-GJ) (2) Dalseong weir (ND-DS) (3) Hapcheon-Changnyeong weir (ND-HC) (4) Changnyeong-Haman weir (ND-CH) (Fig. 4.1). The flow velocity was measured using an acoustic Doppler current profiler (ADCP, SonTek Riversurveyor M9), which was equipped on a moving boat. ADCP and a differential global positioning system were synchronized, recording coordinates along with velocity measurements at the measurement points. Riversurveyor M9 features a smart pulse function that automatically adjusts the frequency of beams depending on the water depth, with the number of bins in the vertical direction changing accordingly. During post-processing of ADCP data, the cross-sectional grid system at each measured section was reconstructed, and then the velocity fields were analyzed (Rhoads and Kenworthy, 1998; Kim and Muste, 2012; Parsons et al., 2013; Vermeulen et al., 2014). The flow velocity was initially obtained in the Cartesian coordinate system (east and north), then the velocity components were transformed to the orthogonal curvilinear (s, n) system, yielding streamwise and normal velocity components.

The flow velocity was measured at the specified regions around 15 cross-sections with intervals of 200 m to 500 m. Flow velocity measurements were conducted once in ND-GJ, and twice in other regions, ND-DS, ND-HC, and ND-CH. Table 4.3 presents the hydraulic conditions on the field survey dates. A total of 7 field surveys were carried out under relatively high flow conditions, with the water levels maintained at average levels. ND-GJ1, ND-HC1, and ND-CH1 field surveys were carried out under flow conditions with a discharge greater than the 95th percentile. The remaining field surveys were also conducted under relatively high flow conditions, exceeding the 90th percentile of discharge, except ND-CH2.

Table 4.3: Hydraulic conditions at the field survey dates for measuring flow velocity (Q : discharge; \bar{U} : cross-sectional average velocity; \bar{h} : mean water depth; Fr : Froude number ($Fr = \bar{U}/\sqrt{g\bar{h}}$); g : gravitational acceleration (9.81 m/s^2))

	Survey Date	$Q \text{ (m}^3/\text{s)}$	Water Level (EL. m)	$\bar{U} \text{ (m/s)}$	$\bar{h} \text{ (m)}$	Fr
ND-GJ1	Sep 27, 2023	975.7	18.26	0.23	7.37	0.03
ND-DS1	Jun 29, 2023	375.9	14.0	0.18	8.54	0.02
ND-DS2	Sep 25, 2023	405.2	13.57	0.18	8.42	0.02
ND-HC1	Jun 28, 2023	1010.4	9.21	0.48	7.73	0.07
ND-HC2	Sep 5, 2023	330.5	9.23	0.19	7.55	0.02
ND-CH1	Jun 29, 2023	1161.9	4.89	0.43	5.54	0.06
ND-CH2	Sep 6, 2023	425.7	4.89	0.18	5.76	0.02

4.3 Methodology

4.3.1 Analysis of bedform

Bedforms are distinguishable in the measured bed profile. In rivers, the bedforms can develop with a minimum height of a few centimeters and lengths ranging from a few meters to several hundred meters (Bradley and Venditti, 2017). Therefore, the bedform size is substantial enough to derive meaningful results from morphology surveys. A well-established method for tracking bedforms from the bed profile was developed by Van der Mark and Blom (2007); Van der Mark et al. (2008) and studies were conducted to investigate the distribution and characteristics of bedforms developed in rivers (Gutierrez et al., 2014; De Lange et al., 2021; Zomer et al., 2022; Muste et al., 2023).

Bedform analysis, including identification and extraction of geometric parameters, is conducted using the method adapted from Van der Mark et al. (2008), utilizing riverbed data measured in the streamwise direction within ND-S1 to ND-S4 regions. Van der Mark et al. (2008) used filtered bathymetry data and the zero-crossing method to identify bedforms and estimate their size. Based on the identified bedform information, the height and length of bedforms are estimated, and the relationship between height and length is examined. The measured bed profile shows variations in elevation, forming crest and trough due to the development of bedforms. Therefore, by applying the zero-crossing method to identify crests and troughs, individual bedform element can be defined. For the application of the zero-crossing method, it is necessary to set a reference level. The reference level was determined using smoothed bed level data (Van der Mark et al., 2008; De Lange et al., 2021; Zomer et al., 2021). The LOESS (locally estimated scatterplot smoothing) algorithm is used for smoothing the bed profile. LOESS is a non-parametric regression technique used for

smoothing irregular morphology data (Van Dijk et al., 2008; Cazenave et al., 2013; Zomer et al., 2021), and it effectively captures local variations without losing information about bedforms (Zomer et al., 2022). The variation of bedform level is obtained by subtracting the smoothed bed profile from the original bed level. Subsequently, the zero-crossing method is applied to determine crest and trough points and the individual bedform is identified. The variation between trough points on either side of the crest point is defined as one bedform (Fig. 4.3). Subsequently, bedform height and length are estimated from this information. The height of bedform (Δ_f) is defined as the distance from crest to trough and the length (Λ_f) is defined as the distance between two adjacent trough points. The definitions of bedform height and length are illustrated in Fig. 4.3.

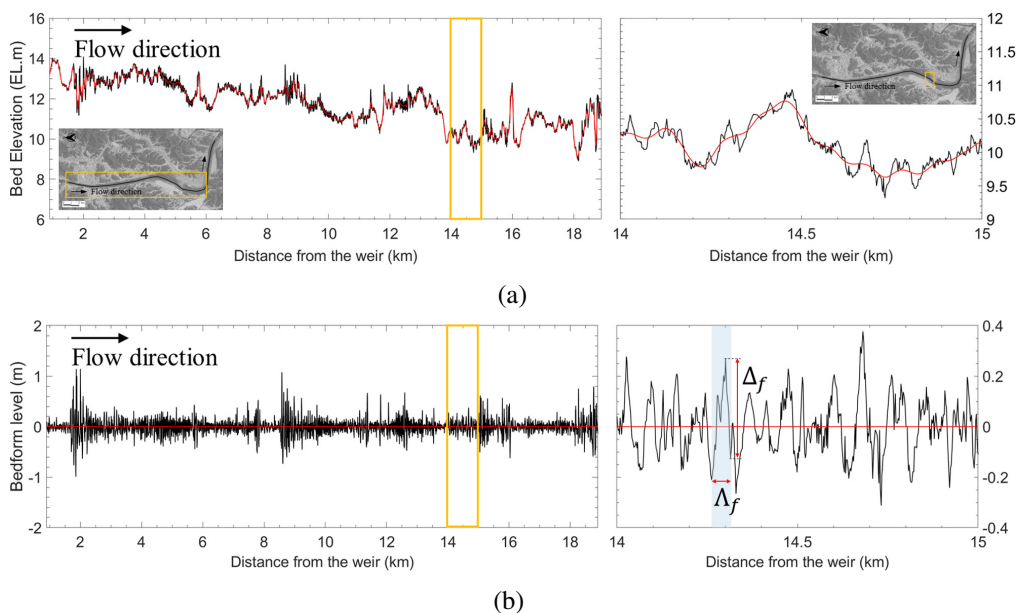


Figure 4.3: Decomposition of bedform level and definition of bedform information, height and length (a) Sample of measured bed profile (black solid line) and its smoothed bed profile (red solid line) (b) Bedform level and definition of bedform height and length

The average bedform size and corresponding form roughness height developed in each segment are presented in Table 4.4. The bedform characteristics presented in Table 4.4 are calculated from a total of 18,713 bedforms identified from the bed profiles between ND-S1 and ND-S4. The form roughness height ($k_{s,f}$) was calculated using the form predictor proposed by Van Rijn (1993) (Eq. 4.11). The calculated form roughness height exhibits an order of centimeters, indicating that it is more than 10 times larger compared to the roughness height of sand particles, which has an order of millimeters or less. The grain roughness height is generally estimated from the representative grain diameter with a form $k_{s,g} = \alpha d_*$, and the range of α is between 1 and 6.6 (Yen, 2002). This implies that form bed shear stress may contribute significantly to total bed shear stress.

Table 4.4: Average size of bedform and form roughness height

	Bedform height (Δ_f, m)	Bedform length (Λ_f, m)	Form roughness height ($k_{s,f}, mm$)
Overall	0.130 (0.069)	10.7 (5.25)	46 (41)
ND-S1	0.115 (0.066)	10.8 (4.81)	38 (36)
ND-S2	0.111 (0.052)	10.0 (5.37)	36 (28)
ND-S3	0.121 (0.062)	9.74 (4.95)	45 (42)
ND-S4	0.150 (0.073)	11.6 (5.53)	56 (44)

The aim of establishing the relationship for bedform length is to estimate bedform length based on river cross-sectional bed profile data in the transverse direction and calculate the form roughness height. In order to comprehend the hydraulic characteristics in rivers, ADCP is utilized to measure cross-sectional flow velocity, allowing simultaneous acquisition of water depth. Furthermore, the distribution of bed shear stress along the cross-section may vary depending on the changes in velocity and roughness height in the transverse direction. Therefore, to estimate the cross-sectional distribution of bed shear stress, it is necessary to

estimate form roughness height along the cross-section. While roughness elements can be separated based on the acquired bed profile in the transverse direction, there is a limitation in defining the bedform length (Lee et al., 2024b). Therefore, the empirical formula is required to estimate bedform length, and Eq. 4.2 is used as it represents the characteristics of bedforms in the target area in this study.

Previous studies suggested that the relationship between bedform height and bedform can be expressed with a power-law form as follows (Flemming, 2000; Lefebvre et al., 2016; Bradley and Venditti, 2017):

$$\Delta_f = a\Lambda_f^b, \quad (4.1)$$

where a and b are determined as 0.0677 and 0.8098 by Flemming (2000), 0.13 and 0.59 by Lefebvre et al. (2016), and 0.0513 and 0.7744 by Bradley and Venditti (2017).

Through the obtained bedform information, the relationship between the normalized height and length of bedform is derived (Eq. 4.2; Fig. 4.4). The height and length of bedform are normalized by d_{50} . It is observed that the scale of bedforms developed in the four segments (ND-S1, ND-S2, ND-S3, and ND-S4) is similar, and the height and length of bedform exhibit a similar relationship across the four segments. The derived empirical equation (Eq. 4.2) is obtained by aggregating the data from the four segments, and it is utilized to estimate bedform length from the bedform height. The bedform lengths developed between ND-S1 and ND-S4 range from 3 to 25 m, with a tendency to increase as bedform height increases. Eq. 4.2 expresses this trend. However, various bedform lengths can develop at the same bedform height, causing the actual data to be more scattered than predicted by Eq. 4.2. Eq. 4.2 represents the average relationship between normalized bedform height and length. Out of a

total of 18,713,92% are distributed between $1.6 \times 10^3 (\Delta_f / d_{50})^{1/3}$ and $8.2 \times 10^3 (\Delta_f / d_{50})^{1/3}$ (the purple and blue dashed line in Fig. 4.4(a)). The accuracy of estimating the roughness height by applying Eq. 4.2 is discussed in the result part of Chapter 4.

$$\Lambda_f / d_{50} = 4.1 \times 10^3 (\Delta_f / d_{50})^{1/3}. \quad (4.2)$$

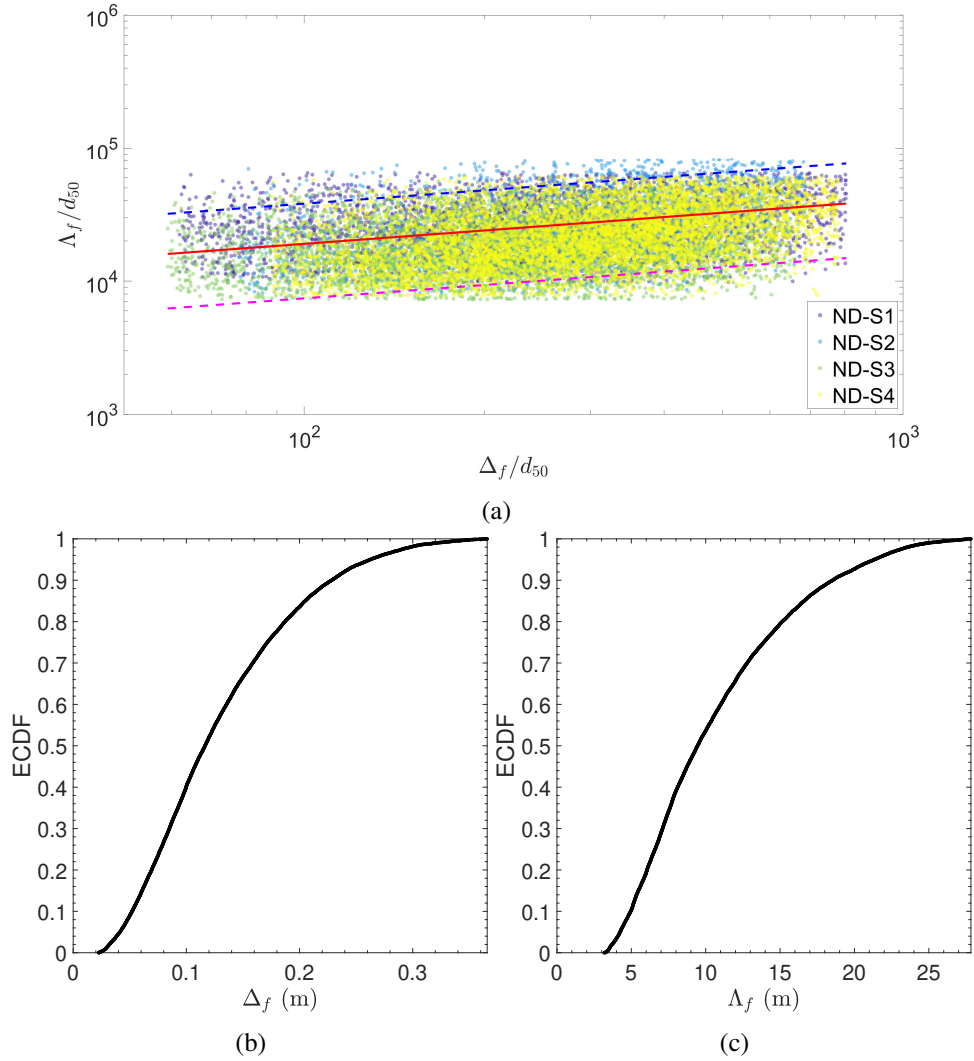


Figure 4.4: (a) Correlation plot of bedform height and length, where the red solid line is for $\Lambda_f/d_{50} = 4.1 \times 10^3 (\Delta_f/d_{50})^{1/3}$; the blue dashed line is for $\Lambda_f/d_{50} = 8.2 \times 10^3 (\Delta_f/d_{50})^{1/3}$; the purple dashed line is for $\Lambda_f/d_{50} = 1.6 \times 10^3 (\Delta_f/d_{50})^{1/3}$; (b) Distribution of bedform height (c) Distribution of bedform length

The method to estimate form roughness height from cross-sectional data in the transverse direction is outlined below. Firstly, the roughness elements are distinguished from the bed profiles to estimate bedform size. For this analysis, a similar method used for bedform analysis from the bed profile in the streamwise direction is applied. The bedform level is obtained by subtracting the smoothed bed profile from the original bed profile, and the crest and trough points are identified using the zero-crossing method. During this process, the smoothed bed profile is fitted using LOESS algorithm. An individual bedform is defined as the level change interval between the trough points on either side of the crest point. Examples of identified bedforms are illustrated in Fig. 4.5. The bedform height is defined as the greater of the distances between the crest and the two trough points in the identified bedform interval. As mentioned earlier, estimating the length from cross-sectional data has limitations since the primary direction of bedform development in rivers is along the flow direction. Thus, the obtained empirical relation (Eq. 4.2) is utilized to calculate the bedform length, and finally, the form roughness height can be calculated using Eq. 4.11.

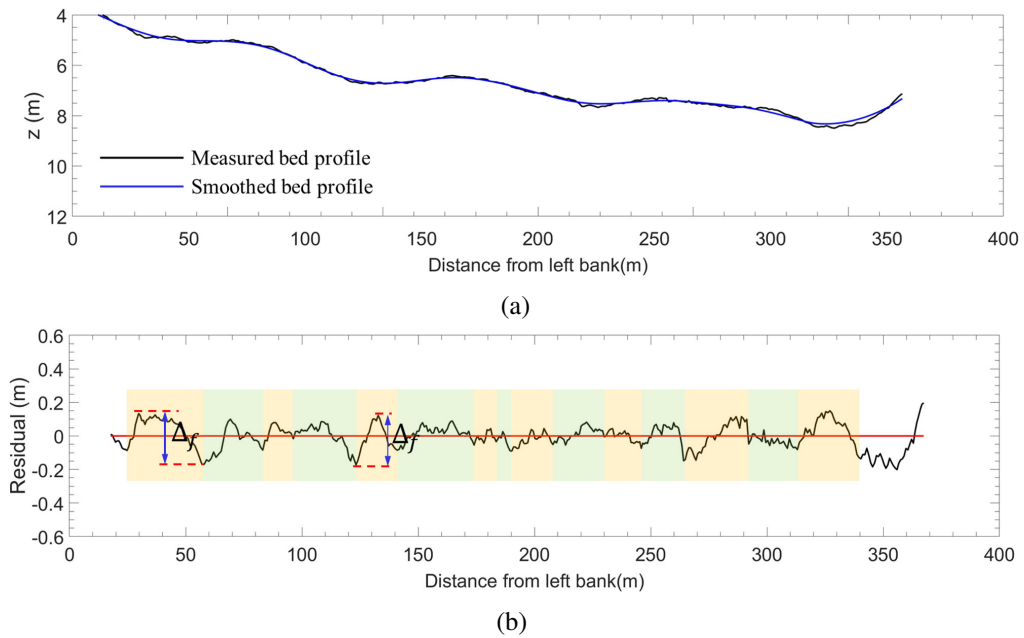


Figure 4.5: Identification of roughness elements in bed profile in the transverse direction (a) Sample of measured bed profile and its smoothed bed profile (b) Identification of rough elements from the decomposed bed level and definition of bedform height

4.3.2 Bed shear stress

The bed shear stress can be calculated using several methods: (1) the log-law (Sime et al., 2007) (2) the quadratic friction law (Engel and Rhoads, 2016) (3) Reynolds stress (Lichtneger et al., 2020) (4) turbulent kinetic energy (Kim et al., 2000) (5) energy spectrum (Johnson and Cowen, 2017). In this study, the log-law and quadratic friction law are used to compute the bed shear stress with ADCP data (Biron et al., 2004; Sime et al., 2007; Engel and Rhoads, 2016; Kim and Hwang, 2023). The shear velocity is obtained by the log-law (Eq. 4.3), then the bed shear stress can be estimated using Eq. 4.4.

$$\frac{u}{u_*} = \frac{1}{\kappa} \ln \left(\frac{z}{z_0} \right) + C_1, \quad (4.3)$$

$$\tau_b = \rho u_*^2, \quad (4.4)$$

where ρ is water density; u_* is shear velocity; κ is von Kármán constant (≈ 0.41); z_0 is hydraulic roughness height ($z_0 = k_s/30$); C_1 is constant ($C_1 = 5.1$). When fitting the logarithmic velocity profile, two unknown variables, u_* and k_s should be determined. In the study described in Chapter 4, k_s is pre-assigned from bedform analysis, and u_* is obtained by fitting the logarithmic velocity profile.

Another method to calculate bed shear stress using the depth-average velocity in the unidirectional flow can be expressed as follows,

$$\tau_b = \frac{1}{8} \rho f U^2 = \frac{\rho g U^2}{C^2} = \rho C_f U^2, \quad (4.5)$$

where f is Darcy-weisbach friction factor; U is depth-average velocity; g is gravitational acceleration; C is Chezy coefficient; C_f is dimensionless Chezy coefficient.

Chezy coefficient can be formulated in terms of roughness height and water depth (Eq. 4.6) and it can be derived from log-law (Van Rijn, 1993).

$$C = \frac{2\sqrt{g}}{\kappa} \log \left(\frac{12h}{k_s} \right), \quad (4.6)$$

where h is water depth. The dimensionless Chezy coefficient, C_f , is expressed as power form with roughness height (Eq. 4.7).

$$C_f = \left(8.1 \left(\frac{h}{k_s} \right)^{1/6} \right)^{-2}. \quad (4.7)$$

The roughness height is classified into the grain and form-related roughness height, $k_{s,g}$ and $k_{s,f}$ based on the concept of classification of bed shear stress and friction factor as follows,

$$\tau_b = \tau_{b,g} + \tau_{b,f}, \quad (4.8)$$

$$f = f_g + f_f, \quad (4.9)$$

where $\tau_{b,g}$ is grain-related bed shear stress; $\tau_{b,f}$ is form-related bed shear stress; f_g is grain-related friction factor; f_f is form-related friction factor. The grain roughness height is generally computed from grain diameter and the form roughness height is computed from the geometric variables of bedform. Eq. 4.11 is applicable to dune-type bedform, except the anti-dunes (Van Rijn, 1984). The steepness (Δ_f / Λ_f) of dune is less than 0.7, and the bedforms identified from the thalweg bed profiles of ND-River can be considered dune-type

bedform, as their steepness is predominately less than 0.7.

$$k_{s,g} = \alpha d_{50}, \quad (4.10)$$

$$k_{s,f} = 1.1\Delta_f \gamma (1 - \exp(-25\Delta_f/\Lambda_f)), \quad (4.11)$$

In the study described in Chapter 4, α is set as 1; d_{50} is 50th percentile of grain size distribution; γ is field condition parameter, ($\gamma=0.7$).

Total Chezy coefficient considering both the grain and bedform effects can be computed by Eq. 4.13 according to the relationship between Chezy coefficient and friction factor.

$$C = \sqrt{\frac{f}{8g}}, \quad (4.12)$$

$$\frac{1}{C^2} = \frac{1}{C_g^2} + \frac{1}{C_f^2}. \quad (4.13)$$

Manning's n which is widely used friction coefficient in open channel flow can be estimated from Chezy coefficient as follows,

$$n = \frac{h^{1/6}}{C}. \quad (4.14)$$

4.4 Results

4.4.1 Friction factor in the Nakdong River

The roughness height and Chezy coefficient for the transverse velocity measurement transects are calculated based on the method described in Section 4.2. To ensure the suitability of estimated form roughness height, the form roughness height estimated from cross-sectional data in the transverse direction is compared to the form roughness height estimate

based on the thalweg transect obtained on the same day of velocity measurements. In the case of the field surveys for ND-GJ1 and ND-DS2, where the bed profile in the streamwise direction was not acquired, the data are excluded for the comparison. The comparison is conducted for the remaining measurement cases, ND-DS1, ND-HC1, ND-HC2, ND-CH1, and ND-CH2. Fig. 4.6 depicts the correlation between the height of bedform and the corresponding form roughness height. The comparison results demonstrate that the estimated form roughness height from the cross-sectional data is similar to the form roughness height which is obtained from the thalweg transect data. This is because the heights of bedform identified in both streamwise and transverse bed profiles are similar, and Eq. 4.2 accurately represents the length of bedform developing in the Nakdong River. As a result, the form roughness heights analyzed in the streamwise and transverse directions are similar.

The high correlation between the two datasets shows that the estimated form roughness height from cross-sectional data can be rationally utilized as a form roughness height for the reach along the river. Furthermore, these results can provide supplementary information to understand the spatial distribution of the friction factor and bed shear stress. Conventionally, bedform identification has been conducted using bed profiles in the streamwise direction, and the identified bedform data are used to calculate roughness heights and friction factors. This approach had limitations in analyzing roughness height and friction factors that could develop across the river channel width. Thus, the presented method provides data that can overcome the limitations of the conventional method.

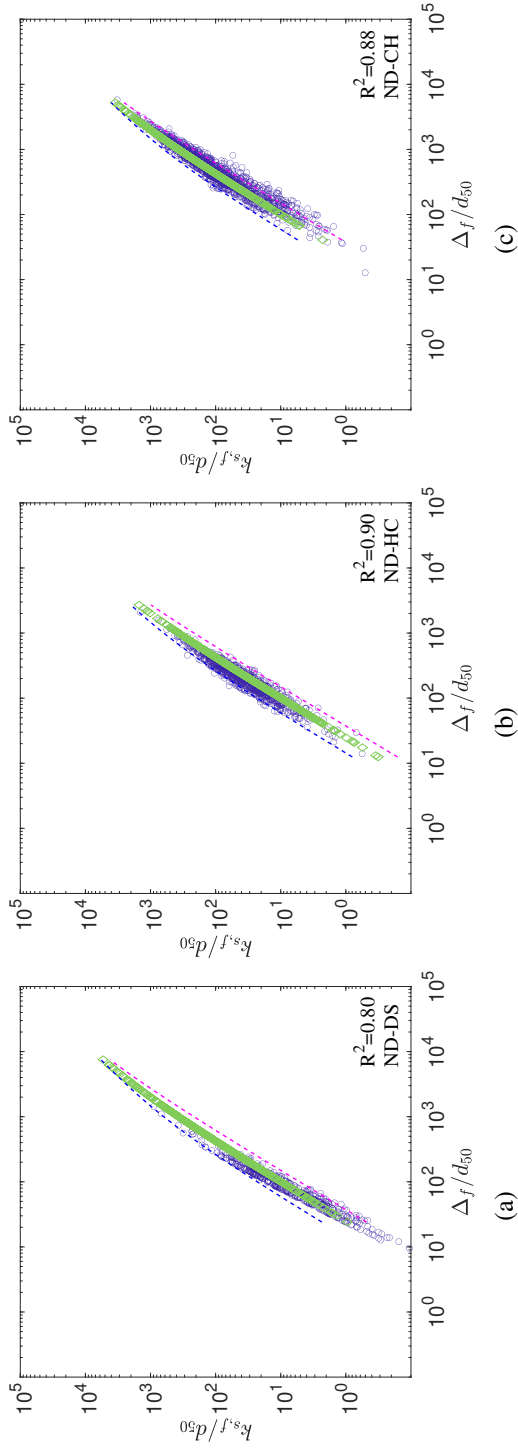


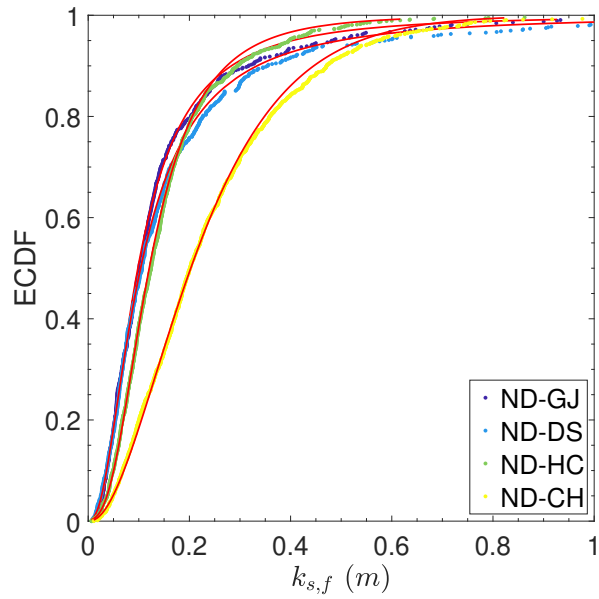
Figure 4.6: Comparison of bedform height and form roughness height estimated from streamwise and transverse bed profile data for velocity measured region (a) ND-DS (B) ND-HC (c) ND-CH (Blue circle: estimated values from streamwise bed profile data; Green diamond: estimated values from transverse bed profile data with Eq. 4.2); blue dashed line: estimated values from transverse bed profile data with $\Lambda_f/d_{50} = 8.2 \times 10^3 (\Delta_f/d_{50})^{1/3}$; purple dashed line: estimated values from transverse bed profile data with $\Lambda_f/d_{50} = 1.6 \times 10^3 (\Delta_f/d_{50})^{1/3}$)

The average values of form roughness height and friction coefficients (Chezy coefficient and Manning's n) estimated from the cross-sectional bed profile in the transverse direction are summarized in Table 4.5. The range of average roughness height values in the surveyed sections is 31.0-122.5 (mm). The estimated form roughness, on the order of centimeters, is more than ten times larger than the grain roughness height. This observation suggests that form roughness plays a significant role in estimating bed shear stress. Considering the estimated form roughness height, Chezy coefficient yielded an average value around $50 m^{1/2}/s$, with a range between 30 and $70 m^{1/2}/s$. In addition, Manning's n is estimated to have an average value of approximately $0.028 s/m^{1/3}$, with values ranging between 0.020 and 0.048. These values align with typical friction coefficients under ripples and sand dunes, namely $C : 32 - 72 m^{1/2}/s$ and $n : 0.018 - 0.040 s/m^{1/3}$ (Julien, 2018). If the influence of bedforms is not considered, and only sediment size is taken into account to calculate Chezy coefficients of the flow velocity measurement sections, the range is observed to be $68 - 98 m^{1/2}/s$. This range of Chezy coefficient is different from when considering bedforms, and this difference affects the calculation of bed shear stress. The contribution of bedform to bed shear stress is discussed in Section 4.5.1.

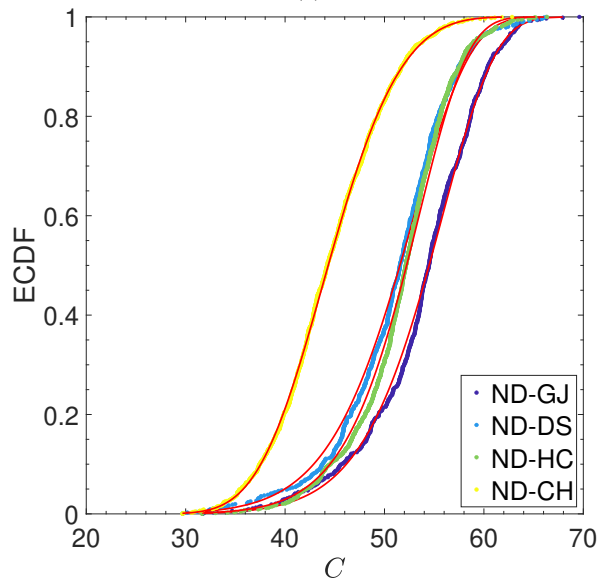
Table 4.5: Mean form roughness height (value in parentheses represents the standard deviation) and mean Chezy coefficient and Manning's n (ranges of Chezy coefficient and Manning's n values in parentheses)

	$k_{s,f}$ (mm)	C ($m^{1/2}/s$)	n ($s/m^{1/3}$)
ND-GJ1	40.0 (90.6)	54 (32-70)	0.027 (0.021-0.044)
ND-DS1	84.0 (165.2)	51 (30-66)	0.029 (0.021-0.048)
ND-DS2	55.0 (141.5)	51 (31-61)	0.029 (0.022-0.046)
ND-HC1	42.1 (52.0)	52 (36-66)	0.028 (0.020-0.040)
ND-HC2	31.0 (63.5)	52 (32-65)	0.027 (0.021-0.042)
ND-CH1	74.4 (99.0)	46 (30-62)	0.028 (0.021-0.043)
ND-CH2	122.5 (107.5)	43 (30-63)	0.031 (0.022-0.043)

Similar to the sediment, the bedforms do not uniformly develop in the same size across the space, resulting in variations in the friction coefficient depending on the regions. Therefore, it is necessary to understand the characteristics of the target region. In this aspect, the distributions of form roughness height and Chezy coefficient in each surveyed region are examined and the probability density function (PDF) for form roughness height and Chezy coefficient were fitted, respectively (Fig. 4.7). The parameters for the fitted PDF are presented in Table 4.6. The fitted PDF was selected by choosing the distribution with the smallest error compared to empirical cumulative distribution function (ECDF) among those that passed the statistical hypothesis tests such as Kolmogorov-Smirnov test and Chi-square test. PDF fitting results indicate that the fitted PDF is more suitable for extreme value distributions such as Generalized extreme value (GEV) and Weibull distributions than normal distribution. Furthermore, the fitting results show distinct development characteristics of the form roughness height and Chezy coefficient depending on the segments. It demonstrates the need to consider local characteristics when determining friction coefficient for flow velocity and bed shear stress calculations, as well as numerical model calibration. The optimally constructed distribution for each segment (Table. 4.6) has taken into account the local characteristics. Therefore, these distributions can be utilized for selecting friction coefficient in predicting flow velocity and bed shear stress. For example, the representative friction coefficient (e.g. mean friction factor) can be obtained and it can be utilized to extract various values for applying different friction coefficients in different spatial locations.



(a)



(b)

Figure 4.7: (a) Distribution of form roughness height (b) Distribution of Chezy coefficient (Color dot: empirical cumulative distribution function for observed value; Red solid line : fitted probability density function)

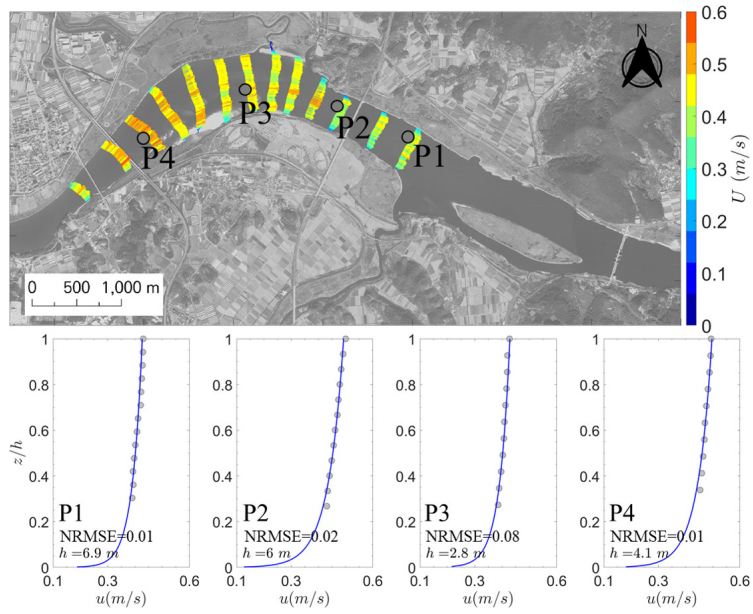
Table 4.6: Parameters of the probability density function estimated for each segment

		Form roughness height ($k_{s,f}$)		Chezy coefficient (C)	
	Distribution	Parameter		Distribution	Parameter
ND-GJ	GEV	location (μ)=0.0764 scale (σ)=0.0549 shape (ξ)=0.4236		Weibull	scale (λ) =56.3 shape (k)=11.4
ND-DS	GEV	location (μ)=0.0787 scale (σ)=0.0619 shape (ξ)=0.4930		Weibull	scale (λ)=53.4 shape (k)=10.2
ND-HC	GEV	location (μ)=0.0972 scale (σ)=0.0614 shape (ξ)=0.2099		Weibull	scale (λ)=53.9 shape (k)=11.8
ND-CN	Gamma	scale (β)=0.1037 shape (α)=2.2774		GEV	location (μ)=42.5 scale (σ)=5.3 shape (ξ)=-0.23

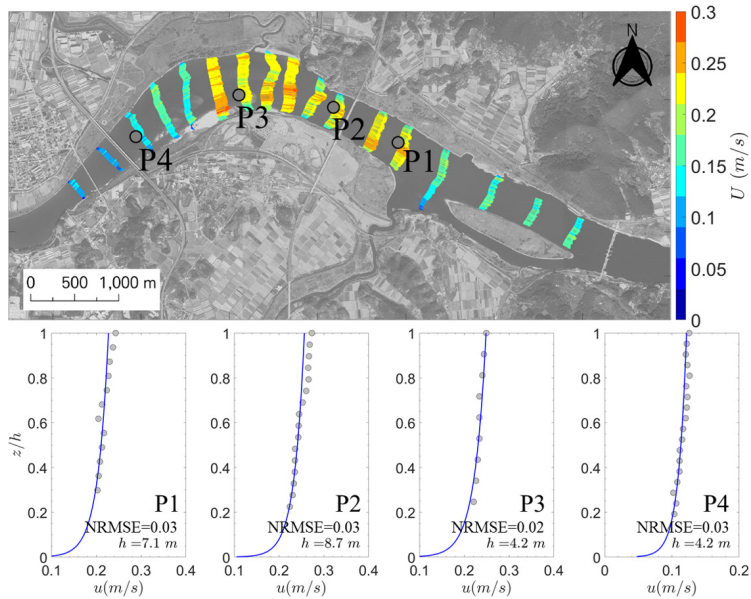
4.5 Discussion

4.5.1 Bed shear stress in the Nakdong River

In this section, the influence of the form roughness height on bed shear stress is investigated. Two different methods are used (Eq. 4.4, 4.5), and the correlation between the results obtained using the two methods is examined because the bed shear stress can differ depending on the chosen method (Sime et al., 2007). To calculate bed shear stress through Eq. 4.4, the shear velocity is determined from the log-law fitting and the comparison with the measured velocity at selected points are shown in Fig. 4.8. The average NRMSE (normalized root mean square error) for the entire log-law fitting results is 0.05, with a standard deviation of 0.04 and a range from 0.01 to 0.22. NRMSE is obtained by dividing RMSE (root mean square error) by the average of the measured value.



(a)



(b)

Figure 4.8: Vertical velocity profile at selected points and logarithmic velocity profile at selected points (a) ND-CH1 (b) ND-CH2 (Gray dot: the measured velocity; Blue solid line: the logarithmic velocity profile)

Fig. 4.9 presents the correlation between the total bed shear stress calculated through the two different methods. The form roughness height is taken into account to calculate $\tau_{b,log}$ and $\tau_{b,U}$. The bed shear stress calculated using the log-law is denoted by adding *log* as a subscript to the bed shear stress symbol (τ_b), and the bed shear stress calculated using the depth-averaged velocity is denoted by adding *U* as a subscript to τ_b . The comparison results show differences in the calculated bed shear stress values based on the method used, however, there is a high correlation between the two results. The results confirm that the bed shear stress is reasonably calculated based on the field measurements of flow velocity and friction coefficient.

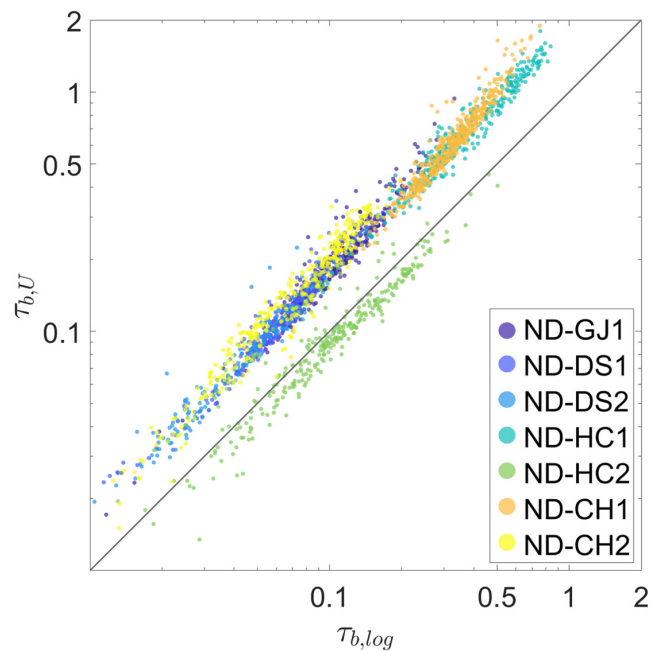


Figure 4.9: Correlation plot of bed shear stress computed by the log-law and depth-average velocity

Grain bed shear stress and total bed shear stress are compared to examine the influence of bedforms on bed shear stress. Fig. 4.10 illustrates the relationship between the grain bed shear stress and form bed shear stress, as well as between grain bed shear stress and total bed shear stress. Each survey section and survey time are represented by markers with different colors. Although the influence of bedforms on the bed shear stress varies depending on the method used to calculate bed shear stress, it is consistently observed that considering bedforms results in an increase in the bed shear stress compared to the case where only grain roughness is considered. This is an obvious result because when examining Eq. 4.5, as the Chezy coefficient is in the denominator, an increase in the roughness height leads to a decrease in Chezy coefficient. Under the same velocity conditions, the bed shear stress increases by decreasing Chezy coefficient. The relationships between the grain bed shear stress ($\tau_{b,g}$) and total bed shear stress (τ_b) depending on the calculation methods are as follows,

$$\tau_{b,log} = 1.717\tau_{b,g,log}, \quad (4.15)$$

$$\tau_{b,U} = 3.794\tau_{b,g,U}. \quad (4.16)$$

This implies that the bed shear stress due to bedform accounts for more than 60% of the total bed shear stress. The calculation results confirmed that in ND-River which is a sandy river with developed bedforms, a significant proportion of bed shear stress is attributed to bedforms, consistent with previous research findings. In subcritical flow conditions, the influence of form bed shear stress could be greater than grain bed shear stress (Chanson, 2004). Numerical investigation reported that the bed shear stress can increase by at least 50% along the bedform (Lefebvre et al., 2014). The field measurement results also suggested that

in areas where bedforms are developed, the form bed shear stress may have a greater impact on the total bed shear stress compared to grain bed shear stress (Kostaschuk et al., 2004).

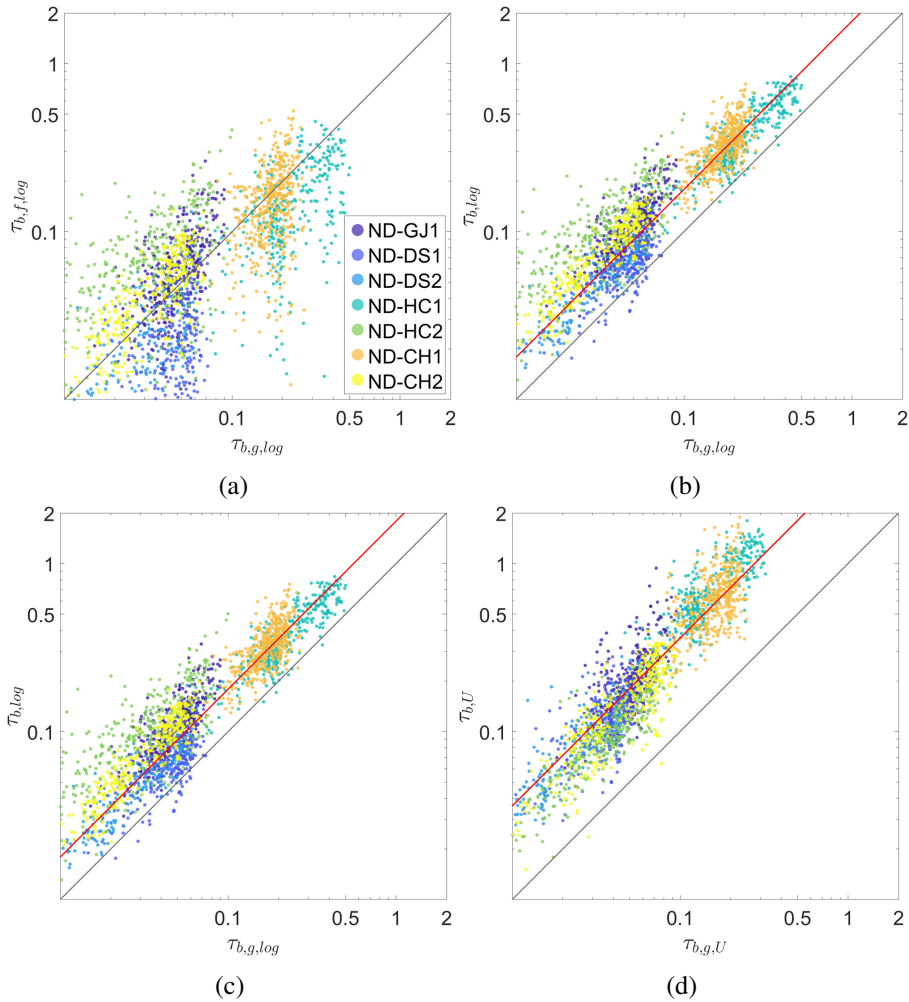


Figure 4.10: Bed shear stress in ND-GJ, ND-DS, ND-HC, and ND-CH (a) Comparison of grain bed shear stress and form bed shear stress computed using log-law (b) Comparison of grain bed shear stress and total bed shear stress computed using log-law (Red solid line represents $\tau_{b,log} = 1.717\tau_{b,g,log}$) (c) Comparison of grain bed shear stress and form bed shear stress computed using depth-average velocity (d) Comparison of grain bed shear stress and total bed shear stress computed using depth-average velocity (Red solid line represents $\tau_{b,U} = 3.794\tau_{b,g,U}$)

The calculation results for bed shear stress show the importance of taking into account the influence of bedforms on the bed shear stress. Neglecting the contribution of form roughness height may result in an underestimation of bed shear stress, leading to inaccuracies in predicting sediment transport and bed changes. Morphodynamic models typically establish a threshold for the initiation of sediment particle motion on the bed, determined by the critical bed shear stress depending on the grain size. The assumption is that when the bed shear stress does not exceed this threshold, particles in the riverbed remain stationary. Therefore, accurate prediction of bed shear stress becomes crucial for modeling sediment transport.

The potential impact of underestimating bed shear stress on the erosion phase is explored based on field measurement data. For this analysis, the distribution of grain bed shear stress and bed shear stress, considering the influence of bedforms, is compared. The critical bed shear stress for sand particles is considered in this comparison, ranging from 0.11 to 0.47 *pa* (as cited in Julien (2010)).

Fig. 4.11 shows the comparison of bed shear stress magnitudes with and without considering the form roughness height for ND-CH1 and ND-CH2. Among the velocity measurement sections, ND-CH is the section where the average Chezy coefficient is lowest due to the influence of bedforms. The average form roughness heights for ND-CH1 and ND-CH2 are 74.4 mm and 122.5 mm, respectively. When considering the form roughness height in the calculation of friction coefficient, the average Chezy coefficients for ND-CH1 and ND-CH2 are found to be 46 $m^{1/2}/s$ and 43 $m^{1/2}/s$, respectively. This represents a reduction in Chezy coefficient by approximately 1.6 times compared to cases where only grain roughness height is considered, which yielded Chezy coefficients of 75 $m^{1/2}/s$ for ND-CH1 and 67 $m^{1/2}/s$ for ND-CH2. Such a significant change in Chezy coefficient also impacts the bed shear stress. The region also experienced significant changes in bed level

before and after flood season, making accurate prediction of bed changes essential. The section within the black box in Fig. 4.11 indicates areas where the bed shear stress exceeds the critical bed shear stress (0.194 pa for medium sand, $d_s > 0.25 \text{ mm}$). Compared to the calculation considering only sand particles, it is observed that larger areas with bed shear stress exceeding the critical value occur when considering the influence of bedforms.

For ND-CH1, under flow conditions with larger than 95th percentile, even when considering only sand particles, bed shear stress exceeding the critical value is calculated, indicating potential erosion in some sections. However, when compared to the case considering bedforms, it can be inferred that bed erosion might be underestimated. In the case of ND-CH2, where the flow condition is below 90th percentile, considered the low-flow condition compared to ND-CH1. In this case, without considering the influence of bedforms, the bed shear stress within the survey area does not exceed the critical bed shear stress, expecting no risk of bed erosion. However, considering the bedform effect reveals bed shear stress exceeding the critical value between the cross-sections CHS6 and CHS13, indicating a potential for bed erosion. Thus, in the bed conditions where bedforms are developed, neglecting their influence may lead to underestimation of bed shear stress, resulting in potential errors in predicting bed changes.

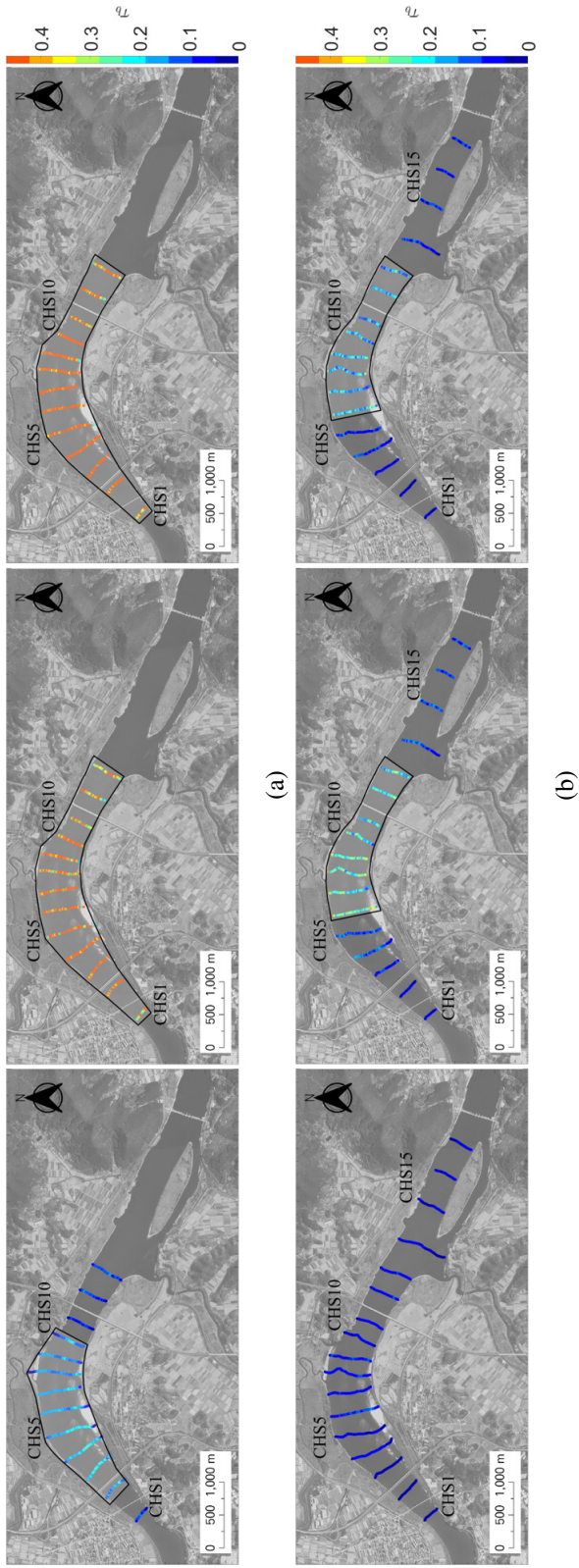


Figure 4.11: Comparison of the grain bed shear stress, form bed shear stress, and total bed shear stress calculated using depth-average velocity. (a) Distribution of the grain bed shear stress (left), the form bed shear stress (middle), and the total bed shear stress (right) for ND-CH1. (a) Distribution of the grain bed shear stress (left), the form bed shear stress (middle), and the total bed shear stress (right) for ND-CH2.

4.6 Concluding remarks

A method for estimating friction coefficients using measured bathymetry data is proposed. One notable aspect of this study is the estimation of form roughness height and friction coefficient using cross-sectional data in the transverse direction. The proposed method is suitable for sandy rivers, especially when the formation of bedforms significantly contributes to the total bed shear stress. It supplements the limitations of the conventional method that analyze bedforms using bathymetry data in the streamwise direction. Analyzing bedforms using streamwise bed profiles has limitations in understanding variations in bottom friction and bed shear stress across the channel width. However, the proposed method characterizes the friction coefficient across the channel width and allows for the analysis of the spatial distribution of bed shear stress using the obtained friction coefficient.

To accurately estimate the form roughness height, it is essential to analyze the characteristics of bedforms because the form roughness height is the function of bedform height and length. When analyzing bedform characteristics using bed profiles in the transverse direction, the bedform height can be estimated through the zero-crossing of filtered bed profiles, however, there is a limitation in estimating the bedform length. Therefore, in addition to the cross-sectional data, the measured bed profiles in the streamwise direction are utilized to incorporate the characteristics of bedform development in the interested section into the cross-sectional data analysis. Especially, the empirical relationship for estimating bedform length from bedform height is derived, taking into account the field characteristics.

The proposed method is applied to four segments of the Nakdong River in South Korea. The applied results demonstrate a high correlation between the form roughness height estimated through the streamwise direction and those estimated using transverse direction measured data. It shows that reasonable results consistent with traditional methods

of analyzing bedforms and estimating form roughness height using the streamwise direction data can be obtained.

The ability to estimate friction factor considering the influence of bedforms based on the cross-sectional data indicates that spatial data can be analyzed using ADCP-measured data. Particularly, considering the influence of bedforms in estimating bed shear stress can contribute to understanding the impact of bed shear stress on hydraulic phenomena, such as sediment transport and river morphology. In the analysis of four segments of the Nakdong River, the bed shear stress increases by an average of 1.7 times when calculated using the log-law method, and when using the depth-averaged velocity for the bed shear stress calculation, the total bed shear stress increases by an average 3.8 times, compared to calculations considering only grain roughness height. These increases can significantly influence sediment transport and morphodynamic analysis. This emphasizes the importance of including the bedform effect in the bed shear stress estimations. Moreover, analyzing the spatial distribution characteristics of the estimated friction coefficients allows for the examination of friction coefficient distribution features in the area of interest. In other words, the distribution of these estimated friction coefficients facilitates statistical analysis and the creation of a probability density function that accurately depicts this distribution. These results enable the determination of key values of friction coefficient that reflect field conditions for the calibration of numerical model. Additionally, the established probability density function for friction coefficient can be utilized to derive friction coefficients that represent the spatial variations in river environments.

The proposed method could be applicable to sandy rivers where bedforms have developed and is considered a practical approach for estimating bottom friction and bed shear stress. However, applying the proposed method requires an understanding of bedform length

characteristics such as their relation to bedform height. These characteristics can vary depending on the river, influencing the analysis results. Therefore, further river surveys are necessary to identify the bedform characteristics specific to other sandy rivers.

Chapter 5. CALIBRATION OF NUMERICAL MODEL USING FRICTION FACTOR DISTRIBUTION

5.1 Introduction

Numerical simulation is widely used to predict the hydrodynamics of rivers. Large eddy simulation has great potential to examine sophisticated phenomena (Rodi et al., 2013; Khosronejad et al., 2016). However, large eddy simulation requires high computational costs. Thus, a numerical model based on the shallow-water equations is widely used to predict river flow. The shallow-water equations are derived by integrating vertically Navier-Stokes equations with some assumptions. One of the fundamental assumptions is the no-slip boundary condition on the bed, which is related to the bed shear stress. The friction coefficient and roughness height are required to calculate the bed shear stress in the models such as Delft3d (Deltares, 2020), Telemac (Hervouet, 2007), EFDC (Hamrick, 2007), and MIKE3D MIKE21 and MIKE3 Flow Model (2009), and they influence accuracy and stabilize the numerical model (Dao and Tkalich, 2007; Gelfenbaum et al., 2011; Williams et al., 2013; Parsapour-Moghaddam and Rennie, 2018; Yang et al., 2021). Therefore, the appropriate friction coefficient must be determined to calibrate the numerical model. Nevertheless, the determination of the friction coefficient is still a significant challenge.

Recent advancements in field instrumentation made it possible to collect high-resolution bathymetry data as well as flow fields in the natural riverine environment and research were conducted on method for distinguishing bedforms and analyzing bedform characteristics using obtained bathymetry data (Van der Mark et al., 2008; Cataño-Lopera et al., 2009;

^oThis chapter is reproduced from the part of following publication: Lee, Park, Lee, & Lyu (2024). KSCE Journal of Civil Engineering, 28:1108-1121.

Cazenave et al., 2013; Porcile et al., 2020) Form roughness predictors were suggested and the form roughness can be calculated using the following geometric variables: length, height, and steepness of the bedform (Van Rijn, 1993; Soulsby, 1997; Bartholdy et al., 2010; Lefebvre and Winter, 2016). It implies that the form roughness can be estimated through analyzing obtained bathymetry data. Although several studies have tried to develop techniques to understand the distribution of the bedforms over the river bed, few attempted to determine friction factor based on the result of the bedform analysis.

The study in Chapter 5 aims to determine the friction coefficient considering the form roughness based on the geometry of the bedform obtained from the field survey data and to demonstrate that the determined friction coefficient is suitable for calibration of the numerical model.

5.2 Field experiment

5.2.1 Study Site

Fig. 5.1 shows the study site with survey lines. The study site is located downstream of the Hapcheon-Changnyeong weir in the Nakdong River. The Hwang River joins the Nakdong River 1.6 km downstream from the Hapcheon-Changnyeong weir. The mean channel width and water depth in the surveyed reach are 230 m and 4 m, respectively. The river bed slope between the cross-sections NHS2 and NHS6 is about 5×10^{-4} . Ten field surveys were conducted and hydraulic data including the bed profile were acquired at six selected cross-sections.

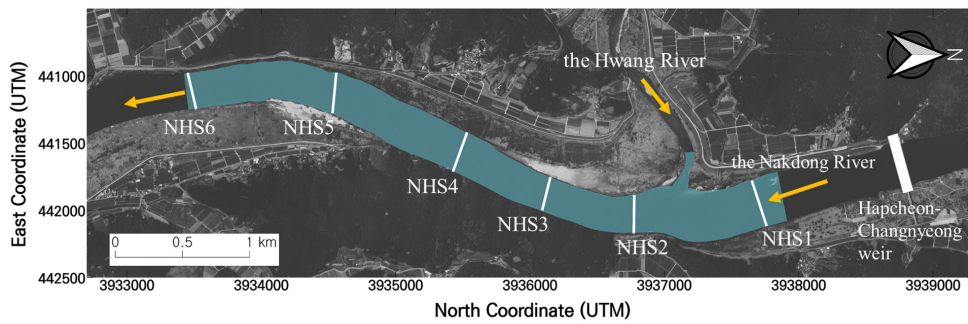


Figure 5.1: Study site of the study in Chapter 5. Downstream of the Hapcheon-Changnyeong weir in the Nakdong River. The region with blue color is the computational domain and white solid lines are survey lines.

5.2.2 Field data

The flow velocity and water depth were measured by an acoustic Doppler current profiler (ADCP, Sontek RiverSurveyor M9) mounted on a moving boat to collect the data on the cross-sections shown in Fig. 5.1. The flow conditions on the field survey dates are listed in Table 5.1. The discharges listed in Table 5.1 are daily average discharge and they are referenced from the website (www.mywater.or.kr). The ranges of daily average discharge for the Nakdong River are $59.2 \text{ m}^3/\text{s}$ to $573.5 \text{ m}^3/\text{s}$. These discharge conditions on the survey date ranges from low to high discharge conditions compared with the annual mean discharge. The annual mean discharges of outflow of the Hapcheon-Changnyeong weir in the Nakdong River were $187 \text{ m}^3/\text{s}$ in 2019 and $362 \text{ m}^3/\text{s}$ in 2020. Details of the field survey method and results can be found in MOE (2022).

Fig. 5.2 shows the bed profiles on the date of the field surveys. As observed in Fig. 5.2, the bed profiles change under the erosion and sedimentation processes. Increased flow discharge results in accelerated change of bed profiles. Large discharges occurred in the flood season during which the discharges over 95th percentile mostly occurred (Fig. 5.3). The discharges corresponded to 95% and 99% between 2013 and 2020 at the site are $610 \text{ m}^3/\text{s}$ and $2,265 \text{ m}^3/\text{s}$, respectively. The frequency of discharge over 95% in 2020 is higher than those in other years, which resulted in more severe changes to the bed profile during the period. A survey report is referred to for information on the grain size at the study site (MOLIT, 2017; MOE, 2018, 2019). The sediment particles in the bed in the study area are primarily composed of sandy soil ($d_{50} = 0.36\text{mm}$ in the Nakdong River; $d_{50} = 0.50\text{mm}$ in the Hwang River).

Table 5.1: Daily mean discharge at the study site. Q_{NH} is the outflow from the Hapcheon-Changnyeong weir; Q_H is the discharge of the Hwang River

Survey Date	Q_{NH} (m^3/s)	Q_H (m^3/s)
Jun 25, 2019	104.8	9.1
Aug 1, 2019	103.7	11.5
Aug 23, 2019	573.5	30.5
Apr 16, 2020	59.2	15.7
Apr 27, 2020	64.1	21.9
May 27, 2020	106.3	19.6
Aug 24, 2020	379.2	253.3
Nov 2, 2020	70.7	9.7
Mar 30, 2021	149.8	15.0
Apr 14, 2021	153.4	16.4

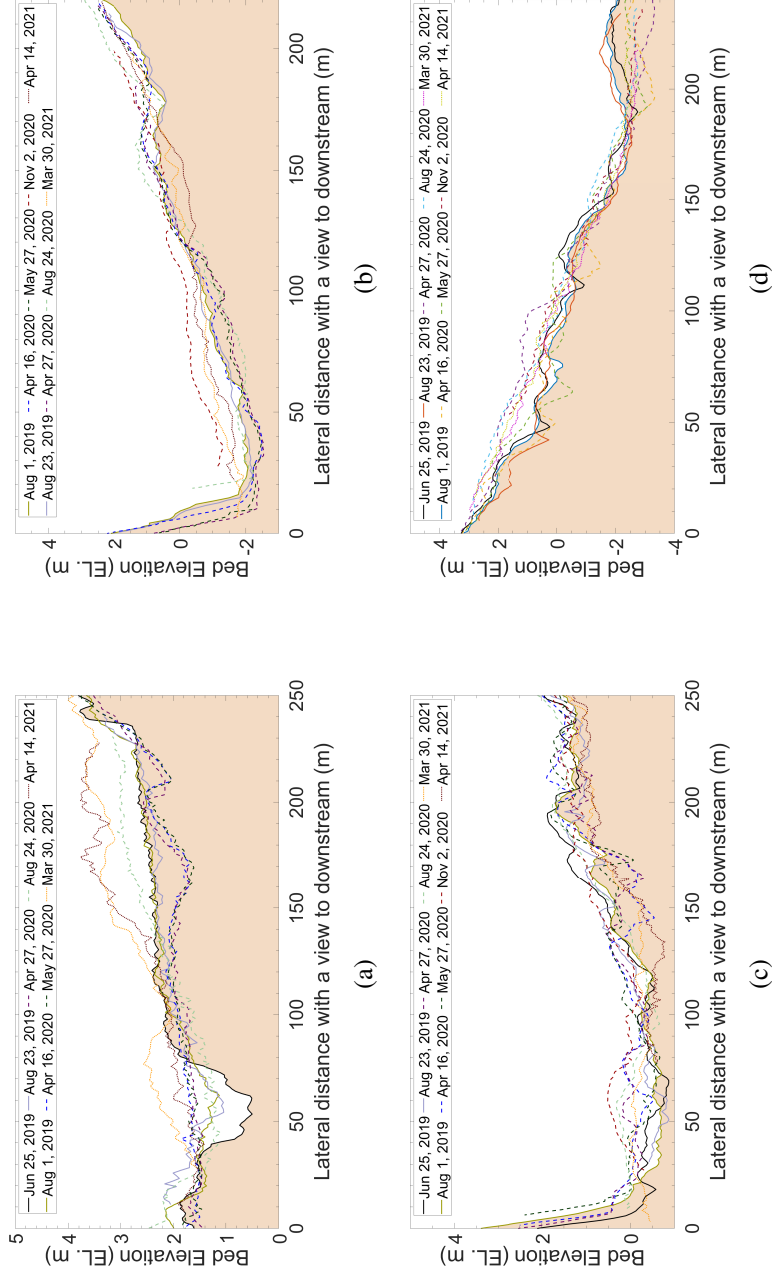


Figure 5.2: Changes in the bed elevation in each cross-section (a) NHS2 (b) NHS3 (c) NHS4 (d) NHS5. A Solid line along the brown area is the bed elevation measured on the first field survey, and other colors show the bed elevation on subsequent field surveys, respectively.

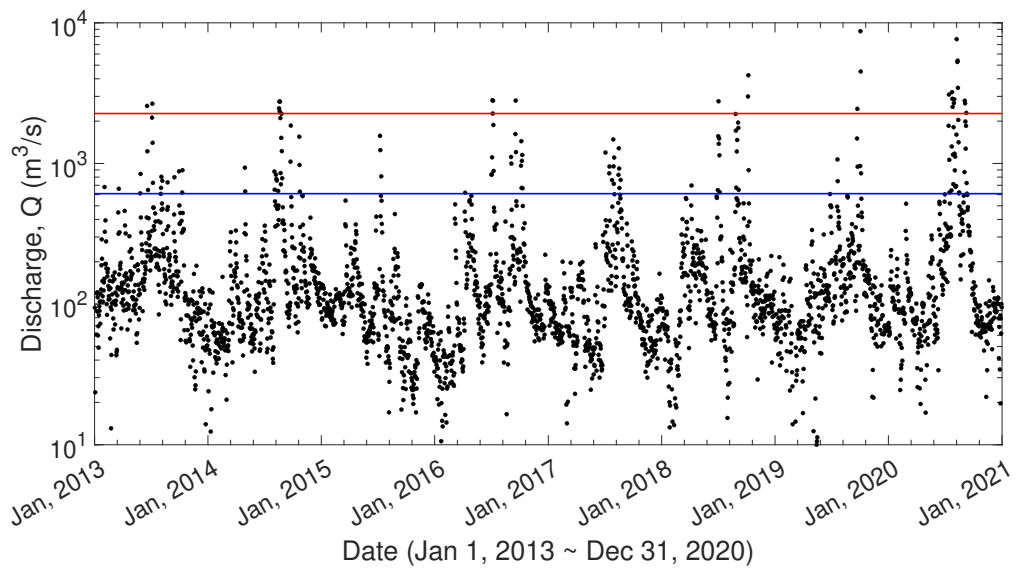


Figure 5.3: Variation of the daily average discharge of outflow from the Hapcheon-Changnyeong weir from 2013 to 2020 (Black circle: the daily averaged discharge; Blue line: the discharge corresponding to 95th percentile of outflow from the Hapcheon-Changnyeong weir; Red line: the discharge corresponding to 99th percentile of outflow from the Hapcheon-Changnyeong weir)

5.3 Estimation of bedform friction factor

5.3.1 Calculation of bedform friction factor

Bed shear stress (τ_b) consists of stresses due to grain ($\tau_{b,g}$) and bedform ($\tau_{b,f}$) (Eq. 5.1); Van Rijn (1993); Julien (2010)) Darcy-Weisbach friction factor (f) and the Chezy coefficient (C) can be written as Eq. 5.2 and Eq. 5.3, respectively. The relationship between Darcy-Weisbach friction factor and Chezy coefficient shown as below (Yen, 2002):

$$\tau_b = \tau_{b,g} + \tau_{b,f} \quad (5.1)$$

$$f = f_g + f_f \quad (5.2)$$

$$\frac{1}{C^2} = \frac{1}{C_g^2} + \frac{1}{C_f^2} \quad (5.3)$$

τ_b and f can be formulated using Chezy coefficient (Eqs. 5.4, 5.5, and 5.6):

$$\tau_b = \frac{\rho g U^2}{C^2} \quad (5.4)$$

$$f = \frac{8g}{C^2} \quad (5.5)$$

$$C = \frac{2.3\sqrt{g}}{\kappa} \log\left(\frac{12h}{k_s}\right) \quad (5.6)$$

where ρ is water density, g is gravity acceleration, U is flow velocity, κ is von Kármán constant which is 0.4, h is water depth; k_s is roughness height. The roughness height is separately expressed for grain roughness, $k_{s,g}$, and form roughness, $k_{s,f}$. Chezy coefficient

can be obtained by integration of logarithmic velocity profile Van Rijn (1993)

$$\bar{u} = \frac{1}{h} \int_{z_0}^h \frac{u_*}{\kappa} \ln \frac{z}{z_0} dz = \frac{u_*}{\kappa} \left[-1 + \ln \frac{h}{z_0} \right] \quad (5.7)$$

$$\frac{\bar{u}}{u_*} = \frac{C}{\sqrt{g}} \quad (5.8)$$

with the relations $\bar{u} = C\sqrt{hI}$ and $u_* = \sqrt{ghI}$ where z_0 is hydraulic roughness height; I is the water surface slope.

$k_{s,g}$ is proportional to the representative sediment size, $k_{s,g} = \alpha d_*$ where d_* is the representative sediment size, the subscript * indicates the grain size fraction, and α is a constant. The grain roughness height is taken from $k_{s,g} = 3d_{90}$ as suggested by Van Rijn (1993). The representative sediment size ($d_{90} = 0.70mm$) is taken from the reported value in MOE (2019). Formulas for the form roughness height have been proposed by Van Rijn (1993); Soulsby (1997); Bartholdy et al. (2010) (Table 5.2). The form roughness height is estimated using equations listed in Table 5.2, and the results are compared in Chapter 5.3.3. In Table 5.2, Δ_f is bedform height and Λ_f is bedform length.

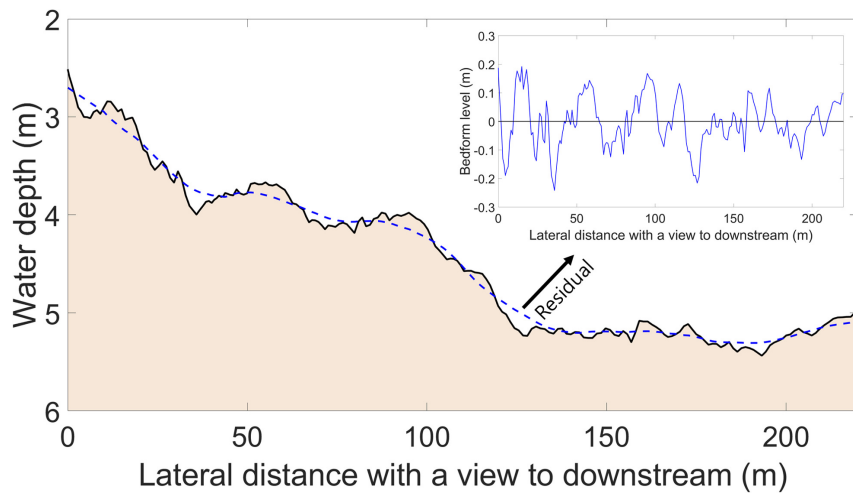
Table 5.2: Form roughness predictors

Form roughness height	Reference
$k_{s,f} = 1.1\Delta_f \left(1 - \exp \left(-25\Delta_f / \Lambda_f \right) \right)$	Van Rijn, 1993 (VR1993)
$k_{s,f} = \frac{30\Delta_f^2}{\Lambda_f}$	Soulsby, 1997 (Soulsby1997)
$k_{s,f} = 0.57\Delta_f$	Bartholdy et al., 2010 (BAR2010)

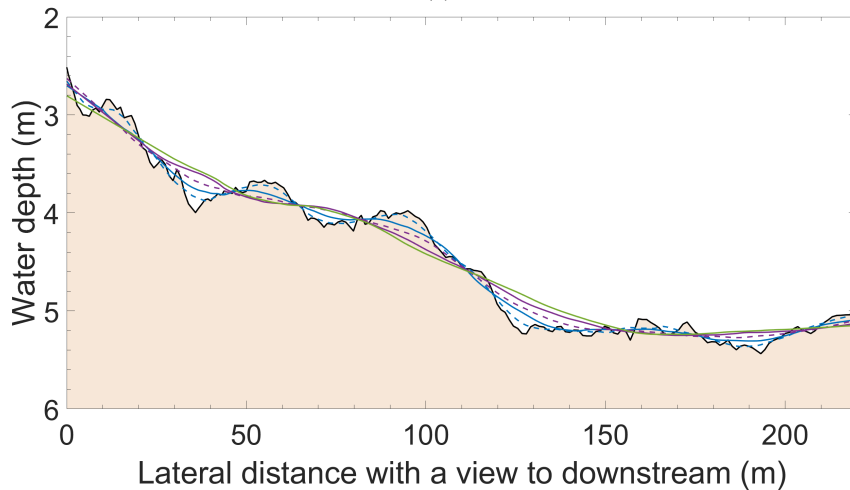
5.3.2 Determination of bedform geometry

Information on the geometric variables of bedform, Δ_f and Λ_f , is necessary to calculate the form roughness. The zero-crossing method is adopted to determine the height of bedform from the field-measured bed profiles (Van der Mark et al., 2008; Wang et al., 2020). The bedform height is defined as a distance between crest and trough and crest and trough points can be found between zero-crossings. To calculate the bedform height using the zero-crossing method, the reference level (or zero level) should be set (Fig. 5.4(a)). The bedform height is estimated from the residual which is obtained by subtracting the field-smoothed bed profile from the field-measured bed profile (subfigure in Fig. 5.4(a)). In the study in Chapter 5, the smoothed bed profile which is derived through Friedman's super smoother (Friedman, 1984) is set as the reference level. Friedman's super smoother is based on a local linear regression with bandwidth (span size), which ranges from 0 to 1. The super smoother shows good performance in estimating bed profile where neighboring values change without abrupt variations (Kim et al., 2013). Different smoothing results could be obtained depending on the span size (SS), where SS determines the number of neighboring data points used for averaging. The smoothing function, *supsmu* in *R*, is used (Wickham et al., 2019).

The smoothing results could vary with the span size. Thus, it is expected that geometric variables of the bedform could vary with the reference level. In other words, it is one of the sensitive parameters to the friction coefficient which is calculated based on the bed profile Fig. 5.4(b) shows the results of comparing how the smoothing result varies according to the span size.



(a)



(b)

Figure 5.4: Estimation of the bedform height using the zero-crossing method (a) Example of the field-measured bed profile (black solid line) and smoothed bed profile (blue dot line) in NHS5 and the bedform height defined from the residual bed level (b) Comparison between the field-measured bed profile and smoothed bed profiles using the 5 different span size (SS=0.05, 0.1, 0.15, 0.2, and 0.25) (Black solid line: the measured bed profile; Blue solid line: SS=0.05; Blue dot line: SS=0.1; Purple solid line: SS=0.15; Purple dot line: SS=0.2; Green solid line: SS=0.25)

The bedform dimensions could be over-estimated with increasing span size due to excessive smoothing of the bed profiles. As the ratio between bedform height and water depth is known to be less than 0.36 (Julien, 2010), over-estimated bedforms that have a ratio greater than 0.36 are removed from the distribution in the calculations.

In river modeling, the geometric parameters of the bedform were defined based on a bed profile in the streamwise direction (Gutierrez et al., 2013). However, only the cross-sectional data in the normal direction of the river are available. Therefore, the bedform height from the survey data is taken and the length of bedform is estimated using its relationship with the water depth (Van Rijn, 1993), which is given in Eq. 5.9:

$$\Lambda_f / h = 7.3, \quad (5.9)$$

Then, form roughness is calculated by substituting the estimated bedform height and bedform length into the form predictors listed in Table . Finally, the Chezy coefficient corresponding to the geometric variables of the bedform can be get.

5.3.3 Distribution of roughness

The bottom friction factor is discussed in terms of the Chezy coefficient (Eq. 5.3 and Eq. 5.6). First, distributions of the Chezy coefficients for the study site are compared depending on the smoothed bed profiles. Bedforms are discriminated from the bed profiles obtained from 10 field surveys and Chezy coefficient is calculated based on the bedform information and local water depth. In this process, the bedform height and Chezy coefficient are estimated while varying the smoothness of bed profile to examine the effect of smoothness of bed profile. The smoothness of bed profile could be controlled by span size. Then, empirical cumulative distribution function (ECDF) of Chezy coefficient calculated for each span size

is computed, and ECDFs are compared (Fig. 5.5). ECDF of the Chezy coefficient is obtained through *ECDF* function in Matlab.

Table 5.3 lists the mean, standard deviation, and skewness of the Chezy coefficients according to the span size and form predictors. The number of data used for the calculations in Table 5.3 is an average of 1,513 in case of span size=0.2 and an average of 4,081 in case of span size=0.05. Three form predictors listed in Table 5.3 are applied to calculate the Chezy coefficients. The mean of the Chezy coefficients decreases as the span size increases. The mean value varies by 10% as the span size varies from 0.05 to 0.20. These variations occurs because the height of bedform which is estimated based on the smoothed bed level, changed depending on the smoothness of bed profile. The estimated bedform height could increase as increasing smoothness of the bed profile in result Chezy coefficient could decrease by the relationship, $C \propto k_s^{-1} \Delta_f / \Lambda_f$. The Mean, standard deviation and skewness of the Chezy coefficient which is calculated based on Manning's n value are listed in Table 5.4.

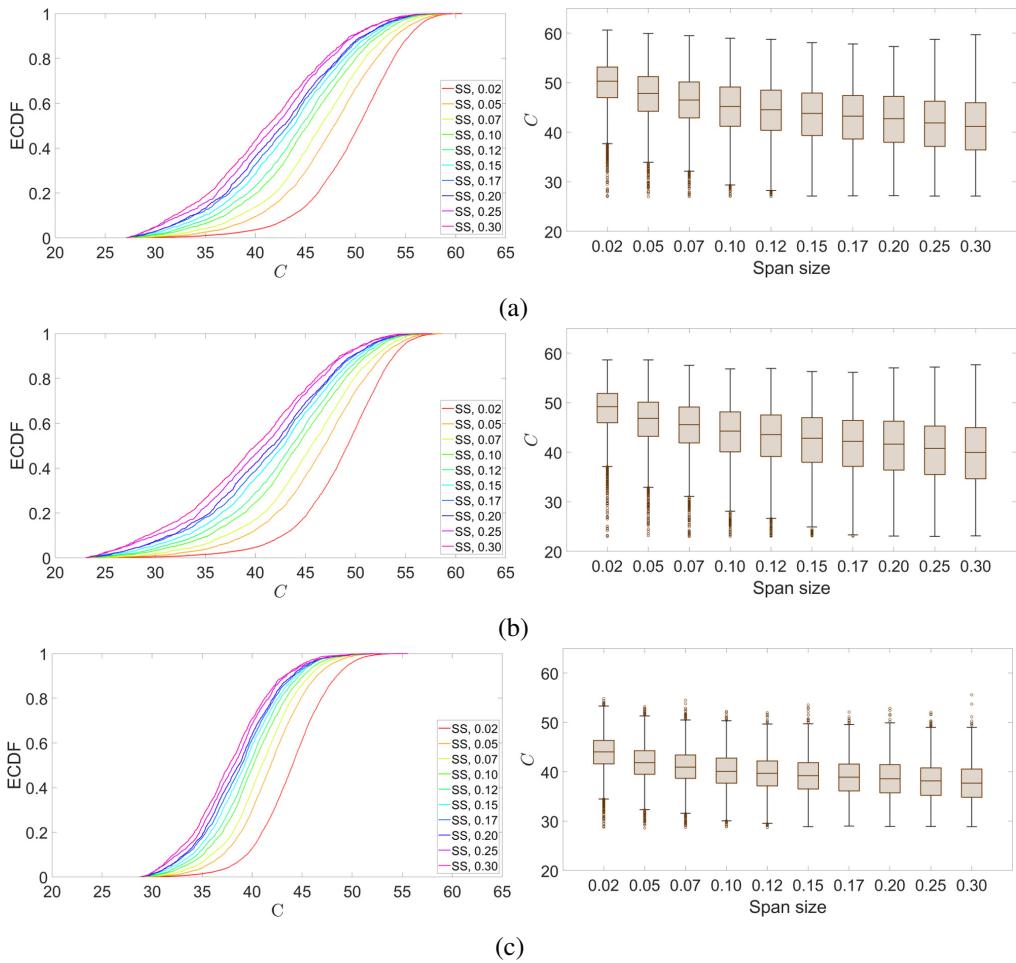


Figure 5.5: Distribution and box plot of the Chezy coefficients according to the span size and form roughness predictors. The Chezy coefficients are calculated using three different form predictors (a) VR1993 (b) Soulsby 1997 and (c) BAR2010.

Table 5.3: Mean, standard deviation (Std), and skewness (Skew) of the estimated Chezy coefficients depending on the smoothness and form predictors

Span Size	0.05			0.10			0.15			0.20		
	Mean	Std	Skew									
VR1993	47.4	5.4	-0.5	44.8	5.9	-0.4	43.4	4.2	-0.3	42.5	6.4	-0.1
Soulsby1997	46.2	5.5	-0.8	43.6	6.2	-0.6	42.0	6.6	-0.5	41.1	6.9	-0.3
BAR2010	41.8	3.7	-0.2	40.1	3.9	-0.1	39.2	4.0	0.0	38.6	4.1	0.2

Table 5.4: Mean, standard deviation (Std), and skewness (Skew) of the estimated Chezy coefficients depending on Manning's n values

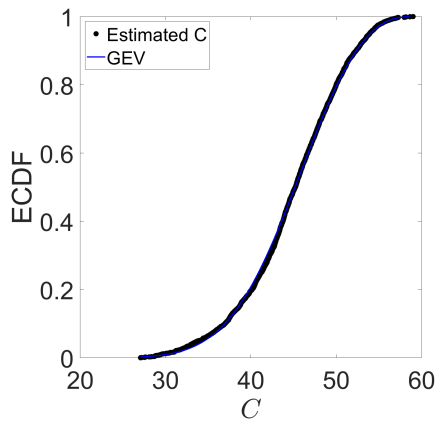
Manning's n	0.020	0.025	0.030	0.035
Mean	61.5	49.3	41.1	35.3
Std	5.2	4.1	3.4	2.9
Skew	-0.4	-0.4	-0.4	-0.4

VR1993 and Soulby1997 resulted in a distribution with non-zero skewness, implying that the normal distribution would not fit. On the other hand, the skewness is close to zero when BAR2010 is used. The statistical parameters for various PDFs are estimated and the best-fit PDF of the Chezy coefficient is determined and comparison between the calculated Chezy coefficient and the fitted PDF is shown in Fig. 6. The matlab function *fitdist* is used to calculate parameters for the PDF. The parameters for five PDFs, Weibull, GEV, Gamma, Lognormal, and Normal distribution are derived and the errors between the original data and fitted PDFs are calculated to determine the best-fit PDF. As observed in Table 5.5, the fitted PDF with the lowest error accurately represents the distribution of the calculated Chezy coefficients based on the field data. GEV and Weibull distributions well represented the distribution of the Chezy coefficients calculated through VR1993 and Soulsby1997, and the normal distribution fitted accurately with Chezy coefficient estimated by BAR2010. The calculated Chezy coefficient values range between $20 \text{ m}^{1/2}/\text{s}$ and $60 \text{ m}^{1/2}/\text{s}$ and exhibit spatial variability. Thus, the Chezy coefficient values for each grid cell is obtained from the fitted PDF and applied to the numerical model as a friction coefficient.

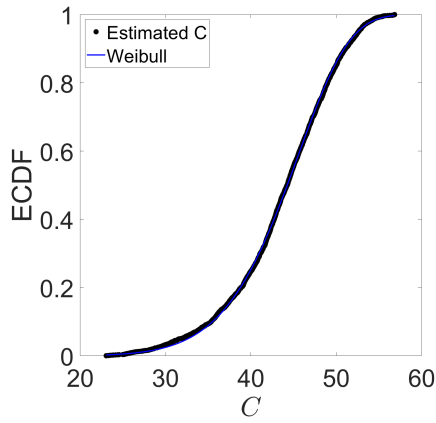
Manning's n values are calculated from the estimated Chezy coefficient using Eq. 5.14. In results, the minimum value of Manning's n is 0.02 and the value corresponding to 0.9 of the distribution of calculated Manning's n is 0.035. To compare the sensitivity and accuracy of the numerical results using the Manning coefficient, Manning's n values within the range of 0.02 to 0.035 are applied to the numerical model, and the results are compared with those obtained using the method proposed in this study.

Table 5.5: Probability density function error

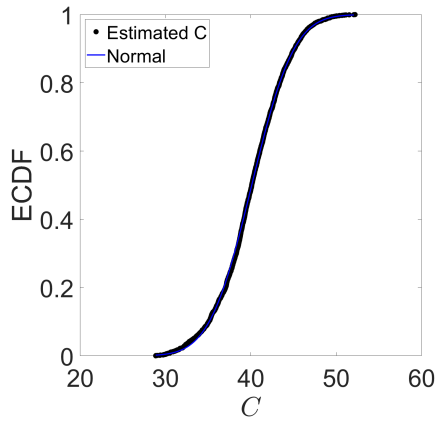
Form Predictor	Weibull	GEV	Gamma	Lognormal	Normal
VR1993	0.010	0.009	0.029	0.035	0.018
Soulsby1997	0.006	0.013	0.041	0.048	0.028
BAR2010	0.028	0.013	0.014	0.018	0.008



(a)



(b)



(c)

Figure 5.6: Comparison between the computed Chezy coefficients and the fitted probability density function according to form predictors (a) VR1993 (b) Soulsby1997 (c) BAR2010

5.4 Numerical modeling

5.4.1 Delft3D

Delft3D modeling package which has been developed by Deltares was used to simulate flows in the study site. To simulate three-dimensional flow, Delft3D solves 3D shallow-water equations consisting of the continuity equation and two horizontal momentum equations with Boussinesq assumptions for incompressible flow (Eq. 5.10-5.12)

$$\frac{\partial \eta}{\partial t} + \frac{\partial(hU)}{\partial x} + \frac{\partial(hV)}{\partial y} = 0, \quad (5.10)$$

$$\frac{\partial u}{\partial t} + u \frac{\partial u}{\partial x} + v \frac{\partial u}{\partial y} + w \frac{\partial u}{\partial z} = -g \frac{\partial \eta}{\partial x} + \nu_H \left(\frac{\partial^2 u}{\partial x^2} + \frac{\partial^2 u}{\partial y^2} \right) + \frac{\partial}{\partial z} \left(\nu_V \frac{\partial u}{\partial z} \right), \quad (5.11)$$

$$\frac{\partial v}{\partial t} + u \frac{\partial v}{\partial x} + v \frac{\partial v}{\partial y} + w \frac{\partial v}{\partial z} = -g \frac{\partial \eta}{\partial y} + \nu_H \left(\frac{\partial^2 v}{\partial x^2} + \frac{\partial^2 v}{\partial y^2} \right) + \frac{\partial}{\partial z} \left(\nu_V \frac{\partial v}{\partial z} \right), \quad (5.12)$$

where η is the water level; U and V are depth-averaged velocity in horizontal direction; u and v are velocity components in horizontal direction; w is vertical velocity component; g is gravitational acceleration; t is time; ν_H and ν_V are horizontal eddy viscosity and vertical eddy viscosity, respectively. Vertical momentum equation is neglected and it can lead to the hydrostatic pressure assumption. The vertical velocity is calculated using the continuity equation.

Two vertical coordinate systems, σ -coordinate system and Z -model can be chosen to simulate three-dimensional flow. σ -coordinate system was adopted for the three-dimensional numerical analysis in this study.

A quadratic bottom shear stress formulation is used at the bottom (Eq. 5.13) and the formula includes the Chezy coefficient which can be related to water depth and Manning's

n value or roughness height (Eq. 5.14 and Eq. 5.15, respectively) as below (Deltares, 2020).

$$\tau_b = \frac{\rho g u_b |u_b|}{C^2}, \quad (5.13)$$

$$C = \frac{h^{1/6}}{n}, \quad (5.14)$$

$$C = 18 \log_{10}(12h/k_s), \quad (5.15)$$

where u_b is velocity in bottom layer. One of the roughness parameters (Chezy coefficient or Manning's n) can be chosen to calculate the bottom shear stress. In the study described in Chapter 5, different roughness values which were generated from the best-fit PDF were applied to each grid cell. Then, the model performance is assessed to examine the applicability of the presented bottom friction factor estimation method. The models with constant Manning's n values, 0.02, 0.025, 0.03, and 0.035, were additionally established for comparison with the numerical model with the presented bottom friction factor estimation method.

The horizontal eddy viscosity should be selected to calibrate the numerical model and it is a superposition of three parts as Eq. 5.16:

$$\nu_H = \nu_{SGS} + \nu_V + \nu_H^{back}, \quad (5.16)$$

where ν_{SGS} is sub-grid scale (SGS) horizontal eddy viscosity and is computed by SGS turbulence model when HLES (Horizontal Large Eddy Simulation) option is turned on. The background horizontal eddy viscosity, ν_H^{back} is a user-specified value. The vertical eddy viscosity, ν_V , is calculated by the turbulence closure model. In the study in Chapter 5, HLES option was turned on, and ν_H^{back} was set to 0. $k - \epsilon$ turbulence closure model was employed.

The computational domain covers the study site shown in Fig. 5.1. For the reach of the

Nakdong River, the computational grid is consisted of 377 cells in the streamwise direction and 41 cells in the transverse direction. The computational grid for the Hwang River is consisted of 38 cells in the streamwise direction and 12 cells in the transverse direction. The average grid sizes in the streamwise direction and the transverse direction are 11.8 m and 7.1 m, respectively. The number of layers in the vertical direction is 14. Bathymetry data obtained by intensive field survey (MOE, 2022) was used to generate depth information. The discharge and water level boundary conditions were applied at the upstream boundary and the downstream boundary, respectively. The hourly averaged discharge and water level were set as boundary values; these data were downloaded from the website (<https://www.water.or.kr/>) that provides recorded data at gauging stations installed along the rivers in South Korea.

5.4.2 Simulation cases

A total of 36 numerical simulations were conducted under both low and high flow conditions with two different kinds of form roughness predictors (VR1993 and BAR2010) as well as Manning's n values. Table 5.6 shows the simulation conditions including the boundary conditions, the horizontal eddy viscosity, and the bottom friction factor. In Table 5.6 and hereinafter, BBC denotes the cases with the Chezy coefficients randomly generated from best-fit PDF. The distribution of Chezy coefficient applied to the numerical model generated from fitted PDF is shown in Fig. 5.7(a) and the distributions of Chezy coefficient according to the Manning's n in the range of 0.02 to 0.035 are shown in Fig. 5.7(b)-(e). HLES denotes the column labeled Horizontal Eddy Viscosity in Table 5.6 means that horizontal eddy viscosity was mainly calculated using the HLES model and the background horizontal eddy viscosity of 0 was applied in the numerical model.

To estimate the roughness and its effect on the numerical results, the accuracy of the

model is assessed using the root mean square error (RMSE) between the simulated results (x_{mod}) and the field-measured data (x_{obs}):

$$RMSE = \sqrt{\frac{\sum(x_{mod} - x_{obs})^2}{m}}, \quad (5.17)$$

where m is the sample size. The simulation results are compared to field-measured velocity collected at the survey lines shown in Fig. 5.1. The simulations were performed using 8 or 12 processors on Dell Precision 7920 Tower with 40 Cores. The wall-clock time was approximately 20 - 24 hours for each simulation case.

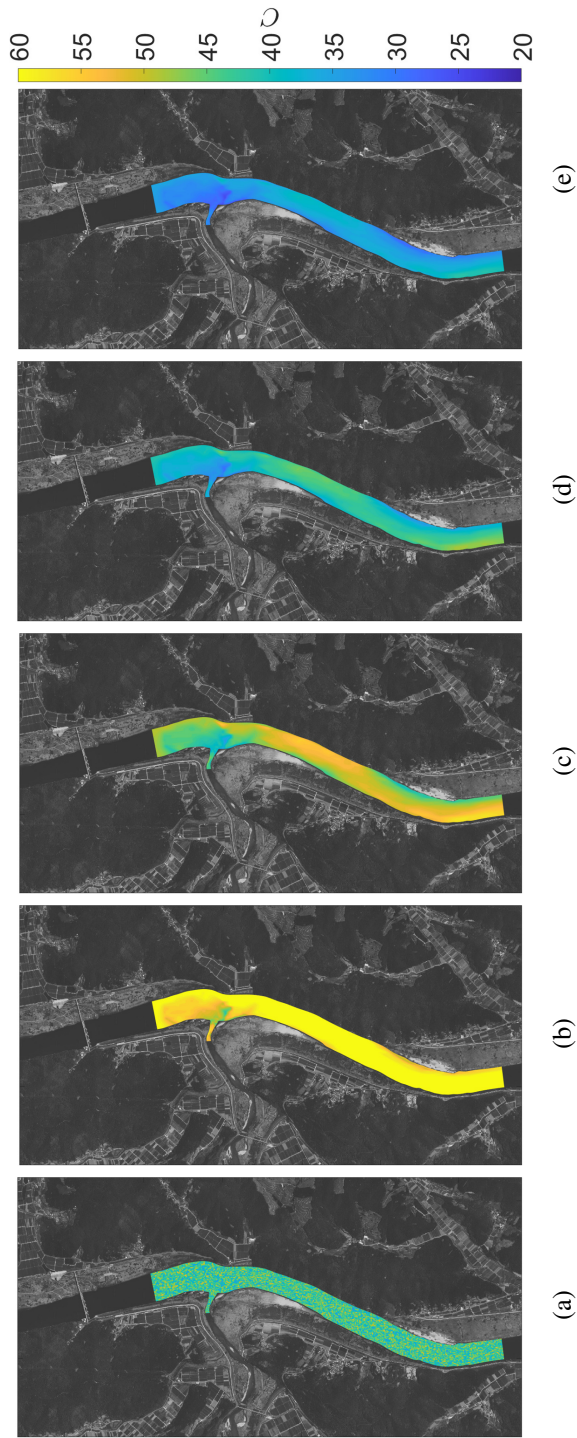


Figure 5.7: Example of distribution of Chezy coefficient (a) Q2V15 (b) Q2M20 (c) Q2M25 (d) Q2M30 (e) Q2M35

Table 5.6: Simulation Cases for the Study Site. Q_{NH} is the Outflow from the Hapcheon-Changnyeong weir; Q_H is the Discharge of the Hwang River. SP Denotes Span Size

Simulation case	Q (m ³ /s)	Roughness	Horizontal eddy viscosity
Q1V05	$Q_N = 574\text{m}^3/\text{s}$ $Q_G = 31\text{m}^3/\text{s}$	BBC (VR1993, SP=0.05)	HLES ($v_H^{back} = 0$)
Q1V10		BBC (VR1993, SP=0.10)	HLES ($v_H^{back} = 0$)
Q1V15		BBC (VR1993, SP=0.15)	HLES ($v_H^{back} = 0$)
Q1V20		BBC (VR1993, SP=0.20)	HLES ($v_H^{back} = 0$)
Q1B05		BBC (BAR2010, SP=0.05)	HLES ($v_H^{back} = 0$)
Q1B10		BBC (BAR2010, SP=0.10)	HLES ($v_H^{back} = 0$)
Q1B15		BBC (BAR2010, SP=0.15)	HLES ($v_H^{back} = 0$)
Q1B20		BBC (BAR2010, SP=0.20)	HLES ($v_H^{back} = 0$)
Q1M20		Manning's n , 0.020	HLES ($v_H^{back} = 0$)
Q1M25		Manning's n , 0.025	HLES ($v_H^{back} = 0$)
Q1M30		Manning's n , 0.030	HLES ($v_H^{back} = 0$)
Q1M35		Manning's n , 0.035	HLES ($v_H^{back} = 0$)
Q2V05		$Q_N = 380\text{m}^3/\text{s}$ $Q_G = 253\text{m}^3/\text{s}$	BBC (VR1993, SP=0.05)
Q2V10	BBC (VR1993, SP=0.10)		HLES ($v_H^{back} = 0$)
Q2V15	BBC (VR1993, SP=0.15)		HLES ($v_H^{back} = 0$)
Q2V20	BBC (VR1993, SP=0.20)		HLES ($v_H^{back} = 0$)
Q2B05	BBC (BAR2010, SP=0.05)		HLES ($v_H^{back} = 0$)
Q2B10	BBC (BAR2010, SP=0.10)		HLES ($v_H^{back} = 0$)
Q2B15	BBC (BAR2010, SP=0.15)		HLES ($v_H^{back} = 0$)
Q2B20	BBC (BAR2010, SP=0.20)		HLES ($v_H^{back} = 0$)
Q2M20	Manning, 0.020		HLES ($v_H^{back} = 0$)
Q2M25	Manning, 0.025		HLES ($v_H^{back} = 0$)
Q2M30	Manning, 0.030		HLES ($v_H^{back} = 0$)
Q2M35	Manning, 0.035		HLES ($v_H^{back} = 0$)
Q3V05	$Q_N = 150\text{m}^3/\text{s}$ $Q_G = 15\text{m}^3/\text{s}$		BBC (VR1993, SP=0.05)
Q3V10		BBC (VR1993, SP=0.10)	HLES ($v_H^{back} = 0$)
Q3V15		BBC (VR1993, SP=0.15)	HLES ($v_H^{back} = 0$)
Q3V20		BBC (VR1993, SP=0.20)	HLES ($v_H^{back} = 0$)
Q3B05		BBC (BAR2010, SP=0.05)	HLES ($v_H^{back} = 0$)
Q3B10		BBC (BAR2010, SP=0.10)	HLES ($v_H^{back} = 0$)
Q3B15		BBC (BAR2010, SP=0.15)	HLES ($v_H^{back} = 0$)
Q3B20		BBC (BAR2010, SP=0.20)	HLES ($v_H^{back} = 0$)
Q3M20		Manning's n , 0.020	HLES ($v_H^{back} = 0$)
Q3M25		Manning's n , 0.025	HLES ($v_H^{back} = 0$)
Q3M30		Manning's n , 0.030	HLES ($v_H^{back} = 0$)
Q3M35		Manning's n , 0.035	HLES ($v_H^{back} = 0$)

5.5 Results and discussions

5.5.1 Calibration of eddy viscosity

Eddy viscosity is one of the essential parameters and it should be calibrated. Before the investigation of the sensitivity of the BBC, the simulation results with HLES option with $v_H^{back} = 0$ are examined. Simulated depth-averaged velocity and streamwise velocity distribution are compared to the measured data. Fig. 5.8 shows the depth-averaged velocity and Fig. 5.9 shows the streamwise velocity distribution. In the river confluence, flow acceleration occurs due to the inflow of tributary flow, and variations in flow velocities along the cross-section are evident near the junction. As the flow progresses downstream from the junction, the flow stabilizes, and the velocity distribution across the cross-section becomes more uniform. For example, under discharge condition Q1, at NHS2, the flow velocity on the left bank side reached up to 1 *m/s*, while on the right bank, it was about 0.7 *m/s*. On the other hand, at NHS4, the velocity distribution became nearly uniform across the cross-section with a mean flow velocity of 0.45 *m/s* and a velocity difference of less than 0.1 *m/s* between the left and right bank side. The numerical simulations accurately represent these variations in flow patterns shown Q1 discharge condition. Additionally, the numerical results have good agreement with the field-measured data for Q2 and Q3 discharge conditions. Consequently, given the successful representation of observed outcomes with the HLES option with $v_H^{back} = 0$, it is concluded that it is appropriate to use HLES option with $v_H^{back} = 0$. Hence, HLES option was adopted and set v_H^{back} to zero for all the simulation cases discussed below.

The simulated water depth is compared to measured data and RMSEs for the water depth are shown in Fig. 5.10. The mean of water depth in cross-sections NHS2 to NHS5

were 4.4 m on Aug 23, 2019, 4.6 m on Aug 24, 2020, and 3.9 m on Mar 30, 2021. The maximum RMSE is 0.48 m in NHS4 on Mar 30, 2021 and 0.47 m in NHS5 on Aug 23, 2019. The maximum value of RMSE is about 10 % relative to the mean water depth. Hence, the numerical simulation could represent the water depth as well.

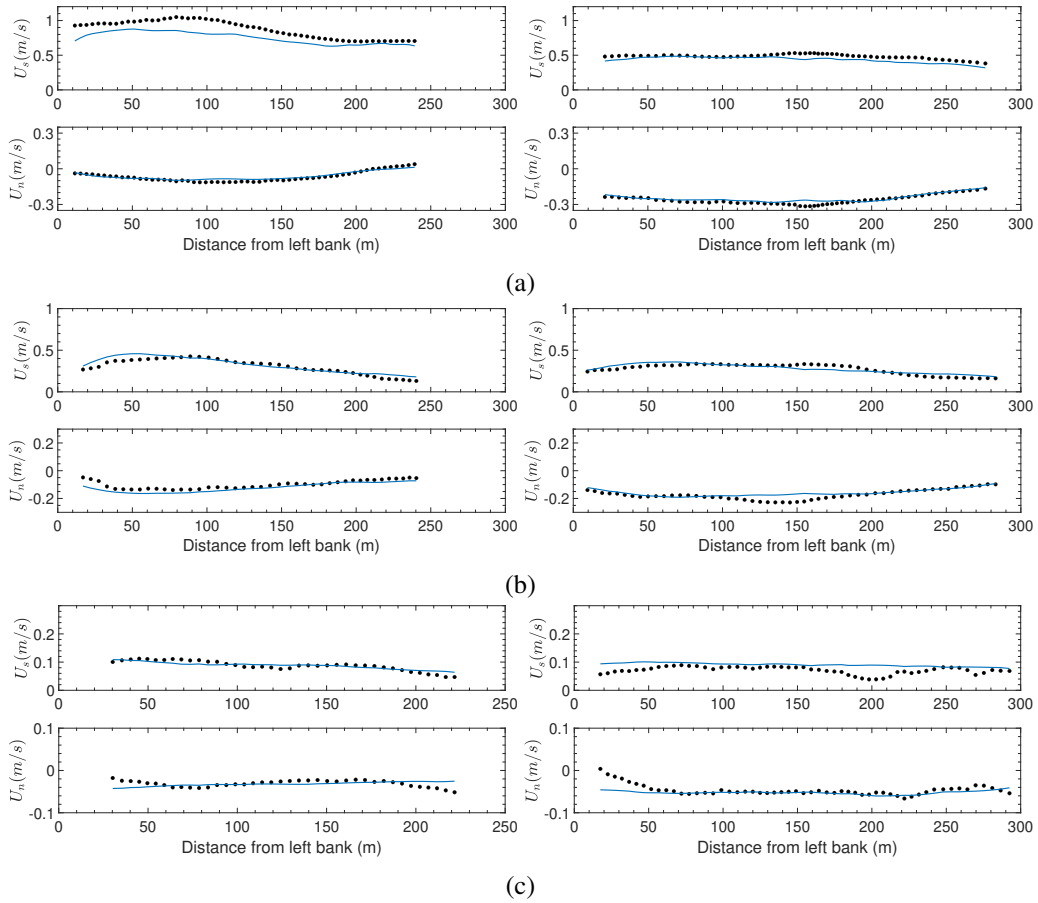


Figure 5.8: Comparison between the field-measured velocity and simulated velocities on the section NHS3 (left in subfigure) and NHS4 (right in subfigure) (Black dot: the field-measured velocity; Blue solid line: the simulated depth-averaged velocity) (a) Streamwise velocity (U_s) and transverse velocity (U_n) in case of Q1V10 (b) Streamwise and transverse velocity in case of Q2V10 (c) Streamwise and transverse velocity in case of Q3V10. Positive value of the transverse velocity represents the eastward transverse direction (toward to left bank) and negative value of the transverse velocity represents the westward transverse direction (toward to right bank).

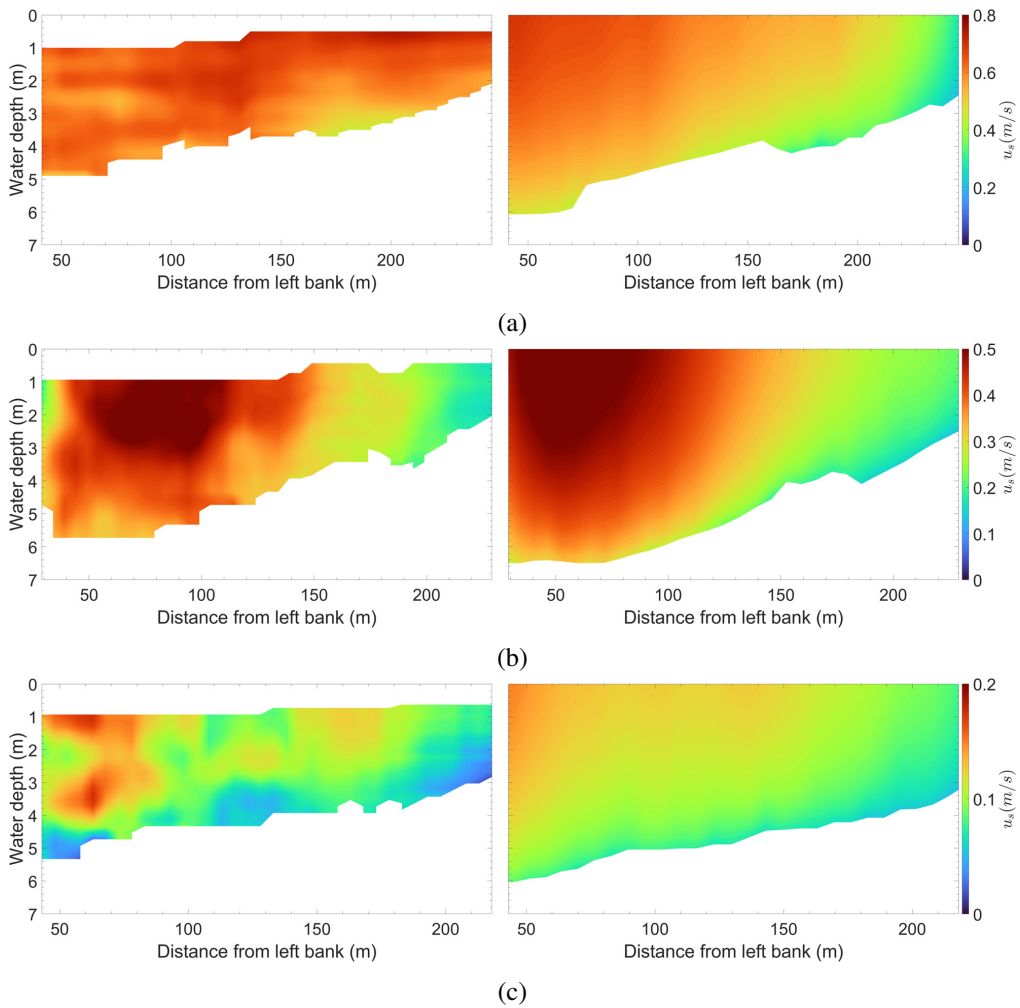


Figure 5.9: Comparison between the field-measured velocity and simulated velocities on section NHS3 (a) Q1V10 (b) Q2V10 (c) Q3V10 (Left in subfigure: the field-measured streamwise velocity; Right in subfigure: the simulated streamwise velocity; u_s : streamwise velocity)

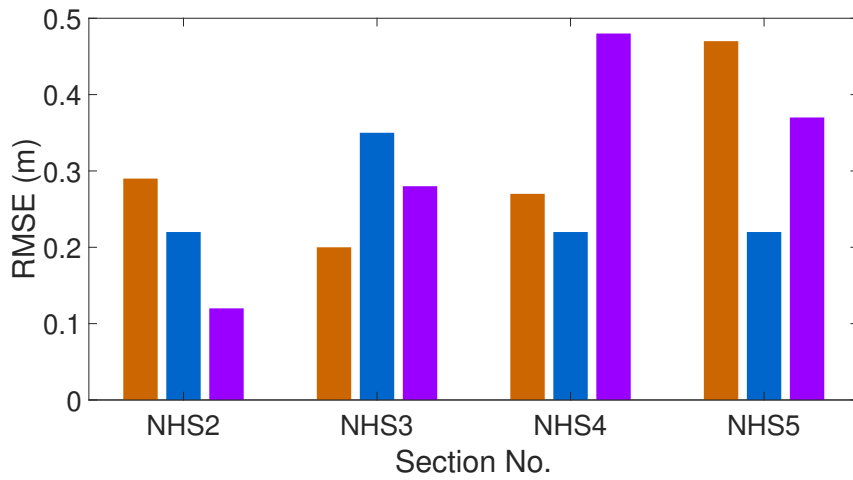


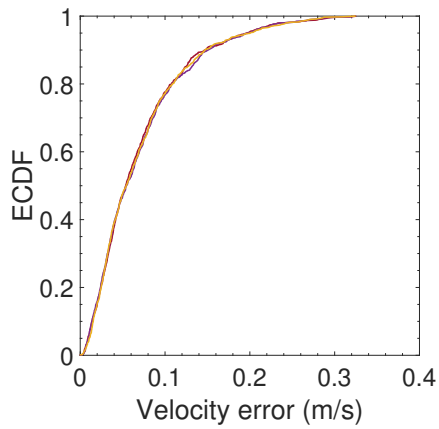
Figure 5.10: RMSE for the measured water depth and simulated water depth at NHS2-NHS5 (Orange bar graph: Q1V10; Blue bar graph: Q2V10; Purple bar graph: Q3V10)

5.5.2 Sensitivity of the model to random generation of Chezy coefficient from PDF

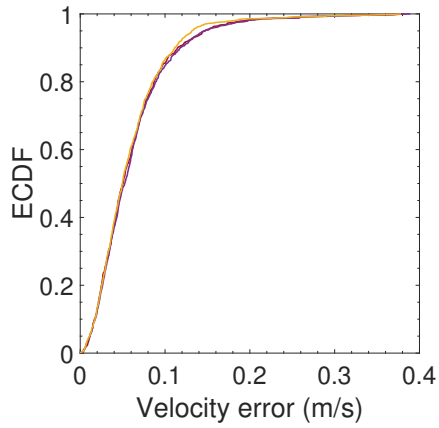
The sensitivity tests are performed to examine the effect of the variation of Chezy coefficients in each grid cell. Since Chezy coefficients applied to the grid cells were generated from best-fit PDF, it was expected that the applied Chezy coefficient in each grid cell could change every time they were generated.

For the sensitivity test, three sets of values of Chezy coefficients were created from the best-fit PDF for VR1993 with a span size=0.10 for three numerical models. As the three different sets of Chezy coefficients were applied to each case, 9 numerical simulations were conducted to investigate the sensitivity of the randomly generated Chezy coefficients.

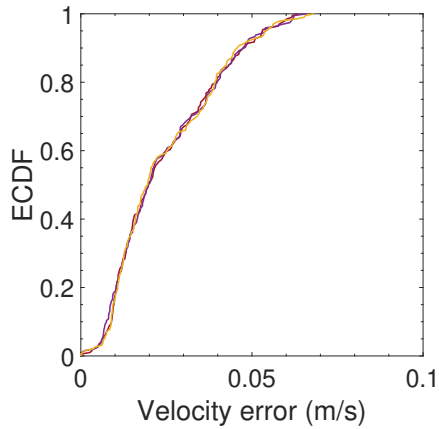
It can be seen that there are no significant differences between the models with different sets of roughness (Fig. 5.11). RMSEs between the different realizations are summarized in Table 5.7. The difference between the RMSE in the same case is less than 1%, except for Q2V10. However, this difference is relatively small compared to the mean velocity of Q2V10. In other words, when generating Chezy coefficients from the same fitted PDF for applying the numerical model, the numerical results are not sensitive, even though different values of Chezy coefficient are applied to each grid cell.



(a)



(b)



(c)

Figure 5.11: Comparison of the depth-averaged velocity error between the models with different roughness sets (a) Q1V10 (b) Q2V10 (c) Q3V10 (Red solid line: roughness case 1; Purple solid line: roughness case 2; Yellow solid line: roughness case 3)

Table 5.7: Velocity error for different roughness sets

	Q1V10	Q2V10	Q3V10
Roughness Case 1	0.0914	0.0781	0.0305
Roughness Case 2	0.0926	0.0797	0.0305
Roughness Case 3	0.0920	0.0752	0.0305

5.5.3 Sensitivity to smoothness and form roughness predictor

In this section, the sensitivity of the model to smoothness and form roughness predictors is investigated. The distribution of Chezy coefficients based on the field data could change depending on the smoothness of the bed profile and form predictors (Fig. 5.12). The Chezy coefficients were generated from best-fit PDF with four different span sizes, i.e. 0.05, 0.10, 0.15, and 0.20, and different form predictors, VR1993 and BAR2010. The mean, standard deviation, and skewness of Chezy coefficient according to Soulsby1997 are similar to those of VR1993 (Table 5.3). Therefore, sensitivity tests are conducted for the form predictors by comparing the numerical results to which VR1993 and BAR2010 were applied, respectively.

Models with different span sizes yield similar velocity errors (Fig. 5.12). The difference of RMSE depending on the span size is less than 5 % except in the series Q2 (Q2V05-Q2V20; Q2B05-Q2B20). Although the difference for the models of the Q2 series with different span sizes is larger than other cases, the maximum difference is about 8 % and its value is 0.007 *m/s*. This value is small compared to the mean velocity. The numerical results with VR1993 are more sensitive to the span size. In the series Q2, the maximum difference for the models with VR1993 is 0.0068, and it is 0.0008 for those with BAR2010.

The results are not significantly different between the models when only the form predictor is different and other conditions are same (Fig. 5.12). The range of RMSE of depth-averaged velocity for the models with the discharge condition with Q1 (Q1V05-Q1V20; Q1B05-Q1B20) is between 0.091 and 0.095 and the range for the models with the discharge condition with Q3 (Q2V05-Q2V20; Q3B05-Q3B20) is between 0.0295 and 0.0308. The difference between the model results with different form predictors and the same span size is less than 4% except for Q2 condition (range of the RMSE: 0.0734-0.0836). The maximum difference of RMSE between the models for Q2 is 11.8% and its value is 0.01

m/s. However, this difference is still small compared to the mean velocity.

It is observed that the differences in numerical results are small even though the applied Chezy coefficients change due to different smoothness and form predictors. This means that robust results can be obtained without strict adjustment of parameters such as span size.

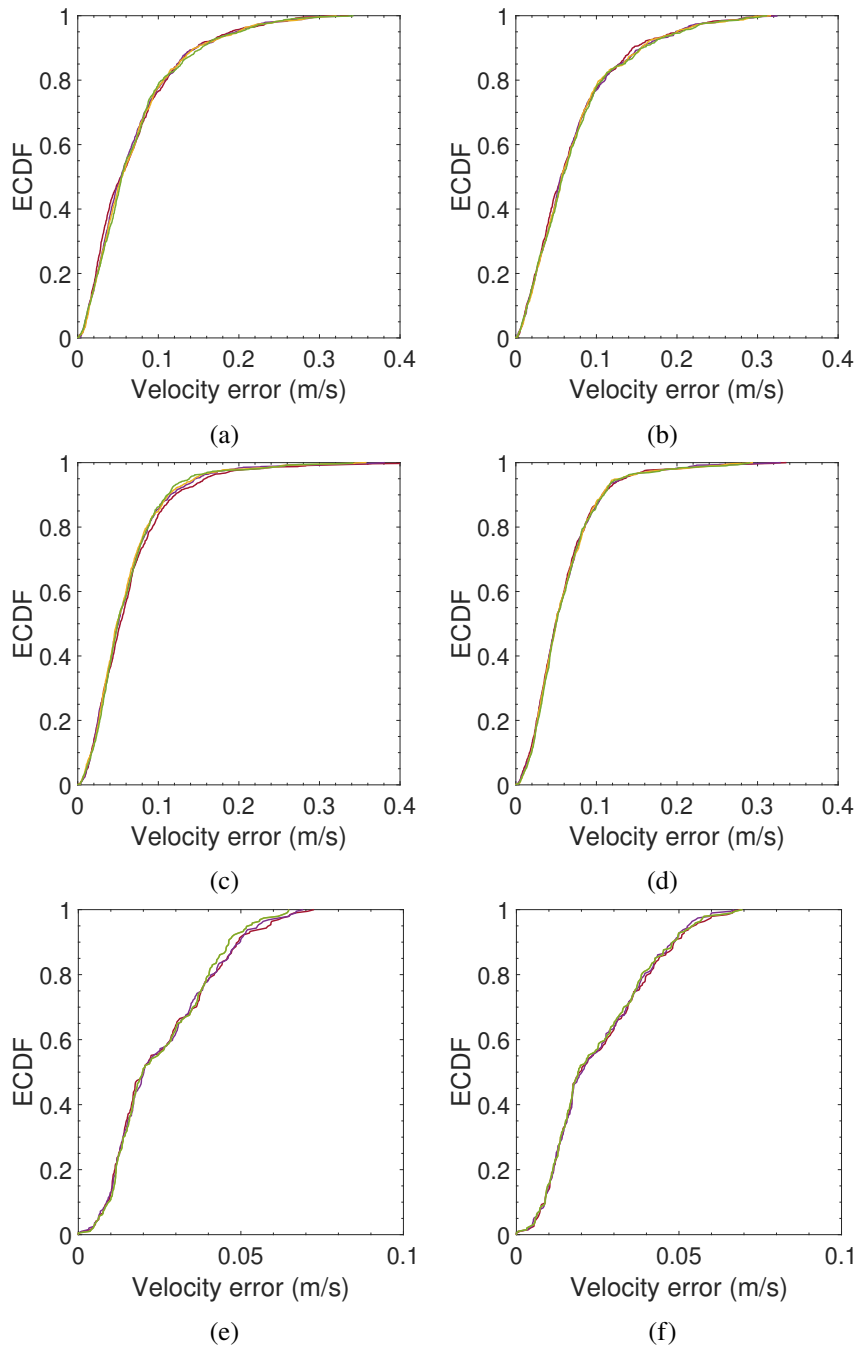


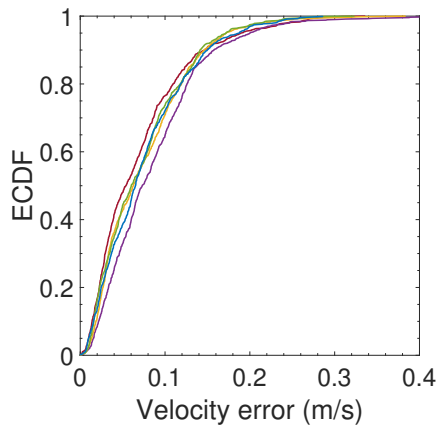
Figure 5.12: Depth-averaged velocity error depending on the smoothness and form Predictors, VR1993 and BAR2010 for: (a) Q1V05-Q1V20 (b) Q1B05-Q1B20 (c) Q2V05-Q2V20 (d) Q2B05-Q2B20 (e) Q3V05-Q3V20 (f) Q3B05-Q3B20 (Red solid line: span size =0.05; Purple solid line: span size = 0.10; Yellow solid line: span size = 0.15; Green solid line: span size = 0.20)

5.5.4 Comparison with Manning equation

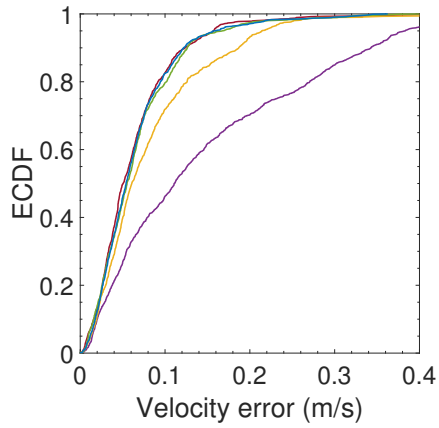
The numerical results between the models with the BBC and Manning's n value are compared to evaluate the performance and sensitivity. For this, four Manning's n values, $n = 0.02, 0.025, 0.03, \text{ and } 0.035$, were applied to the numerical model.

The change of numerical results due to different Manning's n values is markedly larger than the change in the roughness based on the BBC method (Fig. 5.13). The difference of RMSE between the models with Manning's n value is considerably larger. The maximum differences of RMSE for the simulation cases of Q1M, Q2M, and Q3M are 15.1 %, 57.3 %, and 18.4 %, respectively. The ranges of RMSE of depth-averaged velocity for the models, Q1M, Q2M, and Q3M are 0.090-0.106, 0.084-0.197, and 0.026-0.032, respectively. On the other hand, the maximum difference of RMSE for the simulation cases of Q1V, Q1B, Q2V, Q2B, Q3V, and Q2B are 2.84%, 11.84%, and 3.57%. Different Manning coefficients can lead to large variations in the numerical results.

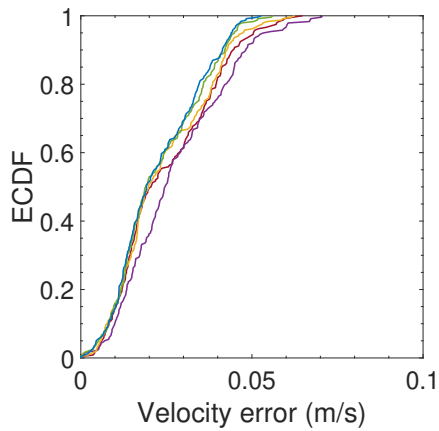
Nevertheless, numerical results with a constant Manning's n value can match the field-measured data reasonably well, while one needs to calibrate the value with trial and error for each case. This is a conventional process of model calibration. However, the numerical results are sensitive to Manning's n value especially around the region with a large velocity gradient (Fig. 5.14), while the numerical results with BBC do not change sensitively. Therefore, it is advantageous to apply non-uniform bottom roughness to the numerical model for better performance. It is concluded that the presented method for bottom friction coefficient can produce robust and accurate results without further calibration.



(a)



(b)



(c)

Figure 5.13: Cumulative distribution of depth averaged-velocity error for each validation cases; (a) Q1V15 and Q1M20-Q1M35 (b) Q2V15 and Q2M20-Q2M35 (c) Q3V15 and Q3M20-Q3M35 (Red: V15; Purple: M20; Yellow: M25; Green: M30; Blue: M35)

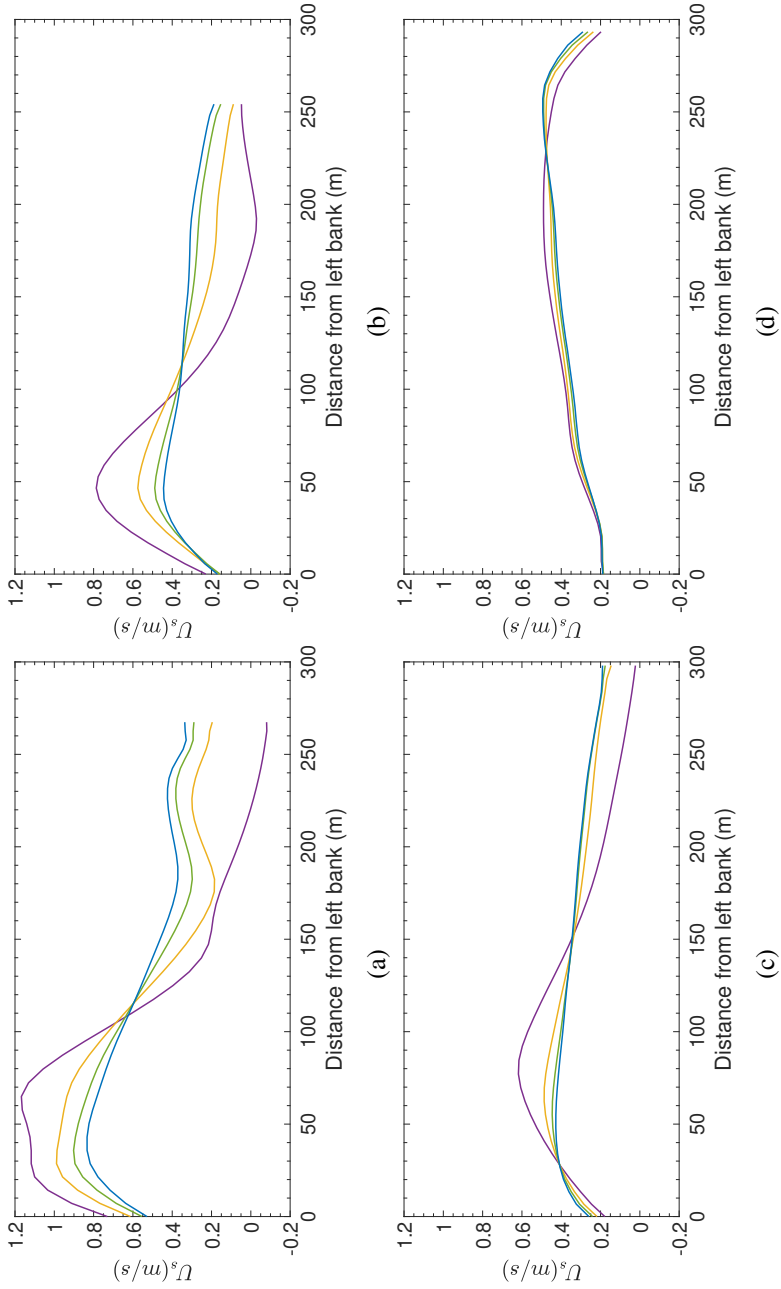


Figure 5.14: Comparison of the depth-average velocity results at NHS2-NHS5 for the numerical results with different Manning's n under Q2 flow condition: (a) NHS2, (b) NHS3, (c) NHS4, (d) NHS5 (Purple: Q2M20; Yellow: Q2M25; Green: Q2M30; Blue: Q2M35)

5.6 Concluding remarks

The bottom friction coefficient is an essential parameter required to solve shallow-water equations. The study in Chapter 5 proposes a novel method for estimating the bedform roughness using field survey data. The geometric parameters for the bedform are calculated using the bed profile obtained by acoustic Doppler current profiler. The zero-crossing method is applied to estimate the bedform dimensions. The form roughness is then estimated using empirical formulas as functions of the bedform height and length. A range of bedform sizes is obtained from the field survey data. The Chezy coefficients are calculated based on the estimated geometric parameters of the bedform. Subsequently, the PDF of Chezy coefficients is determined to randomly generate the Chezy coefficients, which are then applied to each grid cell. The uncertainties affecting the numerical results are investigated: (1) different roughness set by random generation from the PDF, (2) different form roughness predictors, and (3) different bedform dimensions due to the smoothness of the bed profiles. For all the cases considered in the present study, the new method exhibits good and robust agreement with the field data. In addition, the numerical results with the Chezy coefficients generated from the PDF are less sensitive than those with Manning's n . It is significant that the bedform friction factor can be obtained directly from the measured bathymetry data with virtually no calibration procedure.

Chapter 6. Conclusion

Roughness height, related to friction coefficient and bed shear stress, is a key parameter for predicting hydrodynamics and transport phenomena in shallow-water environments. Therefore, it is essential to estimate roughness height considering bed conditions. As roughness height is a function of the geometric variables of the rough elements, it can be determined through the surface analysis. This dissertation focuses on determining roughness height and applying it to the numerical model to enhance the calibration procedure.

Chapters 3 and 4 focus on estimating roughness height and friction coefficient in shallow-water environments, where various rough elements exist. However, methods for estimating the roughness height of all rough elements are not fully understood. A knowledge gap exists regarding the estimation of roughness height for oyster reefs, which are a major contributors to coastal roughness. Chapter 3 addresses this gap by conducting a study on methods to estimate the roughness height of oyster reefs. Unidirectional and oscillatory flow experiments were performed to analyze the correlation between roughness height and geometric variables of rough elements on oyster reef surfaces. The experiments resulted in the proposal of a roughness predictor ($k_{s,o} = 7\Delta_o$). This roughness predictor is validated by verifying its reproducibility in the velocity profile over oyster's rough surfaces. The suggested roughness predictor facilitates the estimation of roughness height distribution on oyster reef surfaces, allowing for the determination of a representative roughness height. This representative roughness height is expected to be useful for evaluating the applicability of oyster reefs as a nature-based solution.

Chapter 4 presents a study focused on developing an effective method for estimating friction coefficients in sandy rivers and assessing their utility. In sandy rivers, the primary

rough elements are the grain particles and bedforms, which critically influence friction coefficient estimation for accurate river flow analysis. Due to the heterogeneous development of bedforms both longitudinally and transversely, the roughness height and friction coefficient exhibit spatial variability. Therefore, an effective method is needed to capture this heterogeneity. The study proposes a method for estimating friction coefficients using transverse measurement data of the river. By employing this method, it is possible to estimate the distribution of friction coefficients and, when linked with high-resolution velocity measurement data, to estimate the bed shear stress distribution. The proposed method offers the advantage of providing high spatial resolution analysis data compared to methods using only bed profiles in the streamwise direction. Additionally, it considers the influence of both particles and bedforms, allowing for the estimation of increased bed shear stress due to bedforms, thereby enabling a more diverse range of scenarios for analyzing riverbed changes.

Chapter 5 builds upon the assumption established in Chapter 3 and 4, which suggests that the roughness height can be determined from geometric variables of rough elements. This chapter focuses on determining roughness height (or friction coefficient) that accurately represents surface conditions for numerical model calibration. Chapter 4 highlights the crucial roles of grain and form roughness heights in determining bed shear stress in sandy rivers. For effective numerical model calibration, it is essential to select a roughness height (or friction factor) that accounts for bedform influences. The method from Chapter 3 and 4 is applied to estimate the distribution of roughness height and friction coefficient in the study area, which is then used for calibrating the numerical model. Utilizing the friction coefficient distribution estimated through field surveys for model calibration has proven to be robust under various flow conditions. This study enhances the suitability of scenario analysis by considering the physical characteristics of the field rather than treating the friction

coefficient merely as a calibration parameter. Additionally, by narrowing the selection range of the friction coefficient to match field conditions, the method reduces the time required for model calibration.

In summary, the study indicates that high-resolution surface measurements and hydraulic data can be used to estimate roughness height and friction coefficient. Their distribution can also be determined, allowing for representative values that reflect heterogeneous surface characteristics and the obtained distribution can be used to calibrate the numerical model. The findings of this study are significant as they provide a method for determining roughness height and highlight the importance of parameter estimation in field investigations and calibration of numerical model. The study results and related achievements are summarized in Table 6.1.

Table 6.1: Research summary

Chapter 3	Research	Developing roughness predictor for oyster reefs
	Methodology	- Enabling the estimation of roughness height for oyster reefs
	Contribution	Experiment
	Related Publication	
Chapter 4	Research	Field Survey
	Methodology	
	Contribution	- Developing estimation method for friction factor in sandy river - Improving the estimation of bed shear stress
	Related Publication	Lee, Park, Lee, Song, & Park (2024). Earth Surface Processes and Landforms. DOI: http://doi.org/10.1002/esp.5954
Chapter 5	Research	Numerical Simulation
	Methodology	
	Contribution	- Developing method for determining numerical model calibration parameter - Enhancing numerical model calibration procedure
	Related Publication	- Lee, Park, Lee, & Lyu (2024). KSCE Journal of Civil Engineering. 28:1108-1121. - Lee, Park, Ko, Choi, Lyu, & Kim (2024). Journal of Hydro-environment Research. 56: 1-15

Bibliography

- Abreu, T., Michallet, H., Silva, P. A., Sancho, F., van der A, D. A., and Ruessink, B. G. (2013). “Bed shear stress under skewed and asymmetric oscillatory flows.” *Coastal Engineering*, 73, 1–10.
- ASTM Standard D2487-11 (2011). “Standard practice for classification of soils for engineering purposes (unified soil classification system).” *ASTM International, West Conshohocken, PA*.
- Bagherimiyab, F. and Lemmin, U. (2013). “Shear velocity estimates in rough-bed open-channel flow.” *Earth Surface Processes and Landforms*, 38(14), 1714–1724.
- Baranya, S. and Józsa, J. (2013). “Estimation of suspended sediment concentrations with adcp in danube river.” *Journal of Hydrology and Hydromechanics*, 61(3), 232.
- Bartholdy, J., Flemming, B. W., Ernstsén, V. B., Winter, C., and Bartholomäus, A. (2010). “Hydraulic roughness over simple subaqueous dunes.” *Geo-Marine Letters*, 30, 63–76.
- Bellaaj-Zouari, A., Dkhili, S., Gharsalli, R., Derbali, A., and Aloui-Bejaoui, N. (2012). “Shell morphology and relative growth variability of the invasive pearl oyster *pinctada radiata* in coastal tunisia.” *Journal of the Marine Biological Association of the United Kingdom*, 92(3), 553–563.

- Best, J. (2005). “The fluid dynamics of river dunes: A review and some future research directions.” *Journal of Geophysical Research: Earth Surface*, 110(F4).
- Best, J. and Kostaschuk, R. (2002). “An experimental study of turbulent flow over a low-angle dune.” *Journal of Geophysical Research: Oceans*, 107(C9), 18–1.
- Biron, P. M., Ramamurthy, A. S., and Han, S. (2004). “Three-dimensional numerical modeling of mixing at river confluences.” *Journal of Hydraulic Engineering*, 130(3), 243–253.
- Borsje, B. W., van Wesenbeeck, B. K., Dekker, F., Paalvast, P., Bouma, T. J., van Katwijk, M. M., and de Vries, M. B. (2011). “How ecological engineering can serve in coastal protection.” *Ecological Engineering*, 37(2), 113–122.
- Bradley, R. W. and Venditti, J. G. (2017). “Reevaluating dune scaling relations.” *Earth-Science Reviews*, 165, 356–376.
- Cataño-Lopera, Y. A., Abad, J. D., and García, M. H. (2009). “Characterization of bedform morphology generated under combined flows and currents using wavelet analysis.” *Ocean Engineering*, 36(9-10), 617–632.
- Cazenave, P. W., Dix, J. K., Lambkin, D. O., and McNeill, L. C. (2013). “A method for semi-automated objective quantification of linear bedforms from multi-scale digital elevation models.” *Earth Surface Processes and Landforms*, 38(3), 221–236.
- Chanson, H. (2004). *Hydraulics of open channel flow*. Elsevier, Oxford, UK: Butterworth-Heinemann.
- Choe, B.-H., Kim, D.-j., Hwang, J.-H., Oh, Y., and Moon, W. M. (2012). “Detection of oyster

- habitat in tidal flats using multi-frequency polarimetric sar data.” *Estuarine, Coastal and Shelf Science*, 97, 28–37.
- Chowdhury, M. S. N., Walles, B., Sharifuzzaman, S. M., Shahadat Hossain, M., Ysebaert, T., and Smaal, A. C. (2019). “Oyster breakwater reefs promote adjacent mudflat stability and salt marsh growth in a monsoon dominated subtropical coast.” *Scientific Reports*, 9(1), 8549.
- Cleveland, W. S. (1979). “Robust locally weighted regression and smoothing scatterplots.” *Journal of the American statistical association*, 74(368), 829–836.
- Coleman, S. E., Nikora, V. I., and Schlicke, T. (2008). “Spatially-averaged oscillatory flow over a rough bed.” *Acta Geophysica*, 56, 698–733.
- Conevski, S., Guerrero, M., Winterscheid, A., Faltis, D., Rennie, C. D., and Ruther, N. (2023). “Analysis of the riverbed backscattered signal registered by adcps in different bedload transport conditions–field application.” *Journal of Hydraulic Research*, 61(4), 532–551.
- Dao, M. and Tkalich, P. (2007). “Tsunami propagation modelling—a sensitivity study.” *Natural Hazards and Earth System Sciences*, 7(6), 741–754.
- De Lange, S. I., Naqshband, S., and Hoitink, A. J. F. (2021). “Quantifying hydraulic roughness from field data: can dune morphology tell the whole story?.” *Water Resources Research*, 57(12), e2021WR030329.
- De Paiva, J. N. S., Walles, B., Ysebaert, T., and Bouma, T. J. (2018). “Understanding the conditionality of ecosystem services: The effect of tidal flat morphology and oyster reef

- characteristics on sediment stabilization by oyster reefs.” *Ecological Engineering*, 112, 89–95.
- Deltares, D. (2020). “Delft3d-flow user manual: Simulation of multi-dimensional hydrodynamic flows and transport phenomena, including sediments.” *Deltares, The Netherlands*, 1–690.
- Dinehart, R. and Burau, J. (2005). “Averaged indicators of secondary flow in repeated acoustic doppler current profiler crossings of bends.” *Water Resources Research*, 41(9), W09405.
- Dixen, M., Hatipoglu, F., Sumer, B. M., and Fredsøe, J. (2008). “Wave boundary layer over a stone-covered bed.” *Coastal Engineering*, 55(1), 1–20.
- Dunbar, D., van der A, D. A., Scandura, P., and O’Donoghue, T. (2023). “An experimental and numerical study of turbulent oscillatory flow over an irregular rough wall.” *Journal of Fluid Mechanics*, 955, A33.
- Engel, F. L. and Rhoads, B. L. (2016). “Three-dimensional flow structure and patterns of bed shear stress in an evolving compound meander bend.” *Earth Surface Processes and Landforms*, 41(9), 1211–1226.
- Engelund, F. (1966). “Hydraulic resistance for flow over dunes.” *Journal of the Hydraulics Division*, 92(2), 315–326.
- Flack, K. A. and Schultz, M. P. (2010). “Review of hydraulic roughness scales in the fully rough regime.” *Journal of Fluids Engineering*, 132, 041203–1.
- Flemming, B. W. (2000). “The role of grain size, water depth and flow velocity as scaling fac-

- tors controlling the size of subaqueous dunes.” *Marine sandwave dynamics, international workshop*, 23–24.
- Friedman, J. H. (1984). “A variable span smoother.” *Report no.*, Stanford Univ CA lab for computational statistics.
- Fugate, D. C. and Chant, R. J. (2005). “Near-bottom shear stresses in a small, highly stratified estuary.” *Journal of Geophysical Research: Oceans*, 110(C3), C03022.
- Gaeuman, D. and Jacobson, R. B. (2006). “Acoustic bed velocity and bed load dynamics in a large sand bed river.” *Journal of Geophysical Research: Earth Surface*, 111(F2), F02005.
- Gelfenbaum, G., Apotsos, A., Stevens, A. W., and Jaffe, B. (2011). “Effects of fringing reefs on tsunami inundation: American samoa.” *Earth-Science Reviews*, 107(1-2), 12–22.
- Guerrero, M., Rüther, N., and Archetti, R. (2014). “Comparison under controlled conditions between multi-frequency adcps and lisst-sl for investigating suspended sand in rivers.” *Flow Measurement and Instrumentation*, 37, 73–82.
- Gutierrez, R. R., Abad, J. D., Choi, M., and Montoro, H. (2014). “Characterization of confluences in free meandering rivers of the amazon basin.” *Geomorphology*, 220, 1–14.
- Gutierrez, R. R., Abad, J. D., Parsons, D. R., and Best, J. L. (2013). “Discrimination of bed form scales using robust spline filters and wavelet transforms: Methods and application to synthetic signals and bed forms of the río paraná, argentina.” *Journal of Geophysical Research: Earth Surface*, 118(3), 1400–1418.
- Hamrick, J. (2007). “The environmental fluid dynamics code: User manual.” *US EPA, Fairfax, VA, Version, 1*.

- Herrero, H. S., Lozada, J. M. D., García, C. M., Szupiany, R. N., Best, J., and Pagot, M. (2018). “The influence of tributary flow density differences on the hydrodynamic behavior of a confluent meander bend and implications for flow mixing.” *Geomorphology*, 304, 99–112.
- Hervouet, J.-M. (2007). *Hydrodynamics of free surface flows: modelling with the finite element method*. John Wiley & Sons.
- Hitzegrad, J., Brohmann, L., Pfennings, K., Hoffmann, T. K., Eilrich, A. K., Paul, M., Welzel, M., Schlurmann, T., Aberle, J., Wehrmann, A., and Goseberg, N. (2022). “Oyster reef surfaces in the central wadden sea: Intra-reef classification and comprehensive statistical description.” *Frontiers in Marine Science*, 9, 808018.
- Hitzegrad, J., Köster, S., Windt, C., and Goseberg, N. (2024). “Understanding the role of sharp edges in the propagation of surface gravity waves.” *Journal of Geophysical Research: Oceans*, 129(2), e2023JC020336.
- Hoffmann, T. K., Pfennings, K., Hitzegrad, J., Brohmann, L., Welzel, M., Paul, M., Goseberg, N., Wehrmann, A., and Schlurmann, T. (2023). “Low-cost uav monitoring: insights into seasonal volumetric changes of an oyster reef in the german wadden sea.” *Frontiers in Marine Science*, 10, 1245926.
- Holcomb, S. (2023). “Surf2solid—make a solid volume from a surface for 3d printing, <<https://www.mathworks.com/matlabcentral/fileexchange/42876-surf2solid-make-a-solid-volume-from-a-surface-for-3d-printing>>.”
- Holmes Jr, R. R. and Garcia, M. H. (2008). “Flow over bedforms in a large sand-bed river: A field investigation.” *Journal of Hydraulic Research*, 46(3), 322–333.

- Hong, X., Ji, Y., Yan, J., Cheng, J., Wu, S., and Li, Q. (2023). “Study on the wave-dissipation effect of oyster reefs based on the swan numerical model.” *Water*, 15(16), 2884.
- Housego, R. M. and Rosman, J. H. (2016). “A model for understanding the effects of sediment dynamics on oyster reef development.” *Estuaries and Coasts*, 39(2), 495–509.
- Huang, N. E., Shen, Z., Long, S. R., Wu, M. C., Shih, H. H., Zheng, Q., Yen, N., Tung, C. C., and Liu, H. H. (1998). “The empirical mode decomposition and the hilbert spectrum for nonlinear and non-stationary time series analysis.” *Proceedings of the Royal Society of London. Series A: Mmathematical, Physical and Engineering Sciences*, 454(1971), 903–995.
- Humbyrd, C. J. (2012). “Turbulent combined wave-current boundary layer model for application in coastal waters.” M.S. thesis, Massachusetts Institute of Technology, Cambridge, MA, U.S.
- Hwang, D. and Park, Y. S. (2023). “Experimental study on release of plastic particles from coastal sediments to fluid body.” *Journal of Korea Water Resources Association*, 56(2), 125–137.
- Johnson, E. D. and Cowen, E. A. (2017). “Estimating bed shear stress from remotely measured surface turbulent dissipation fields in open channel flows.” *Water Resources Research*, 53(3), 1982–1996.
- Julien, P. Y. (2010). *Erosion and sedimentation*. Cambridge University Press.
- Julien, P. Y. (2018). *River mechanics*. Cambridge University Press.
- Kadivar, M., Tormey, D., and McGranaghan, G. (2021). “A review on turbulent flow over

- rough surfaces: Fundamentals and theories.” *International Journal of Thermofluids*, 10, 100077.
- Kasvi, E., Alho, P., Lotsari, E., Wang, Y., Kukko, A., Hyypä, H., and Hyypä, J. (2015). “Two-dimensional and three-dimensional computational models in hydrodynamic and morphodynamic reconstructions of a river bend: sensitivity and functionality.” *Hydrological processes*, 29(6), 1604–1629.
- Kasvi, E., Laamanen, L., Lotsari, E., and Alho, P. (2017). “Flow patterns and morphological changes in a sandy meander bend during a flood—spatially and temporally intensive adcp measurement approach.” *Water*, 9(2), 106.
- Khosronejad, A., Le, T., DeWall, P., Bartelt, N., Woldeamlak, S., Yang, X., and Sotiropoulos, F. (2016). “High-fidelity numerical modeling of the upper mississippi river under extreme flood condition.” *Advances in Water Resources*, 98, 97–113.
- Kim, D. and Muste, M. (2012). “Multi-dimensional representation of river hydrodynamics using adcp data processing software.” *Environmental Modelling & Software*, 38, 158–166.
- Kim, D. H. and Hwang, J. H. (2023). “Estimating bed shear stress distribution over bottom of a channel on the moving vessel.” *Ocean Science Journal*, 58(1), 3.
- Kim, D.-S., Yang, S.-K., Kim, S.-J., and Jung, W.-Y. (2013). “Development of topological correction algorithms for adcp multibeam bathymetry measurements.” *Journal of Environmental Science International*, 22(5), 543–554.
- Kim, S.-C., Friedrichs, C. T., Maa, J. P. Y., and Wright, L. D. (2000). “Estimating bottom stress in tidal boundary layer from acoustic doppler velocimeter data.” *Journal of Hydraulic Engineering*, 126(6), 399–406.

- Kitsikoudis, V., Kibler, K. M., and Walters, L. J. (2020). “In-situ measurements of turbulent flow over intertidal natural and degraded oyster reefs in an estuarine lagoon.” *Ecological Engineering*, 143, 105688.
- Kostaschuk, R., Villard, P., and Best, J. (2004). “Measuring velocity and shear stress over dunes with acoustic doppler profiler.” *Journal of Hydraulic Engineering*, 130(9), 932–936.
- La Peyre, M. K., Buie, S. C. L., Rossi, R. E., and Roberts, B. J. (2022). “Long-term assessments are critical to determining persistence and shoreline protection from oyster reef nature-based coastal defenses.” *Ecological Engineering*, 178, 106603.
- Lee, M., Park, Y. S., Ko, J. S., Choi, S., Lyu, S., and Kim, B. (2024a). “The influence of density difference, discharge ratio and wind on the mixing at large river confluence.” *Journal of Hydro-environment Research*.
- Lee, M., Park, Y. S., Lee, K., and Lyu, S. (2024b). “Estimation of bedform friction factor directly from bathymetry data.” *KSCE Journal of Civil Engineering*, 28, 1108–1121.
- Lee, M., Park, Y. S., Lee, M., Song, Y.-S., and Park, C. (2024c). “Estimation of friction factor and bed shear stress considering bedform effect in rivers.” *Earth Surface Processes and Landforms*.
- Lefebvre, A., Ernstsens, V. B., and Winter, C. (2013). “Estimation of roughness lengths and flow separation over compound bedforms in a natural-tidal inlet.” *Continental Shelf Research*, 61, 98–111.
- Lefebvre, A., Paarlberg, A. J., Ernstsens, V. B., and Winter, C. (2014). “Flow separation and

- roughness lengths over large bedforms in a tidal environment: A numerical investigation.” *Continental Shelf Research*, 91, 57–69.
- Lefebvre, A., Paarlberg, A. J., and Winter, C. (2016). “Characterising natural bedform morphology and its influence on flow.” *Geo-Marine Letters*, 36, 379–393.
- Lefebvre, A. and Winter, C. (2016). “Predicting bed form roughness: the influence of lee side angle.” *Geo-Marine Letters*, 36(2), 121–133.
- Lichtneger, P., Sindelar, C., Schobesberger, J., Hauer, C., and Habersack, H. (2020). “Experimental investigation on local shear stress and turbulence intensities over a rough non-uniform bed with and without sediment using 2d particle image velocimetry.” *International Journal of Sediment Research*, 35(2), 193–202.
- Lin, H., Yu, Q., Du, Z., Fan, Y., Wang, Y., and Gao, S. (2021). “Geomorphology and sediment dynamics of the liyashan oyster reefs, jiangsu coast, china.” *Acta Oceanologica Sinica*, 40, 118–128.
- Lindhart, M., Monismith, S., Khrizman, A., Mucciarone, D., and Dunbar, R. (2021). “How consistent are estimates of roughness parameters on a rough coral reef?.” *Journal of Geophysical Research: Oceans*, 126(12), e2021JC017825.
- López, R. and Barragán, J. (2008). “Equivalent roughness of gravel-bed rivers.” *Journal of Hydraulic Engineering*, 134(6), 847–851.
- MacVicar, B. and Obach, L. (2015). “Shear stress and hydrodynamic recovery over bedforms of different lengths in a straight channel.” *Journal of Hydraulic Engineering*, 141(11), 04015025.

- Markert, A. (2020). “How dense is dense? toward a harmonized approach to characterizing reefs of non-native pacific oysters—with consideration of native mussels.” *NeoBiota*, 57, 7–52.
- MIKE21, D. and MIKE3 Flow Model, F. (2009). “Hydrodynamic and transport module scientific documentation.” *Denmark: DHI water & Environment*.
- Millar, R. G. (1999). “Grain and form resistance in gravel-bed rivers.” *Journal of Hydraulic Research*, 37(3), 303–312.
- MOE (2018). *Korea Annual Hydrological Report*.
- MOE (2019). *Korea Annual Hydrological Report*.
- MOE (2022a). “2022 river basin survey report.” *Report no.*, Ministry of Environment.
- MOE (2022b). “Investigation and analysis of mixing behavior at the confluence of the representative tributaries in the middle and lower reach of the nakdong river.
- MOLIT (2017). *Korea Annual Hydrological Report*.
- Monismith, S. G. (2007). “Hydrodynamics of coral reefs.” *Annu. Rev. Fluid Mech.*, 39(1), 37–55.
- Moraes, R. P., Reguero, B. G., Mazarrasa, I., Ricker, M., and Juanes, J. A. (2022). “Nature-based solutions in coastal and estuarine areas of europe.” *Frontiers in Environmental Science*, 10, 829526.
- Morris, R. L., Bilkovic, D. M., Boswell, M. K., Bushek, D., Cebrian, J., Goff, J., Kibler, K. M., La Peyre, M. K., McClenachan, G., Moody, J., Sacks, P., Shinn, J. P., Sparks, E. L.,

- Temple, N. A., Walters, L. J., Webb, B. M., and Swearer, S. E. (2019). “The application of oyster reefs in shoreline protection: Are we over-engineering for an ecosystem engineer?.” *Journal of Applied Ecology*, 56(7), 1703–1711.
- Morris, R. L., La Peyre, M. K., Webb, B. M., Marshall, D. A., Bilkovic, D. M., Cebrian, J., McClenachan, G., Kibler, K. M., Walters, L. J., Bushek, D., Sparks, S. E., and Swearer, S. E. (2021). “Large-scale variation in wave attenuation of oyster reef living shorelines and the influence of inundation duration.” *Ecological Applications*, 31(6), e02382.
- Muste, M., You, H., Kim, D., Fleit, G., Baranya, S., Tsubaki, R., Abraham, D., McAlpin, T., and Jones, K. (2023). “On the capabilities of emerging nonintrusive methods to estimate bedform characteristics and bedload rates.” *Water Resources Research*, 59(6), e2022WR034266.
- Muste, M., Yu, K., Pratt, T., and Abraham, D. (2004). “Practical aspects of adcp data use for quantification of mean river flow characteristics; part ii: fixed-vessel measurements.” *Flow Measurement and Instrumentation*, 15(1), 17–28.
- Nikora, V., Goring, D., McEwan, I., and Griffiths, G. (2001). “Spatially averaged open-channel flow over rough bed.” *Journal of Hydraulic Engineering*, 127(2), 123–133.
- Nikora, V., McEwan, I., McLean, S., Coleman, S., Pokrajac, D., and Walters, R. (2007). “Double-averaging concept for rough-bed open-channel and overland flows: Theoretical background.” *Journal of Hydraulic Engineering*, 133(8), 873–883.
- Nikora, V. I., Stoesser, T., Cameron, S. M., Stewart, M., Papadopoulos, K., Ouro, P., McSherry, R., Zampiron, A., Marusic, I., and Falconer, R. A. (2019). “Friction factor decom-

- position for rough-wall flows: theoretical background and application to open-channel flows.” *Journal of Fluid Mechanics*, 872, 626–664.
- O’Donoghue, T. and Wright, S. (2004). “Flow tunnel measurements of velocities and sand flux in oscillatory sheet flow for well-sorted and graded sands.” *Coastal Engineering*, 51(11-12), 1163–1184.
- O’Donoghue, T., Davies, A. G., Bhawanin, M., and van der A, D. A. (2021). “Measurement and prediction of bottom boundary layer hydrodynamics under modulated oscillatory flows.” *Coastal Engineering*, 169, 103954.
- Palman, L. and Trento, A. (2023). “Dispersion coefficients analysis by adcp measurements, tracer test and numerical simulations.” *Environmental Fluid Mechanics*, 23(6), 1381–1402.
- Parsapour-Moghaddam, P. and Rennie, C. D. (2018). “Calibration of a 3d hydrodynamic meandering river model using fully spatially distributed 3d adcp velocity data.” *Journal of hydraulic engineering*, 144(4), 04018010.
- Parsons, D. R., Jackson, P. R., Czuba, J. A., Engel, F. L., Rhoads, B. L., Oberg, K. A., Best, J. L., Mueller, D. S., Johnson, K. K., and Riley, J. D. (2013). “Velocity mapping toolbox (vmt): A processing and visualization suite for moving-vessel adcp measurements.” *Earth Surface Processes and Landforms*, 38(11), 1244–1260.
- Pope, S. B. (2000). *Turbulent flows*. Cambridge University Press.
- Porcile, G., Blondeaux, P., and Colombini, M. (2020). “Starved versus alluvial river bed-forms: an experimental investigation.” *Earth Surface Processes and Landforms*, 45(5), 1229–1239.

- Powell, D. M. (2014). "Flow resistance in gravel-bed rivers: Progress in research." *Earth-Science Reviews*, 136, 301–338.
- Reidenbach, M. A., Berg, P., Hume, A., Hansen, J. C. R., and Whitman, E. R. (2013). "Hydrodynamics of intertidal oyster reefs: The influence of boundary layer flow processes on sediment and oxygen exchange." *Limnology and Oceanography: Fluids and Environments*, 3(1), 225–239.
- Ren, H., Hou, Z., Duan, Z., Song, X., Perkins, W. A., Richmond, M. C., Arntzen, E. V., and Scheibe, T. D. (2020). "Spatial mapping of riverbed grain-size distribution using machine learning." *Frontiers in Water*, 2, 551627.
- Rhoads, B. L. and Kenworthy, S. T. (1998). "Time-averaged flow structure in the central region of a stream confluence." *Earth Surface Processes and Landforms*, 23(2), 171–191.
- Rodi, W., Constantinescu, G., and Stoesser, T. (2013). *Large-eddy simulation in hydraulics*. Crc Press London.
- Rousseau, Y. Y., Biron, P. M., and Van de Wiel, M. J. (2016). "Sensitivity of simulated flow fields and bathymetries in meandering channels to the choice of a morphodynamic model." *Earth Surface Processes and Landforms*, 41(9), 1169–1184.
- Salatin, R., Wang, H., Chen, Q., and Zhu, L. (2022). "Assessing wave attenuation with rising sea levels for sustainable oyster reef-based living shorelines." *Frontiers in Built Environment*, 8, 884849.
- Schlichting, H. and Gersten, K. (2016). *Boundary-layer theory*. springer.
- Scyphers, S. B., Powers, S. P., Heck, K. L. Jr, K. L., and Byron, D. (2011). "Oyster reefs

- as natural breakwaters mitigate shoreline loss and facilitate fisheries.” *PLOS ONE*, 6(8), 1–12.
- Shin, J., Dalziel, S., and Linden, P. (2004). “Gravity currents produced by lock exchange.” *Journal of Fluid Mechanics*, 521, 1–34.
- Shin, J., Seo, J. Y., and Seo, I. W. (2020). “Longitudinal dispersion coefficient for mixing in open channel flows with submerged vegetation.” *Ecological Engineering*, 145, 105721.
- Sime, L. C., Ferguson, R. I., and Church, M. (2007). “Estimating shear stress from moving boat acoustic doppler velocity measurements in a large gravel bed river.” *Water Resources Research*, 43(3).
- Sleath, J. F. A. (1987). “Turbulent oscillatory flow over rough beds.” *Journal of Fluid Mechanics*, 182, 369–409.
- Smart, G., Aberle, J., Duncan, M., and Walsh, J. (2004). “Measurement and analysis of alluvial bed roughness.” *Journal of Hydraulic Research*, 42(3), 227–237.
- Smart, G. M., Duncan, M. J., and Walsh, J. M. (2002). “Relatively rough flow resistance equations.” *Journal of Hydraulic Engineering*, 128(6), 568–578.
- Smith, K. A., North, E. W., Shi, F., Chen, S., Hood, R. R., Koch, E. W., and Newell, R. I. E. (2009). “Modeling the effects of oyster reefs and breakwaters on seagrass growth.” *Estuaries and Coasts*, 32, 748–757.
- Smith, M. W. (2014). “Roughness in the earth sciences.” *Earth-Science Reviews*, 136, 202–225.

- Smith, R. S., Lusk, B., and Castorani, M. C. (2022). “Restored oyster reefs match multiple functions of natural reefs within a decade.” *Conservation Letters*, 15(4), e12883.
- Soulsby, R. (1997). *Dynamics of marine sands*. Thomas Telford, London, U.K.
- Stanley, R. E., Bilskie, M. V., Woodson, C. B., and Byers, J. E. (2024). “A model for understanding the effects of flow conditions on oyster reef development and impacts to wave attenuation.” *Ecological Modelling*, 489, 110627.
- Stewart, M. T., Cameron, S. M., Nikora, V. I., Zampiron, A., and Marusic, I. (2019). “Hydraulic resistance in open-channel flows over self-affine rough beds.” *Journal of Hydraulic Research*, 57(2), 183–196.
- Stone, M. C. and Hotchkiss, R. H. (2007). “Evaluating velocity measurement techniques in shallow streams.” *Journal of Hydraulic Research*, 45(6), 752–762.
- Styles, R. (2015). “Flow and turbulence over an oyster reef.” *Journal of Coastal Research*, 31(4), 978–985.
- Sukhodolov, A. N., Fedele, J. J., and Rhoads, B. L. (2006). “Structure of flow over alluvial bedforms: an experiment on linking field and laboratory methods.” *Earth Surface Processes and Landforms*, 31(10), 1292–1310.
- Swart, D. H. (1974). “Offshore sediment transport and equilibrium beach profiles.” Ph.D. thesis, Delft University of Technology, Delft, Netherlands.
- Thielicke, W. and Sonntag, R. (2021). “Particle image velocimetry for matlab: Accuracy and enhanced algorithms in pivlab..” *Journal of Open Research Software*, 9(1).

- Ullman, S. (1979). "The interpretation of structure from motion." *Proceedings of the Royal Society of London. Series B. Biological Sciences*, 203(1153), 405–426.
- Valentine, P. C. (2019). "Sediment classification and the characterization, identification, and mapping of geologic substrates for the glaciated gulf of maine seabed and other terrains, providing a physical framework for ecological research and seabed management." *Report no.*, US Geological Survey.
- Van Der A, D. A., O'Donoghue, T., Davies, A. G., and Ribberink, J. S. (2011). "Experimental study of the turbulent boundary layer in acceleration-skewed oscillatory flow." *Journal of Fluid Mechanics*, 684, 251–283.
- Van der Mark, C. F. and Blom, A. (2007). "A new and widely applicable bedform tracking tool." *Report no.*, University of Twente, Faculty of Engineering Technology, Department of Water Engineering and Management.
- Van Der Mark, C. F., Blom, A., and Hulscher, S. J. M. H. (2008). "Quantification of variability in bedform geometry." *Journal of Geophysical Research: Earth Surface*, 113(F3), F03020.
- Van der Mark, C. F., Blom, A., and Hulscher, S. J. M. H. (2008). "Quantification of variability in bedform geometry." *Journal of Geophysical Research: Earth Surface*, 113(F3), F03020.
- Van Dijk, T. A. G. P., Lindenbergh, R. C., and Egberts, P. J. P. (2008). "Separating bathymetric data representing multiscale rhythmic bed forms: A geostatistical and spectral method compared." *Journal of Geophysical Research: Earth Surface*, 113(F4), F04017.
- Van Leeuwen, B., Augustijn, D. C. M., Van Wesenbeeck, B. K., Hulscher, S. J. M. H., and De Vries, M. B. (2010). "Modeling the influence of a young mussel bed on fine

- sediment dynamics on an intertidal flat in the wadden sea.” *Ecological Engineering*, 36(2), 145–153.
- Van Rijn, L. C. (1984). “Sediment transport, part iii: bed forms and alluvial roughness.” *Journal of hydraulic engineering*, 110(12), 1733–1754.
- Van Rijn, L. C. (1993). *Principles of sediment transport in rivers, estuaries and coastal seas*. Aqua Publications, The Netherlands.
- Venditti, J. G. (2013). “Bedforms in sand-bedded rivers.” *Treatise on Geomorphology*, 137–162.
- Venditti, J. G. and Bauer, B. O. (2005). “Turbulent flow over a dune: Green river, colorado.” *Earth Surface Processes and Landforms*, 30(3), 289–304.
- Vermeulen, B., Hoitink, A. J. F., and Sassi, M. G. (2013). “On the use of horizontal acoustic doppler profilers for continuous bed shear stress monitoring.” *International Journal of Sediment Research*, 28(2), 260–268.
- Vermeulen, B., Sassi, M. G., and Hoitink, A. J. F. (2014). “Improved flow velocity estimates from moving-boat adcp measurements.” *Water Resources Research*, 50(5), 4186–4196.
- Wang, L., Yu, Q., Zhang, Y., Flemming, B. W., Wang, Y., and Gao, S. (2020). “An automated procedure to calculate the morphological parameters of superimposed rhythmic bedforms.” *Earth Surface Processes and Landforms*, 45(14), 3496–3509.
- Whitman, E. R. and Reidenbach, M. A. (2012). “Benthic flow environments affect recruitment of *crassostrea virginica* larvae to an intertidal oyster reef.” *Marine Ecology Progress Series*, 463, 177–191.

- Wickham, H., François, R., Henry, L., Müller, K., and Vaughan, D. (2019). “dplyr: A grammar of data manipulation [computer software manual].
- Williams, R. D., Brasington, J., Hicks, M., Measures, R., Rennie, C., and Vericat, D. (2013). “Hydraulic validation of two-dimensional simulations of braided river flow with spatially continuous adcp data.” *Water Resources Research*, 49(9), 5183–5205.
- Williams, R. D., Rennie, C. D., Brasington, J., Hicks, D. M., and Vericat, D. (2015). “Linking the spatial distribution of bed load transport to morphological change during high-flow events in a shallow braided river.” *Journal of Geophysical Research: Earth Surface*, 120(3), 604–622.
- Wright, L. D., Gammisch, R. A., and Byrne, R. J. (1990). “Hydraulic roughness and mobility of three oyster-bed artificial substrate materials.” *Journal of Coastal Research*, 6(4), 867–878.
- Xia, W., Akhtar, T., and Shoemaker, C. A. (2022). “A novel objective function dyno for automatic multivariable calibration of 3d lake models.” *Hydrology and Earth System Sciences*, 26(13), 3651–3671.
- Yang, F., Wu, J., Zhang, Y., Zhu, S., Liu, G., Chen, G., Wu, S., and Fan, Z. (2021). “Improved method for identifying manning’s roughness coefficients in plain looped river network area.” *Engineering Applications of Computational Fluid Mechanics*, 15(1), 94–110.
- Yang, J. Q., Kerger, F., and Nepf, H. M. (2015). “Estimation of the bed shear stress in vegetated and bare channels with smooth beds.” *Water Resources Research*, 51(5), 3647–3663.

- Yang, S.-Q. and Tan, S.-K. (2008). “Flow resistance over mobile bed in an open-channel flow.” *Journal of Hydraulic Engineering*, 134(7), 937–947.
- Yen, B. C. (2002). “Open channel flow resistance.” *Journal of Hydraulic Engineering*, 128(1), 20–39.
- Yoo, H., Kim, H., Kang, T., Kim, K., Bang, K., Kim, J., and Park, M. (2024). “Prediction of beach sand particle size based on artificial intelligence technology using low-altitude drone images.” *Journal of Marine Science and Engineering*, 12(1), 172.
- Yuan, J. and Madsen, O. S. (2014). “Experimental study of turbulent oscillatory boundary layers in an oscillating water tunnel.” *Coastal engineering*, 89, 63–84.
- Yuan, J. and Piomelli, U. (2014). “Estimation and prediction of the roughness function on realistic surfaces.” *Journal of Turbulence*, 15(6), 350–365.
- Zomer, J. Y., Naqshband, S., and Hoitink, A. J. (2022). “A tool for determining multiscale bedform characteristics from bed elevation data.” *Earth Surface Dynamics*, 10(5), 865–874.
- Zomer, J. Y., Naqshband, S., Vermeulen, B., and Hoitink, A. J. F. (2021). “Rapidly migrating secondary bedforms can persist on the lee of slowly migrating primary river dunes.” *Journal of Geophysical Research: Earth Surface*, 126(3), e2020JF005918.

국문초록

본 학위논문에서는 해안 및 하천의 주요 거칠기 요소에 대한 조도계수 산정 방법과 이를 수치모델에 적용하는 방법을 연구하였다. 이를 위해 실험, 현장조사, 수치해석을 활용한 세 가지 연구를 수행하였다.

첫 번째 연구에서는 해안 지역의 굴암초에 대한 조도계수 식 개발을 위한 실험 연구를 수행하였다. 굴암초는 갯벌에서 주로 발달하기 때문에, 조석 흐름과 파랑 흐름의 영향을 고려하여 단방향 흐름과 왕복 흐름 조건에서의 실험을 통해 각 조건에서의 조도계수 특성을 이해하고자 하였다. 굴암초 표면 형상을 모사하기 위해 실제 굴암초 표면 자료를 바탕으로 3D 프린터로 제작한 굴암초 모형을 실험에 사용하였다. 실험을 통해 산정한 조도계수와 굴암초의 특성 길이 간의 상관성을 분석하여 조도계수 식을 제안하였고, 이 식은 측정된 유속과 log-law로 추정된 유속 분포를 비교하여 검증하였다. 첫 번째 연구 결과는 굴암초가 해안 흐름 및 하상 변동에 미치는 영향을 이해하는 데 필수적인 요소인 조도계수를 산정하는 데 활용될 수 있다.

두 번째 연구에서는 모래하천에서 주요 거칠기 요소인 형상조도계수와 베드폼의 영향을 고려한 마찰계수 산정에 대해 연구하였다. 하천 구간에서 다양한 크기로 발달한 베드폼은 하상의 조도계수와 마찰계수의 공간적 변화를 유발한다. 이를 효과적으로 이해하기 위해 하천 횡방향 데이터를 이용한 조도계수 및 마찰계수를 추정 방법을 제안하였다. 제안한 방법을 통해 산정한 조도계수와 마찰계수의 타당성은 흐름방향 데이터 분석 결과와의 비교를 통해 검증하였다. 또한, 형상조도계수가 바닥전단력에 미치는 영향 분석을 통해 형상조도계수 산정의 중요성을 입증하였다.

세 번째 연구에서는 수치모델 검·보정에 있어 주요 매개변수인 마찰계수를 하상 자료 분석을 통해 산정하고 적용하는 방법을 연구하였다. 본 연구에서는 첫 번째와 두

번째 연구에서 활용한 표면 분석 방법을 활용하여 조도계수 및 마찰계수를 산정하였다. 다만, 형상 마찰계수를 산정하고 수치모델에 적용하는 과정에서 세 가지 민감도 요인 (1) 마찰계수 분포로부터 마찰계수 결정 과정에서의 최종 결정된 마찰계수의 차이 (2) 베드폼 분석 과정에서의 평활화 정도에 따른 베드폼 크기 변화 (3) 형상조도계수 식에 따른 마찰계수 분포의 변화가 있었다. 이 세 가지 요인이 수치모델 결과에 미치는 영향을 분석하여, 하상 자료 분석을 통한 마찰계수의 수치모델 적용성을 평가하였다. 분석 결과, 세 가지 민감도 요인과 관계없이 강건한 수치해석 결과를 얻었으며, 수치모델 결과의 민감도도 크지 않음을 검증하였다. 세 번째 연구에서 제시한 방법을 수치모델 보정에 활용하면 매개변수 선정을 위한 수치모델 보정 시간을 단축할 수 있을 것으로 기대된다.

위의 세 연구는, 해안 및 하천에서의 주요 거칠기 요소에 대한 조도계수 및 마찰계수를 추정하고, 그 결과를 수치모델에 적용하는 방법 개발하여 해안 및 하천의 표면 특성이 고려된 수치모델 구축에 기여할 수 있다.

주요어: 조도계수, 마찰계수, 표면분석, 바닥전단력, 수치해석

학번: 2019-30187